

3D printing a three degrees of freedom force sensor

M.K. (Marcel) Welleweerd

MSc Report

Committee:

Prof.dr.ir. G. Krijnen
Dr.ir. J.B.C. Engelen
Dr.ir. W. Olthuis
Ing. R.G.P. Sanders

March 2017

004RAM2017
Robotics and Mechatronics
EE-Math-CS
University of Twente
P.O. Box 217
7500 AE Enschede
The Netherlands

Abstract

This thesis describes the development of a technique which enables single material printers to be utilized for the fabrication of sensors. In a single material print channels and voids are incorporated which later are infused with a conducting liquid.

A three degree of freedom force sensor is modeled and designed which can be fabricated using this technique. The sensor consists of a clamped circular membrane with an inclusion. Structures are integrated in the membrane which can be used for both resistive and capacitive measurements. Normal forces acting on the top center of the inclusion are sensed by the resistive measurements and shear forces acting on the top center of the inclusion by the capacitive measurements.

Several structures have been fabricated to characterize the different aspects of fabrication and the sensing principles developed in the model. The minimum channel and membrane size fabricated by the printer are determined. Two types of conductive liquids have been tested. Straight channels with interfacing have been printed and were infused with those liquids to analyze the resistances formed in the channels and the contact resistances formed with the interfacing. Beams have been printed with multiple strain gauges to characterize the resistive part of the modeled force sensor and the difference in sensitivity between two channel cross-sections has been analyzed.

Contents

1	Introduction	2
2	Sensor and sensor modeling	5
3	Conducting liquids	20
4	Fabrication of the sensor	25
5	Experimental section	31
6	Results and discussion	41
7	Conclusion	64
A	Implementing deflection in Matlab	74
B	Strain in a circular membrane with inclusion	76
C	Resistance change in straight and tapered channels	78
D	Capacitance of capacitor plates in a circular membrane with an inclusion	84
E	Linear deflection of a clamped clamped beam	86
F	Linear deflection with channels included	94
G	Nonlinear deflection of a clamped clamped beam	96
H	Interconnects	102
I	Photos fabricated chips and measurement setups	106
J	IV curve measurements	109
K	IV curve measurements 23 days after first measurement	113
L	Measurements on strain gauges with straight channels containing paint	117
M	Measurements on strain gauges with straight channels containing paint	122
N	Measurements on strain gauges with tapered channels containing paint	127

Chapter 1

Introduction

Additive manufacturing (AM), also termed three dimensional (3D) printing, creates a product through the successive stacking of two dimensional layers of material. Not only is this an efficient process but also a green one; primarily because the amount of waste produced is negligible [1]. This way of production is vastly different from traditional manufacturing processes and opens many opportunities. Especially using multi material additive manufacturing this is the case. These processes enable products which have previously been only multi-step productions, to transition into a single-step production. As a result, parts can be seamlessly combined and put into a solid structure leaving a monolithic piece with no glue, solder, wiring or bolts. In creation of a sensor, AM takes away the costs of packaging but also presents a means by which the sensor could be efficiently integrated into a functional object. To give a more concrete example, one could think of incorporating a force sensor in the tip of a prosthetic finger. Issues arise however in that current AM technologies do not meet the standards of the more traditional manufacturing approaches. Further, most AM processes are designed to use only a single material [2].

When it comes to printing a sensor using AM, the most important requirement is that dielectric structural materials can be combined with conductors. There are different ways to accomplish this. Fused deposition modeling (FDM) and material jetting techniques can deposit intrinsically conducting alloys and polymers or polymers containing additives which make the printed material conductive [3–8]. For some materials, post-processing such as a heat treatment is needed to reach their ultimate conductivity [6]. For FDM, additional techniques are available which integrate wires either during printing or with an extra step in which a hot wire is integrated in printed surfaces [9, 10]. If an AM technique is not intrinsically capable of printing multiple materials, one can think of workarounds. An example of this is combining printing techniques with conventional techniques. This is done in the electrostatically actuated micro-mirror made by Mizuno et al.[11], which is produced with a combination of binder jetting and sputtering. Other examples include combining 3D prints with (flexible) printed circuit boards (PCBs) [12] and the use of liquids to cover the non-conductive 3D printed parts with a conductive material [13].

In this research it is investigated whether the technique of filling channels with a conductive material can be used to create a three degree of freedom (3DOF) force sensor. Such a sensor can prove as being an important asset in tactile sensing or rehabilitation purposes [14–17]. This method has previously been used to embed electric circuits in additive manufactured objects. Voids are left for the electric components and the com-

ponents are connected via channels filled with liquid metals or conductive paints [1, 18]. Next to forming interconnections between electronic parts, the filled channels can be used to form passive electric components themselves like resistors, capacitors and coils [19–21]. In printed sensors, the passive components can be used to transduce different physical quantities to electrical signals. However, the liquid conductors have to comply to a different set of requirements than in other applications since the design space and the printer’s resolution are limited. 3D printing further offers a lot of design freedom and the possibilities to exploit these are yet to be explored. What remains is the need to properly interface the conductive tracks to readout circuitry. These are the several aspects looked at in this report. The resulting process flow for building such a sensor is shown in Figure 1.1. After the sensor is designed in a CAD program the sensor will be printed using a suitable printing method. The third step is adding the interfacing between the electrical read-out and the conductive liquid. Finally, the channels are infused with the conductive liquid. In the remainder of this text the different process steps are explained in more detail.

In chapter 2 a 3DOF force sensor based on a circular membrane with an inclusion is presented. This design combines the use of strain gauges with capacitor plates to come to a differential measurement of both normal and shear forces. Subsequently, the behavior of the sensor will be modeled. First the mechanical response due to both normal and shear forces is derived. Then, how the mechanical responses translate to changes in both resistance and capacitance will be looked at.

Chapter 3 addresses the different available conducting liquids which could possibly be used for filling the channels in the 3D print.

Chapter 4 elaborates on the fabrication technology of the sensor. The printing process and the post-processing will be described and compared with other available printing techniques.

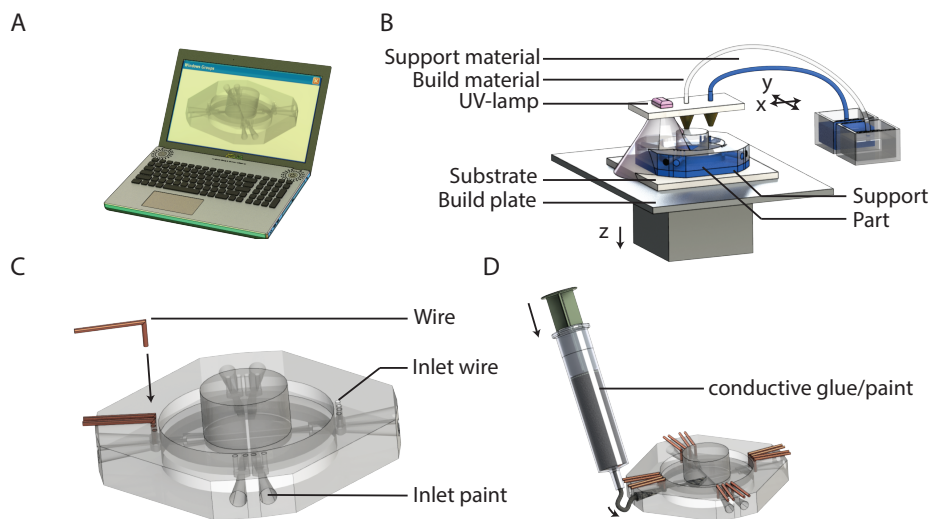


Figure 1.1: Process flow of building a sensor. A. The sensor is designed using CAD software. B. The part is printed using a suitable printing method. C. The interfacing to the outside world is added. D. The channels and cavities in the sensor are infused with a conductive liquid.

Chapter 2

Sensor and sensor modeling

2.1 Introduction

The 3DOF force sensor presented in this work will be based on a circular membrane with an inclusion (Figure 2.1 A). Such sensors have been used in the past to function as tactile force sensors [22, 23] and flow sensors [24]. It consists of a thin circular membrane clamped all along the edge with a circular part in the middle (the inclusion) which is thicker and thus stiffer than the surrounding part. If a normal force is exerted on the inclusion, the membrane will bend downward as a function of the force. If instead a shear force is applied on the top center of the inclusion, the force will cause a moment which makes the inclusion rotate around the center of the membrane. The mechanical response of the membrane can be transduced to electrical signals in different manners. When installed on opposite sides of the membrane, a normal force will cause strain gauges to have the same response, while a shear force will cause the strain gauges to respond in an opposite way [22]. When using capacitances on opposite sides of the inclusion, again a normal force will cause both capacitances to increase, whereas a shear force will make one capacitor increase its capacitance and the other decrease [24]. In both situations this means that one has to know the absolute resistance or capacitance of each sensing element to have all information about the magnitude and the direction of the force. The use of a differential readout results generally in a higher sensitivity of the sensor for both resistive and capacitive sensors. An example of a differential resistive measurement circuit is a Wheatstone bridge [25]. Differential capacitive sensors can be read out in high resolution using a charge amplifier [26].

The sensor will thus be designed to measure both normal and shear forces in a differential manner. Small channels run through the membrane leading to a cavity with the shape of a quarter of a circle. When filled with a liquid conductor, the channels function as a strain gauge while the cavities function as capacitor plates. As shown in the cross-section of the membrane, the channels are not completely straight but incorporate a perpendicular segment midway. Also, immediately adjacent channels are mirror images of one another in the horizontal plane. This will lead to an opposite response to normal forces due to opposite experienced strain (tensile vs. compressive). This will be elaborated later on in this chapter. The cavities in the inclusion form a capacitor together with static electrodes in the bottom part of the sensor. The capacitors will have an opposite response as a result of shear forces. The two capacitor pairs allow for differentiation of shear forces in the x- and y-direction. Thus, each channel in the membrane is utilized to do both the capacitive measurement and the resistive measurement. The electrical

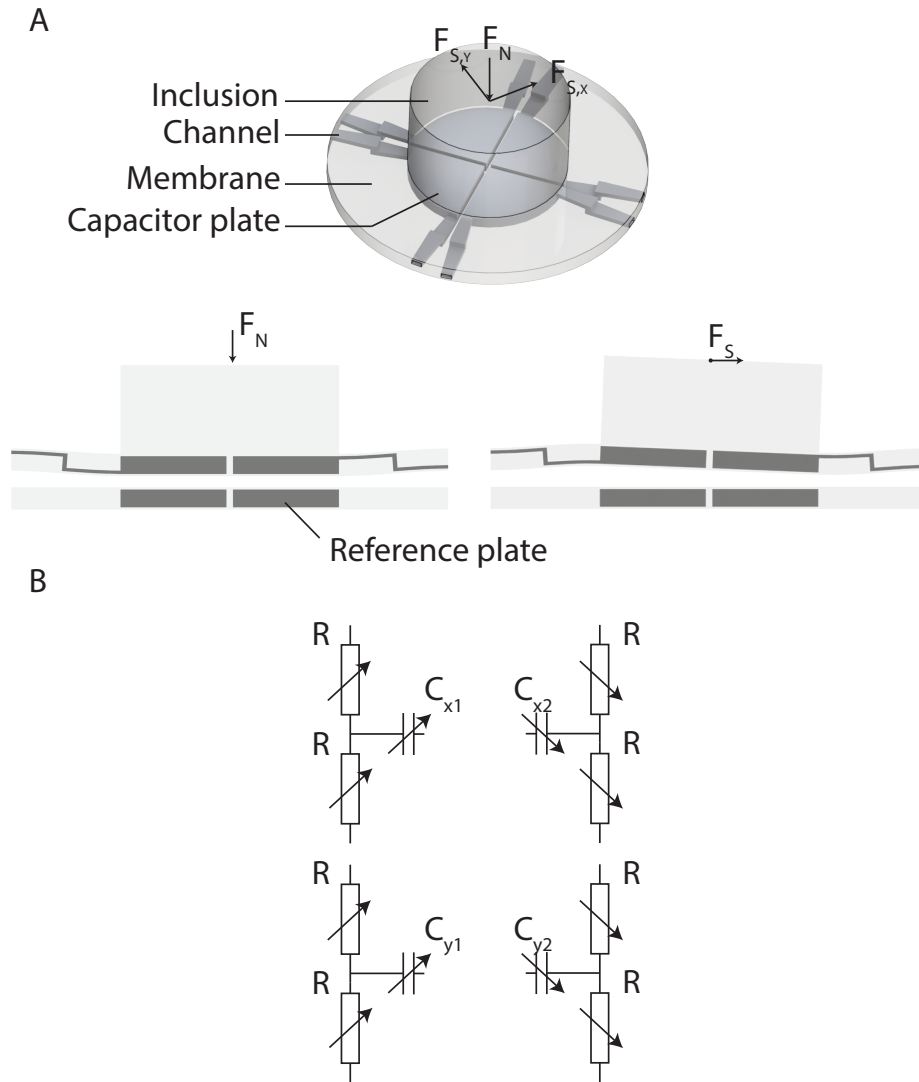


Figure 2.1: A. Basic sensor form; a circular plate clamped all around the edge with incorporated channels functioning as sensing elements. Two cross sections with bending as a result of normal and shear forces. B. The electrical representation of the four channels, capacitor plates and reference electrodes.

diagram for each channel is shown in Figure 2.1 B.

The remainder of this chapter describes the modeling of the presented sensor. Keeping in mind that a possible application would be in prosthesis or rehabilitation purposes, the sensor will be modeled to be as large as a finger tip and have a similar working range: It will be 15 mm in diameter and measure forces in the range of 0–25 N [27]. First the mechanical behavior is explained and then an explanation is given on how the electrical structures can be placed in the membrane to achieve an optimal sensitivity.

2.2 Deflection of the membrane

The design of the sensor is based on a fully clamped circular membrane, as shown in Figure 2.2. The deflection determines the change in capacitance as well as the change in resistance. Therefore, it is essential to know what influence the design parameters have

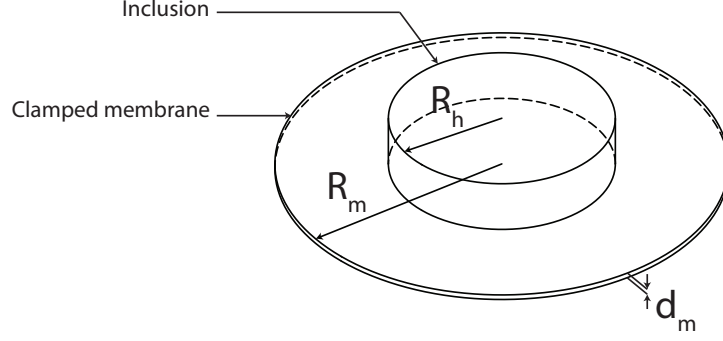


Figure 2.2: Schematic view of the clamped membrane with stiff inclusion.

on the behavior of the membrane.

The forces acting on the top center of the inclusion cause the membrane to deflect in two different modes (Figure 2.3). The membrane bends downward when a normal force (F_N) is applied on the inclusion. Depending on the orientation of the sensor, the weight of the inclusion adds positively or negatively to the total deflection. The second mode of deflection is caused by a moment of force which in turn is generated by a shear force (F_S) acting on the top center of the inclusion. In both modes of deflection, the forces exerted on the top of the membrane generate a certain force distribution on the membrane along the edge of the inclusion.

The general differential equation relating the deflection $w(r, \theta)$ of a plate with a uniform thickness to a force distribution over that plate $f(r, \theta, t)$ is:

$$D\nabla^4 w(r, \theta) + \rho_m d_m \frac{\partial^2 w(r, \theta)}{\partial t^2} = f(r, \theta, t) \quad (2.1)$$

Where r and θ are coordinates in a polar system, ρ_m is the density of the plate material (kgm^{-3}) and d_m is the plate thickness (m), ∇^2 is the Laplace operator:

$$\nabla^2 = \frac{\partial^2}{\partial r^2} + \frac{1}{r} \frac{\partial}{\partial r} + \frac{1}{r^2} \frac{\partial^2}{\partial \theta^2} \quad (2.2)$$

And D is the flexural rigidity of the membrane, defined as:

$$D = \frac{E d_m^3}{12(1 - \nu^2)} \quad (2.3)$$

In this relation E is the Young's modulus (Nm^{-2}) and ν is the Poisson's ratio of the plate.

Equation 2.1 neglects the rotational inertia of the plate as well as the shear deformation [28]. For small deformations, the equation can be solved separately for the force

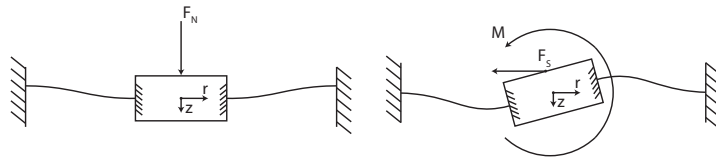


Figure 2.3: Schematic depiction of the deflection modes.

distribution generated by each mode of deflection. Using superposition the total deflection generated by a combination of a normal force and a shear force on the top center of the inclusion can be calculated. By approximating the dynamic behavior by its static behavior - because the sensor will only be used at very low frequencies - 2.1 is simplified to

$$D\nabla^4 w = f(r, \theta) \quad (2.4)$$

Solving this differential equation for both a normal force and and moments acting on the center of the inclusion has previously been undertaken [24]. For normal forces, solving the equation yields:

$$w_{m,N}(\rho) = \frac{F_N R_m^2}{16\pi D} \left[1 - \rho^2 + 2\rho \ln(\rho) - \frac{2\zeta^2 \ln(\zeta)}{1 - \zeta^2} (1 - \rho^2 + 2 \ln(\rho)) \right] \quad (2.5)$$

In which $\rho = \frac{r}{R_m}$ is the normalized distance from the center of the membrane and $\zeta = \frac{R_h}{R_m}$, the ratio between the radius of the inclusion R_h and the radius of the total membrane R_m . The resulting anti-symmetric deflection of the membrane due to a moment generated by shear forces is:

$$w_{m,S}(\rho, \theta) = \frac{MR_m}{8\pi D} \left[\frac{\rho^2 \{1 - \zeta^2 - \rho^2 + 2 \ln(\rho) (1 + \zeta^2)\} + \zeta^2}{\rho (1 + \zeta^2)} \right] \cdot \cos(\theta - \varphi) \quad (2.6)$$

In which φ is the direction of the shear force in radians, and M is the moment (N m) induced by the shear force F_s (N) acting on the inclusion. The shear force and the moment are related to each other in the following way:

$$M = h_i F_s \quad (2.7)$$

Where h_i is the height of the inclusion (m).

Using the input of Table 2.1, Figure 2.4 shows the deflection of the plate for a normal force of 25 N (left) and a shear force of 25 N in $-x$ direction (right). The Matlab code used for modeling the deflection is given in Appendix A. It is shown that normal and shear forces generate deflections around 35 μm and 20 μm respectively. This means that the gap between the membrane and the bottom electrodes should be at least 55 μm in order to work in the full range of forces.

Table 2.1: Input parameters for obtaining Figure 2.4.

R_m	R_h	h_i	T_m	E	ν
7.5 mm	3.25 mm	3 mm	1 mm	1.463 GNm^{-2}	0.35

2.3 Strain and strain gauges

Strain is a measure of deformation of an object as a response to a stress. Suppose an element is subject to a tensile stress in the x direction, σ_x (Nm^{-2}) (Figure 2.5)[29]. The length L_0 (m) of the element will be increased by ΔL , while the height h (m) and width w (m) decrease with an amount of Δh and Δw respectively. If instead a compressive stress is applied, the length of the element will decrease, while the height and width increase.

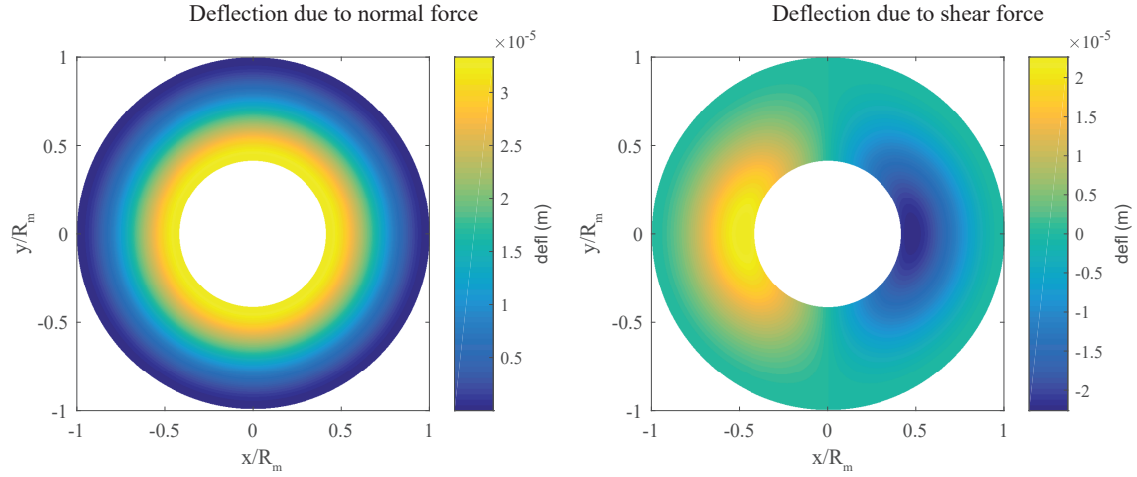


Figure 2.4: Left the modeled deflection due to a normal force of 25 N. Right the modeled deflection due to a shear force of 25 N.

The ratio between the increased length and the original length is called normal strain and is defined as:

$$\epsilon = \frac{\Delta L}{L_0} \quad (2.8)$$

The magnitude of the strain is directly related to the stress and the Young's modulus E (Nm^{-2}) of the material as:

$$\epsilon = \frac{\sigma}{E} \quad (2.9)$$

The shortening in the directions perpendicular to the stress is described by Poisson's ratio as:

$$\frac{\Delta h}{h_0} = \frac{\Delta b}{b_0} = -\nu \frac{\Delta L}{L_0} \quad (2.10)$$

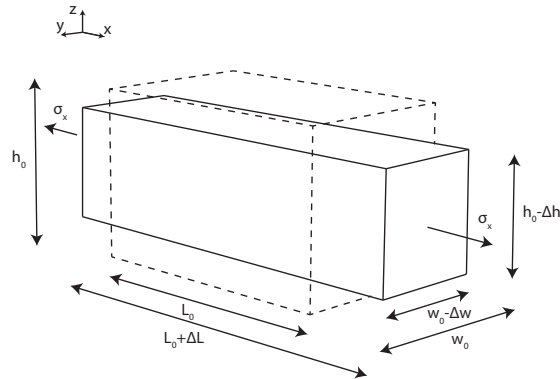


Figure 2.5: When a body is subjected to a tensile stress in x-direction, the body will increase in length l while height h and width w decrease. Adapted from [29].

In which ν is the Poisson's ratio. If the stressed element consists of a conductive material, the element can be used as a transducer. Normally, the resistance R (Ω) of a piece of conductor can be expressed as:

$$R = \rho_R \frac{L}{A} \quad (2.11)$$

In the formula, A represents the the cross-sectional area of the piece of material (m^2) and ρ_R the resistivity of the conductor (Ωm). Now, if the material is under stress, both the length and the cross sectional area of the conductor will be altered. It can be proven that the relative resistance change due to strain is as follows:

$$\frac{\Delta R}{R} = (1 + 2\nu)\epsilon + \frac{\Delta\rho_R}{\rho_R} \quad (2.12)$$

The left part of the equation ($(1 + 2\nu)\epsilon$) describes the relative resistance change as a result of dimensional changes. The right part ($\frac{\Delta\rho_R}{\rho_R}$) describes resistance changes caused by a change in resistivity [29]. The latter will be elaborated on in chapter 3 however will not be incorporated into the modeling as the resistivity change is unknown. For situations in which the channel cross-section and the strain are arbitrarily distributed over the channel length, the left part of Equation 2.12 can be expressed using a more general description:

$$\frac{\Delta R}{R} = \frac{\rho_R \int_a^b \left(\frac{1}{A(r)}\right) (1 + 2\nu) \epsilon(r) dr}{\rho_R \int_a^b \frac{1}{A(r)} dr} = \frac{\int_a^b \left(\frac{1}{A(r)}\right) (1 + 2\nu) \epsilon(r) dr}{\int_a^b \frac{1}{A(r)} dr} \quad (2.13)$$

Strain is also present in the deflected membrane and the introduced principles can be used in designing a membrane incorporating strain gauges with an optimal sensitivity. The magnitude of the strain is not the same everywhere in the membrane. The relation for the radial strain in the membrane is required as a start. For deflections which are small in comparison with the membrane thickness, it can be assumed that the middle plane of the plate remains unstrained. From now on this will be called the neutral plane (Figure 2.6). An equation utilizing the second derivative of the deflection can be derived to calculate the strain at a position r at a distance z from the neutral plane:

$$\epsilon(r) = z \left(\frac{d^2 w}{dr^2} \right) = z \left(\frac{d^2 w_{m,N}}{dr^2} + \frac{d^2 w_{m,S}}{dr^2} \right) \quad (2.14)$$

This relation is evaluated for a normal force and for a shear force using the parameters denoted in Table 2.1(Figure 2.7). It can be concluded from this relation that a normal force induces a strain which has a circular symmetry whereas a shear force induces a strain which is anti-symmetric.

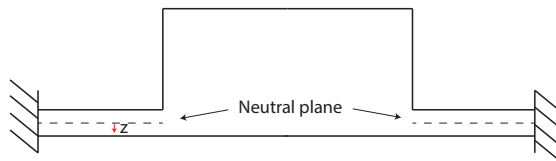


Figure 2.6: A cross-section of the membrane with the unstrained neutral plane indicated. Strains are evaluated at a distance z from the neutral plane.

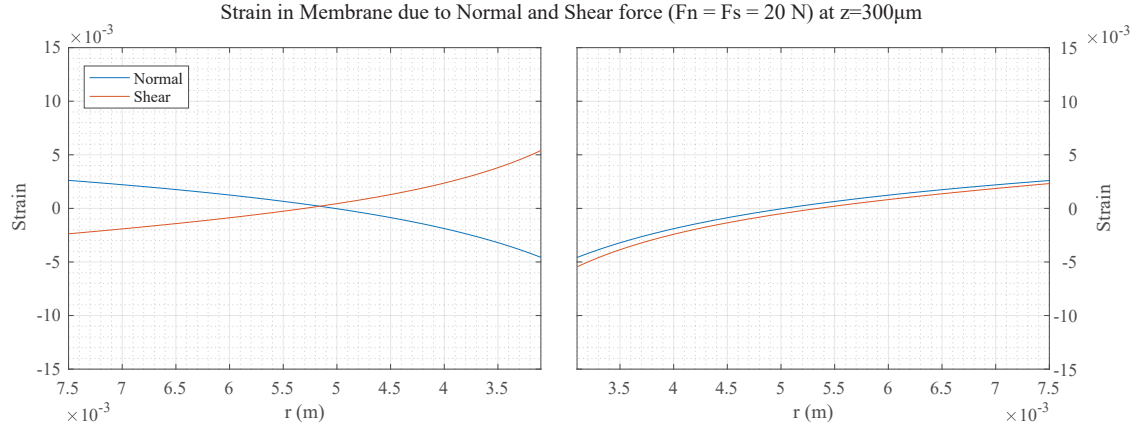


Figure 2.7: Strain in a cross-section of the membrane due to normal force (blue line) and shear force (red line) on both sides of the inclusion. The same parameters as stated in Table 2.1 apply.

Additionally, 2.14 is plotted for strains induced by various normal forces in Figure 2.8. In this graph it stands out that all the lines change sign at the same coordinate r . This coordinate can be found by setting 2.14 to zero and numerically solving the equation for r . It is found that the strain resulting from a normal force changes sign at a particular coordinate regardless of the exerted force. This coordinate at which the strain changes sign is named $r = S$ from now on.

These insights lead to a strain gauge design as shown in Figure 2.9. If the strain gauge is arranged to cross the neutral plane of the membrane at $r = S$, it will experience the same sign strain along r . The optimal placement of the strain gauge is as close to the surface as the fabrication technique allows. Also, the height h of the channel should be as small as possible, as the resistance change will be evaluated for strains in the middle of the channel. Further, two strain gauges placed on alternate sides of the membrane and mirrored in the neutral plane, experience the same strain for shear forces but an opposite strain for normal forces.

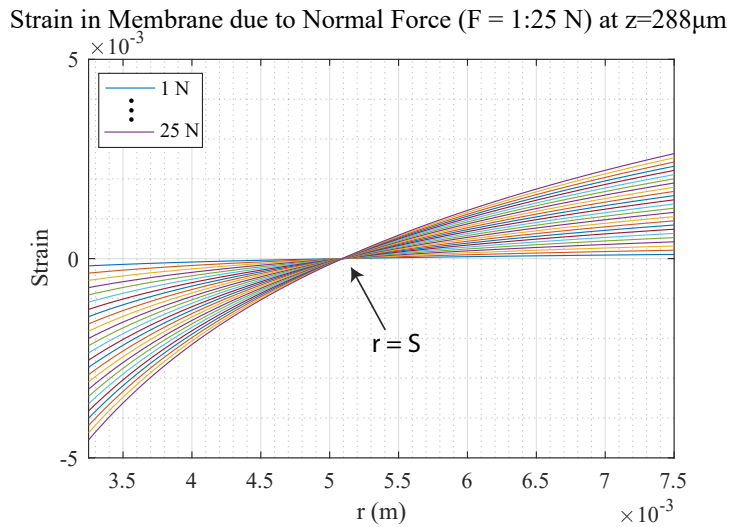


Figure 2.8: The strain in the membrane as a function of r and $F(N)$. The same parameters as stated in Table 2.1 apply. The strain changes its sign at $r = S$ regardless of the exerted force.

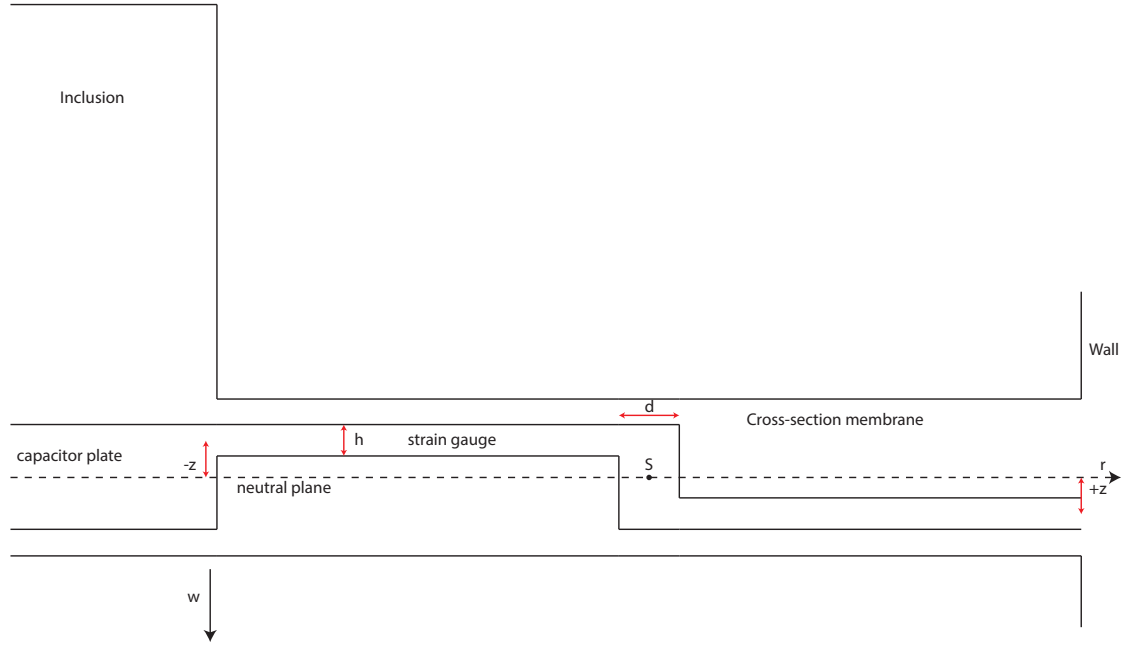


Figure 2.9: Strain gauge design in which the channel goes from one side of the neutral plane to the other.

Placed in a Wheatstone configuration these elements produce a sensor which is sensitive towards normal force and insensitive towards shear forces. Consequently, strain due to shear forces is left out of the following derivations.

From 2.13 it follows that to obtain relatively high changes in resistance, the cross-section $A(r)$ should be large when the strain magnitude is small and should become smaller as the strain magnitude increases. Therefore, two channel designs are considered (Figure 2.10). One design has parallel channel walls and its cross-section remains h by w along the whole channel length. The other channel has a certain height h which remains constant over the channel length. The width w changes however. It starts with a certain width w_0 and towards the point S the channel widens until it reaches a certain width w_1 . What follows is a vertical section in which the channel crosses the neutral plane. Then, the channel width decreases again until it reaches a certain width w_3 . The first channel design will be called straight whereas the other will be called tapered. For both the

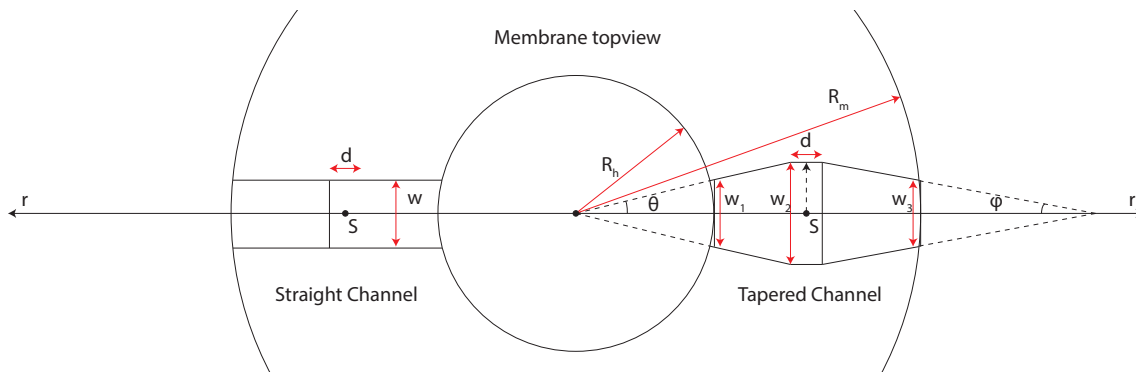


Figure 2.10: The two channel designs, straight (left) and tapered (right) viewed from the top. The details are magnified for clarification.

straight and tapered channel the equation to be solved for finding the relative resistance change is:

$$\begin{aligned}
\frac{\Delta R}{R} &= (1 + 2\nu) \frac{\int_{R_h}^{S-\frac{1}{2}d} \frac{1}{A_a(r)} \epsilon(r) dr + \int_{S+\frac{1}{2}d}^{R_m} \frac{1}{A_b(r)} \epsilon(r) dr}{\rho_R \int \frac{1}{A(r)} dr} \\
&= (1 + 2\nu) \frac{-z \int_{R_h}^{S-\frac{1}{2}d} \frac{1}{A_a(r)} \frac{d^2 w_n}{dr^2} dr + z \int_{S+\frac{1}{2}d}^{R_m} \frac{1}{A_b(r)} \frac{d^2 w_n}{dr^2} dr}{\int_{R_h}^{S-\frac{1}{2}d} \frac{1}{A_a(r)} dr + \int_{-z-\frac{1}{2}h}^{z+\frac{1}{2}h} \frac{1}{A_c} dz + \int_{S+\frac{1}{2}d}^{R_m} \frac{1}{A_b(r)} dr + \frac{1}{2} \int \frac{1}{A_{cap}(y)} dy}
\end{aligned} \tag{2.15}$$

The parts of the channel that add to the resistance change are the two horizontal parts of the channel. There are also two parts which are static: the vertical section in which the channel crosses the neutral plane and the capacitor plate to which the strain gauge leads. This equation cannot be solved analytically for some part. For a more detailed description on solving the integrals and the Matlab implementation please refer to Appendix C. The result is shown in Figure 2.11. When applying the settings as described in Table 2.2, utilizing tapered channels increases sensitivity by roughly 6% according to the model. Self-evidently, in the case where the strain is the highest at the edges of the membrane means the larger the ratio between w_1 and w_2 and between w_2 and w_3 , the larger the sensitivity of the strain gauge.

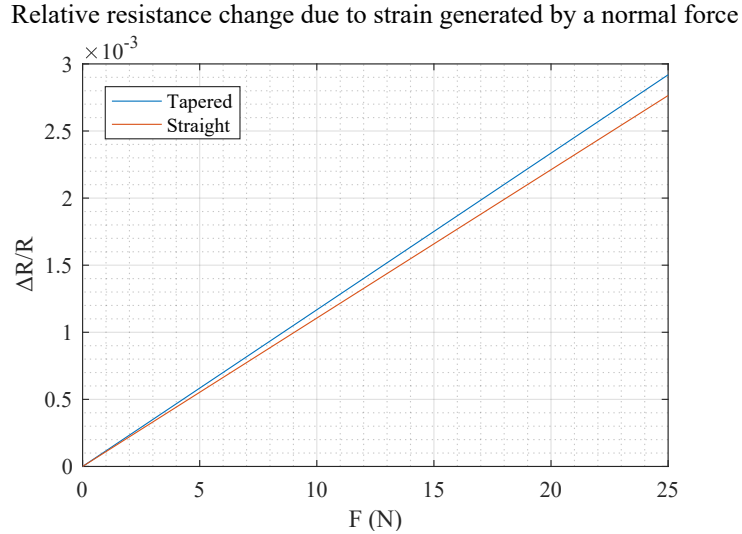


Figure 2.11: Relative resistance change as a function of force modeled for straight (red) and tapered (blue) channels.

2.4 Capacitance

A capacitor is a device which in its most basic configuration consists of two parallel conducting plates with an insulator (dielectric) in between. If a voltage source is connected to these two plates, the plates will start to store electrical charges until the voltage drop over the capacitor, due to the generated electrical field, is the same as the potential difference of the voltage source. The main characteristic of a capacitor is the capacitance, which is expressed by Equation 2.16:

$$C = \frac{Q}{V} = \frac{(\epsilon_0 \epsilon_r A)}{d} N \quad (2.16)$$

In the equation, C is the capacitance (F), V is the voltage applied to the plates (V), ϵ_0 is the permittivity in a vacuum (F m^{-1}), ϵ_r is the relative permittivity, A is the electrode area (m^2), and N is the number of layers or fingers [30].

A capacitor is often used in Micro Electro Mechanical Systems to convert physical quantities like force and pressure into an electric signal or the other way around. To be able to use the capacitor as a measurement instrument, one of the plates of the capacitor should be suspended by springs such that it can move freely while the other plate is connected to a reference frame. If one of the plates moves with respect to the other the thickness of the insulator d becomes larger or smaller and thus the capacitance changes. Other setups, in which the overlapping area A changes with the movement of the electrodes or in which the relative permittivity ϵ_r changes due to environmental quantities such as humidity, exist [12, 31].

The 3D-printed capacitors in this project will have three dielectrics in series: A layer of printed material, the air gap and another layer of printed material. The capacitance of a capacitor with three stacked dielectrics can be calculated as three capacitors in series, the gap of each capacitor being the thickness of the dielectric. Self-evidently, one of the gaps depends on the deflection of the inclusion, while the other two are static:

$$\frac{1}{C} = \frac{1}{C_1} + \frac{1}{C_2(w_{\text{incl}}(r, \theta))} + \frac{1}{C_3} \quad (2.17)$$

From this relation can be deduced that the higher C_1 and C_3 are, the closer the substitutational value will be to C_2 . This is beneficial when doing the measurements. Large values can be reached by printing the smallest possible layer of material between the conductor and the air gap. Also, high relative permittivities are favorable. In this project, the printed material has a relative permittivity of around 6 (see chapter 4), and the air in the gap a value of around 1.

The thickness of the printed layer of material remains constant and as a result the capacitance of C_1 and C_3 remains constant. The value can therefore be calculated as:

$$C_{1,3} = \iint \frac{\epsilon_0 \epsilon_1 r \, d\theta dr}{d_p} \quad (2.18)$$

This is a surface integral in polar coordinates r and θ over the capacitor plate. In the relation, d_p is the thickness of the printed layer between the conducting liquid and the air gap (m).

The other capacitance, C_2 , changes with the deflection of the inclusion:

Table 2.2: Input parameters for obtaining Figure 2.11.

Straight					
w	h	z	d		
510 μm	224 mm	288 mm	600 μm		
Tapered					
w_1	w_2	w_3	h	z	d
560 μm	1 mm	560 mm	224 mm	288 mm	600 μm

$$C_2 = \iint \frac{\epsilon_0 \epsilon_2 r \, d\theta dr}{d_0 - w_{\text{incl}}(r, \theta)} \quad (2.19)$$

The deflection $w(r, \theta)_{\text{incl}}$ in this is the deflection of the inclusion, not the surrounding membrane. If the membrane radius is R_h , $w(r, \theta)_{\text{incl}}$ is valid for:

$$0 \leq r < R_h \quad (2.20)$$

The deflection of the inclusion is again a superposition of a deflection due to normal forces and deflection due to shear forces. It is defined as:

$$w_{\text{incl}}(r, \theta) = w_{\text{incl,N}}(r) + w_{\text{incl,N}}(r, \theta) = w_{\text{m,N}}(R_h) + r \frac{\partial w_{\text{m,S}}(R_h, \theta)}{\partial r} \quad (2.21)$$

In which $w_{\text{m,N}}$ and $w_{\text{m,S}}$ are the deflections due to normal and shear force as defined in Equation 2.5 and 2.6 evaluated at $r = R_h$, respectively. Equation 2.21 follows from the boundary conditions of both Equation 2.5 and 2.6 and the assumption that the inclusion is stiff and will not deform. The deflection of the membrane as a result of the normal force has a derivative $\frac{\partial w_{\text{m,N}}(r)}{\partial r} = 0$ along the edge of the inclusion. Hence, the deflection of the inclusion as a result of the normal force is $w_{\text{m,N}}(R_h)$. The position of the inclusion as a function of the shear force has got the same slope as the membrane has on the edge, this time the slope being non-zero. The inclusion forms a circular plane going through the origin, its function being $r \frac{\partial w_{\text{m,S}}(R_h, \theta)}{\partial r}$.

Equation 2.21 has to be inserted into 2.19. Subsequently, Equation 2.18 and 2.19 have to be integrated over the area of the capacitor plate. The layout of the capacitor plates is shown in Figure 2.12. While the four plates follow the circular shape of the inclusion with radius R_h , they are not quarters since they are displaced from the inclusion center to isolate them from each other. When integrating over r , the lower boundary depends on the angle θ , while the upper boundary is simply R_h . θ should be chosen such that the entire plate area is covered. The result is:

$$C_2 = \epsilon_0 \epsilon_2 \iint \frac{r}{d_0 - w_{\text{incl}}(r, \theta)} dr d\theta = \epsilon_0 \epsilon_2 \int_{-\theta_{\text{max}}}^{\theta_{\text{max}}} \int_{r_{\text{min}}}^{R_h} \frac{r}{d_0 - w_{\text{m,n}}(R_h) - r \frac{\partial w_{\text{m,s}}(R_h, \theta)}{\partial r}} dr d\theta$$

$$\theta_{\text{max}} = 2 \tan^{-1} \left(\frac{\sqrt{2R_h^2 - r_0^2} - R_h}{r_0 + R_h} \right)$$

$$r_{\text{min}} = r_0 \sin(\theta) \tan \left(\theta + \frac{1}{4} \pi \right) + \cos(\theta) r_0 \quad (2.22)$$

The same integration boundaries have to be applied to Equation 2.18. After solving these integrals, C_1 , C_2 and C_3 have to be combined using Equation 2.17. All these steps are integrated in a Matlab code which can be found in Appendix D. The capacitance will be read out using a differential read-out method. So it is not the absolute capacitance of the four capacitors which is important, but rather the difference between the capacitor pairs when a shear force is applied. Using the model it can be defined what the optimal radius of the inclusion R_h is for a set radius of the membrane R_m to get the highest sensitivity. This is shown in Figure 2.13, in which a shear force F_s is exerted on top center of the inclusion in the direction $\theta = 0$. Other parameters used in obtaining this

graph are shown in Table 2.3. From the figure it can be deduced that the maximum sensitivity for shear forces will be obtained at 3.25 mm and that the resulting maximum capacitance difference is around 32 fF. This a small capacitance change, but it should be possible to measure with a charge amplifier as presented by Lammerink et al.[26].

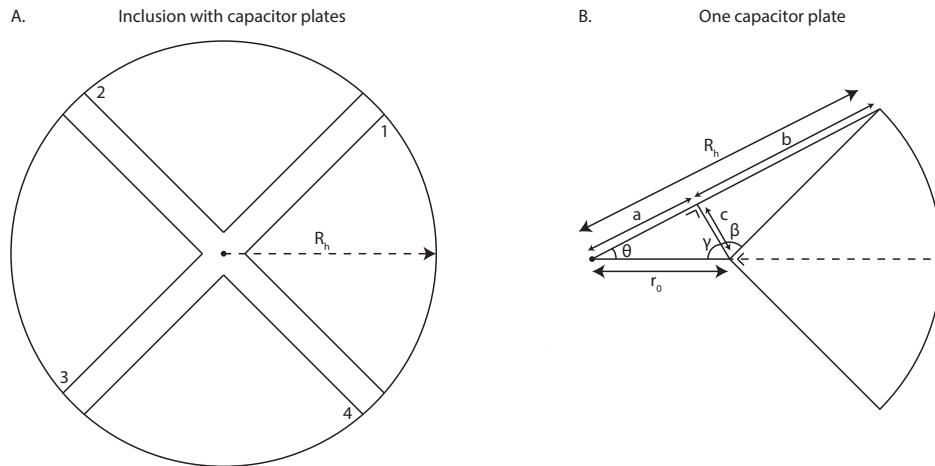


Figure 2.12: A. Topview of the inclusion with the four capacitor plates. B. One capacitor plate with an (exaggerated) offset from the center of the inclusion to pinpoint the integration boundaries.

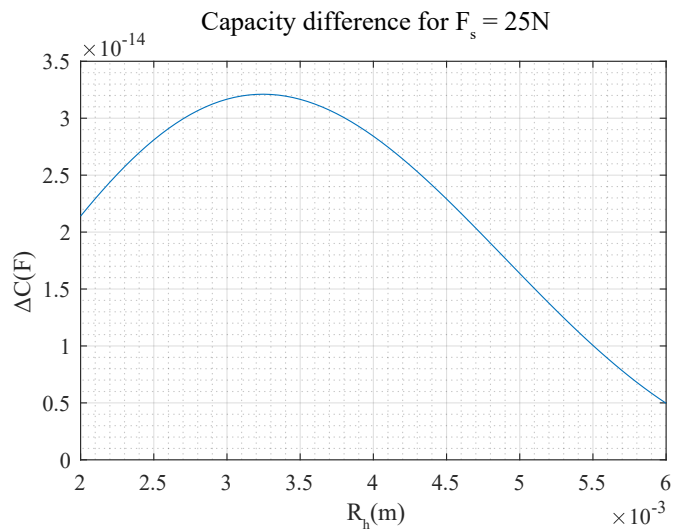


Figure 2.13: The difference in capacitance ΔC between C_1 and C_3 at $F = 25\text{N}$ in the direction $\theta = 0$ for a varying R_h .

Table 2.3: Input parameters for obtaining Figure 2.13.

R_m	h_i	T_m	E	ν	d_p	d_0
7.5 mm	3 mm	1 mm	1.463 GNm^{-2}	0.35	100 μm	200 μm

2.5 Discussion

In the modeling of the sensor, several assumptions have been made which mean that the modeled response will deviate from reality.

In relation to the membrane stiffness, two parameters are not taken into account. First of all, the model assumes a continuous membrane whereas in reality the membrane has channels integrated into it. The channels are filled with a conducting liquid or suspension which may add some stiffness to the channels. However, fluids deform easily and suspensions mostly result in porous and brittle structures. As such, the effective membrane stiffness will likely be lower than what is accounted for in the model. Alternately, the production process may introduce initial stresses in the membrane, stiffening the membrane [24]. The final effect of both these potential influences remains to be seen. The overall behavior of the sensor will be the same but the responsivity will vary.

The material which the membrane will be made of is a polymer. In the modeling of the membrane an elastic material is assumed while in reality a polymer is a viscoelastic material. There are two types of ideal materials: Elastic solids and viscous liquids. An elastic solid has a definite shape and deforms under stresses. All the energy obtained from those stresses is stored and once the stress is released the energy is released as well and the elastic solid regains its original shape. Viscous liquids on the other hand have no definite shape and flow irreversibly when forces are applied. Viscoelastic media however, can cover the whole intermediate range of properties between the before mentioned materials. This means that the nature of the model shifts from static to quasi-static. For a static load, the response of the sensor will not be static. In reality, the Young's modulus of the material is time and frequency dependent [32]. After the initial deformation due to the exerted force on the membrane, the membrane will have the tendency to slowly deform under the influence of the mechanical stresses. This phenomenon is called creep. Furthermore, the presence of an anelastic component means some energy is always lost as heat during loading and unloading; consequently, the unload curve does not follow the load curve. This dependency on past as well as present loads is termed hysteresis [33]. Nevertheless, it has been decided to use a linear model because the polymer used is stiff and brittle and the stress-strain relation in this kind of plastics is more or less linear [33, 34]. Also, the experienced strain will remain small ($< 0.5\%$). Therefore, it is likely that the recovery from the creep will approach 100%.

Finally, it is assumed that all the channels and voids are uniformly and entirely filled. Likely, this will not be the case in reality (chapter 3). Therefore, the change in channel cross-section does not necessarily mean that the conductor undergoes the exact same change in cross-section. Additionally, in many strain gauges more resistance change is generated by the change in resistivity than by the change of dimensional parameters [35–37]. The modeled resistance change will therefore probably not be close to the resistance change resulting from experiments. It is however believed that, provided that the conductor is uniformly spread over the length of the channel, the design principles arising from this way of modeling are useful for building a sensor because the strains are present in the membrane and will be passed on to the conductor because it is in contact with the channel walls.

2.6 Conclusion

A 3DOF force sensor has been presented based on a circular membrane with an inclusion in the middle. The sensor will measure both normal and shear forces applied to the top center of the inclusion in a differential manner. This is done by incorporating four sensing structures in the membrane. Each structure consists of a channel running to the middle of the membrane, ending up in a void which is the quarter of a circle. These channels will later be filled with a conductive substance such that they attain their conductive properties. The filled channels will be utilized for resistive and capacitive sensing at the same time.

The mechanical and electrical behavior of the sensor have been modeled. First some guidelines were set as to what size the sensor should be and which working range it should have; the diameter was determined to be 15 mm and the range of applicable forces should be 0–25 N.

First, a model was made to determine the deflections generated by normal and shear forces acting on the top center of the inclusion. It was found that for small deflections, the two modes of deflection resulting from the forces could be treated separately and could be combined after solving them utilizing the principle of superposition. The resulting deflection from a combination of normal and shear forces can be expected to be approximately 55 μm for design parameters as listed in Table 2.1. This means that the gap between the membrane and the bottom electrodes should be at least this large.

The radial strain in the membrane resulting from normal and shear forces acting on the top center of the inclusion was modeled as well. The strain in the membrane is dependent on the deflection and also the distance with respect to the neutral plane. It was concluded that the strain generated by normal forces has a circular symmetry whereas the strain generated by shear forces is anti-symmetric. Furthermore, it was found that the strain induced by normal forces changes sign at a specific coordinate $r = S$. This finding was used in designing strain gauges experiencing the same sign strain all along their path to the capacitor plate in the inclusion. Also, two strain gauges placed on alternate sides of the membrane which are each other's mirror-images in the neutral plane, experience the same strain as a result of shear forces applied to the inclusion and an opposing strain as a result of normal forces applied to the inclusion. When strain gauges designed in this manner are placed in a Wheatstone bridge configuration, the resulting sensor will be sensitive to normal forces and insensitive to shear forces. Finally, two channel cross-sections were compared with each other: a version with straight channel walls and a version with tapered channel walls. The tapered version has a higher resistance in areas with higher strain. This makes for a higher relative change in resistance compared to the straight version. The resistance change is expected to be in the order of several permille.

Finally, the capacitance change induced by the application of shear forces on the top center of the inclusion has been modeled. Each capacitor in the sensor is modeled as three capacitors in series as there are three layers of dielectrics between the two capacitor plates: A layer of printed material, the air gap and again a layer of printed material. The change in thickness of the air gap determines the change in capacitance of every capacitor. To calculate the changes in the air gap, the movement of the inclusion has been related to the deflection of the membrane. The equation following from these steps was used to find the optimal radius of the inclusion for a set membrane radius of 7.5 mm. The optimal inclusion radius was found to be 3.25 mm. The resulting capacitance changes are expected to reach a maximum of approximately 32 fF.

Several simplifications have been made in the modeling of the sensor. The first simplification is that the channels will not have a large influence on the stiffness of the membrane. This is permissible since the bulk of the membrane will still be a solid material and uncertainties in the stiffness will only alter the responsivity of the sensor and not so much the general behavior. Further, in the model an elastic material is used whereas the material in reality will be a viscoelastic material. This implicates that the character of the model shifts from static to quasi-static: A static force applied to the inclusion will not result in a static response of the sensor. Phenomenons as creep and hysteresis will be present in the membrane material. However, in the range of applied forces and strains the material mostly behaves elastic and creep is likely to recover to nearly 100%. This is why modeling is done using elastic material properties. Finally, it is assumed that the channels are uniformly and entirely filled. In reality, it is not known how exactly the channels will be filled. Also, it is not known how the resistivity of the materials changes. Therefore, it is likely that resistance change will follow a similar pattern as modeled, but the magnitude will be different.

Chapter 3

Conducting liquids

This section describes the different conducting fluids available which perhaps are suitable for filling the channels. Evidently, one important aspect of the fluid is conductivity. The output signal of a Wheatstone bridge is dependent on the source level. Additionally it is important that the bridge does not use a lot of power or become noisy. Typical values of the resistors in a Wheatstone bridge are therefore several hundreds to thousands of Ohms whereas the source level is around ten Volts [25]. This resistance value should be reached in channels which are several hundreds of micrometers high and wide, and about ten millimeters long. Another important aspect is that the liquids should be contained in the sensor and should remain there during the operation of the sensor.

3.1 Low melting point metals

Low melting point metals are widely used in 3D printing, tactile sensing and large strain sensors by researchers [4, 19, 21, 21, 38–45]. A well-known metal which is in the liquid phase at room temperature is mercury, but usage is avoided since this material is highly toxic. More environmentally friendly alternatives like low melting point metal alloys consisting of different constitutions of, amongst other metals, bismuth, lead, tin, gallium or indium are available. These alloys come in eutectic and non-eutectic variants. Non-eutectic metal alloys are ideal for FDM techniques because the different temperatures at which the components solidify make that the alloy has a melting range like a thermoplast. Sn(60%)Bi(40%) is an example non-eutectic metal alloy having a melting temperature in the same range of polymers processed in FDM (138 °C–170 °C)[4]. Eutectic alloys are perhaps more suitable for infusion in channels since they have a single melting point. While for some alloys this melting point is still too high to be compatible with some printing methods, there are also alloys which are in the liquid phase at room temperature. Popular examples of these are Galinstan [21, 39] and eutectic gallium indium [19, 38, 42–45]. The latter is popular in strain sensors because of its high surface tension [41]. What all low melting point metals have in common is that they do not have their gaseous phase at room temperature and also their low resistivities which lies in the order of $\mu\Omega\text{ m}$. Therefore, they are ideal for creating interconnections between electronic parts in 3D printed structures [19]. However, for creating passive electronic parts like resistors this is undesirable. Especially considering the resolutions 3D printers are capable of (see chapter 4).

3.2 Electrolytes and liquid salts

Electrolytes are solutions in which positive and negative ions are present making the solution conductive. The conductivity of electrolytes depends on the concentration of ions, their mobility, the viscosity of the solvent and the temperature of the solution. The conductive behavior of an ionic liquid is heavily dependent on the applied frequency. Figure 3.1 illustrates the equivalent electric diagram of an electrode-electrolyte-electrode interface [23]. A direct current applied to the electrodes causes the formation of double layers at the electrode-solution interface and the sensor will in part behave like a capacitor. Hence, to use the ionic solution as a strain gauge, working with alternating currents is required. For the resistance of the fluid to be dominant, frequencies starting from about 10 kHz can be used. The upper limit of the applied frequencies is dependent on the size of C_p , which largely depends on the layout of the electrodes. In practice this means an upper limit which lies in the megahertz to gigahertz range [46]. The use of electrolytes in a system has several implications. An electrolyte has an electrochemical window, which is the range of voltages that can be applied. When exceeding this range, reactions take place at the electrode-solution interface. An example of this is the electrolysis of water, which takes place at around 1.47 V [24]. All the half-reactions that can take place upon applying a potential have to be considered. Therefore, inert electrodes made of carbon or platinum for example, are imperative. Furthermore, there is the need for a proper sealing to contain the liquid in the channel. As a good sealing may pose problems solvents with lower vapour pressures may be used. To reduce the evaporation rate of water, glycerin can be added to the solution [46, 47]. Also, there are ionic liquids or liquid salts available which have extremely low vapour pressures [48]. A disadvantage of this is that low vapour pressure goes hand in hand with high viscosities and negatively influences conductivity [49]. Because the use of ionic liquids mainly complicates the design of the sensor they are not deemed suitable for the use in this research; An adapted electrical read out would have been needed, limitations in electrode material would have been imposed and precautions to not lose the substances due to evaporation would have to be taken.

3.3 Inks and paints

Inks and paints can play an important role in both the manufacturing technique as described in this report as in additive manufacturing as a whole. They are mostly found as particulate suspensions. These suspensions can be subdivided in three groups: Sus-

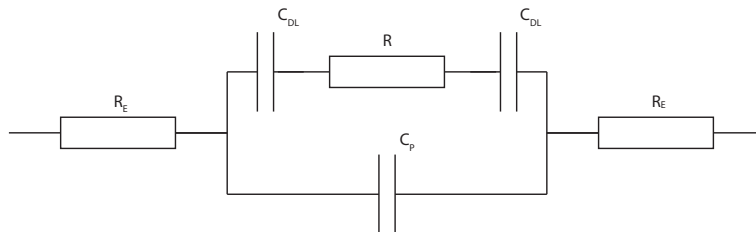


Figure 3.1: The equivalent circuit diagram for an ionic liquid. A Double Layer capacitance (C_{DL}) is present at the electrode-electrolyte contact. These are in series with the conductive ionic liquid which contributes to a certain resistance R . The electrodes have a capacitance which is parallel to the system C_P and a series resistance R_E .

pensions in which the carrier remains liquid after infusion [21], suspensions in which the carrier solidifies after infusion [50, 51] and suspensions in which the carrier evaporates after infusion [20, 22, 52]. The first two have as advantage that void spaces can easily be filled on the condition that the suspension remains monodisperse. When using a suspension in which the solvent evaporates, it remains uncertain where the particles will settle and voids will be present. This problem can partly be solved by repeatedly filling the channels after the solvent is evaporated [20].

Solidification can happen in different ways, light curing [51], resin developing [53], evaporation of solvents [54]. One way can have an advantage over another. If the liquid is cured by light for example, one can cure the liquid on the application of light instead of waiting for evaporation of the solvents on the one hand or prematurely drying of the liquid on the other.

Inks and paints have a wide range of possible resistivities. Not only is there a diverse array of conductive particles available such as silver, gold and several allotropes of carbon [6, 7, 55–58], also the ratio of filler content to the entire solution can be altered to get the desired conductivity [21, 58]. Furthermore, due to high surface-area-to-volume ratios, the melting point of materials can be reduced promoting sintering between the particles under mild conditions, leading to resistivities close to the bulk-resistivity of the material [7, 49]. A condition for using this technique is that the 3D print can suffer the elevated temperatures needed for this.

Particulate tracks generally have high gauge factors. Next to the change in geometry of the conductive track, changes in resistivity can be observed. This can be ascribed to numerous connections and disconnections between neighboring nano- or micro-particles. While this effect makes for higher gauge factors, it is also to the cause for hysteresis effects and drift in the absolute value of the strain gauges. Drift is said to be the result of permanent cracks in the conductive track on the microscale [36, 55, 56].

In this research, for convenience there will only be looked at pre-made liquids which do not stay liquid. The latter requirement makes containing the particles in the printed structures easy. Metal based paints and glues generally give a resistance which is too low to simply use in a Wheatstone bridge. Two types of conductive fluids containing allotropes of carbon and having different characteristics will therefore be tested. The first liquid is a water based thixotropic gel containing graphite particles (Pelco Conductive Graphite 16051, Tedpella Inc, United States). The gel contains 13% solids by volume with a mean particle size of about 1 μm . Its surface resistivity is 30–300 $\Omega \square^{-1}$ for a layer of 25.4 μm depending on the method of application and the drying temperature. The viscosity characteristics are not known, but it being a thixotropic gel means that upon applying pressure when infusing the channel, the viscosity of the liquid lowers. This is a favorable effect when filling the channels. Once infused, the water has to evaporate for the paint to dry and a track of graphite particles is formed. The second liquid is a carbon conductive glue with an acrylic binder (Pelco Conductive Carbon Glue 16050, Tedpella Inc, United States). Once the carrier, acetone, is evaporated, the glue forms a conductive track with graphite and carbon black which is held together by acrylic resin. The glue contains about 17% conductive particles by volume with a particle size of 5–10 μm . The sheet resistance is 47 $\Omega \square^{-1}$ for a 25.4 μm thick layer. The viscosity is 9500 mPa.s. Due to the high vapor pressure of acetone the glue is dry to touch in several minutes (3–5 min).

Calculating the resulting resistances of filled channels is complicated since calculations heavily rely on a lot of unknown parameters. These parameters include the monodispersity of the liquid, the distribution of the particles over the volume, the porosity and the

resulting networks. Therefore, only some rudimental calculations can be done. For the graphite paint, one can assume a $160\ \mu\text{m}$ (h) by $510\ \mu\text{m}$ (w) by $10\ \text{mm}$ (L) channel, which is only filled for 10% with graphite particles since 90% of the fluid is water. Then it could form a $16\ \mu\text{m}$ layer of graphite particles over the whole width and length of the channel. If then the surface resistivity is scaled by $\frac{25}{16}$, one could expect the piece of channel to have a resistivity in the range of about 1–10 k Ω .

A similar calculation is performed for the conductive glue. It is however unknown what volume fraction evaporates from the glue when it is dried. A simple estimation would be to assume a $25.4\ \mu\text{m}$ layer over the length and width of the channel. The described channel would have a resistivity of $47\ \Omega\ \square^{-1}$ and the channel would have a resistance of approximately 1 k Ω .

3.4 Conclusion

The liquids introduced in this chapter will be used in a Wheatstone bridge configuration and have to be contained in channels in the sensor. Keeping the future purpose of the conducting liquids in mind, three different types of liquids have been introduced in this chapter.

Low melting point metals generally have very high conductivities. Also, they do not have their gaseous phase at room temperature. Therefore, these metals are very useful in applications similar to the one described in this report: Utilizing channel filling, low resistance connections can be made between various integrated parts in a 3D print. However, the liquid metals have a resistivity which is too low to form resistors. Especially keeping in mind the resolution of the printer chapter 4.

The second category of liquid conductors introduced is electrolytes and liquid salts. The advantage of electrolytes is that the conductivity can be tailor made by adding a certain concentration of positive and negative ions. However, the utilization of these types of liquids brings along several complications in the design of the sensor. The conductive behavior of an ionic liquid is heavily dependent on the applied frequency. Also, the electrochemical window limits the range of applicable voltages and thus the sensitivity of the sensor. Further, the use of inert electrode materials is imperative because of half-reactions which possibly take place at the electrode interface. Finally, containing the fluids in the channels may pose problems as they tend to evaporate. This disadvantage can partly be solved by using fluids with low vapour pressures such as liquid salts but this negatively influences the conductivity. Thus, electrolytes and liquid salts are not deemed suitable for the use in this research.

Inks and paints are finally introduced as possible candidates to be utilized in this research. This category has got a wide range of applicabilities as the inks and paints come in many different forms. Carriers can stay liquid, solidify or evaporate. The use of different sorts and concentrations of particles make for adaptable resistivities. Further, particular tracks are often used in strain gauges for their high gauge factors. It was found that pre-made suspensions containing allotropes of carbon are the most suitable for this research mainly because their resistivities fall in the preferred range. Two different liquids have been chosen with different properties: graphite paint and carbon glue. They do both not remain liquid which makes containing them in the sensor easy. Their resistivities lie in the same range and therefore the main differences are the way they cure and the particle size. The graphite paint is a water based paint and the water will evaporate. A

porous particulate track is left. The mean particle size is 1 μm . The solvent in carbon glue is acetone. Once acetone evaporates the acrylic resin cures and flexible layer with conductive particles is left. The particles found in this suspension have sizes in the range of 5–10 μm .

Chapter 4

Fabrication of the sensor

This chapter describes the fabrication process of the sensor. It concerns the printing technology used for building the part, the infusion of the channels and the way the chip is interfaced with the outside world.

4.1 3D printing processes

Additive manufacturing processes build up a product by stacking two dimensional layers on top of each other. This can be done starting at the top of a product or the bottom. Traditional subtractive techniques begin with a block of material and get rid of unwanted material and opposed to additive manufacturing create a lot of waste material. Additive manufacturing is therefore seen as a very efficient and green process [1]. Other characteristics of additive manufacturing include the ability to easily adapt products to the needs of the individual and a high degree of freedom in designing three dimensional shapes. The number of different 3D printing technologies has rapidly increased over the last few years. While it is becoming more and more difficult to classify the different technologies, attempts have been done. The American Society for Testing and Materials (ASTM) classified the additive manufacturing technologies in seven main categories: Vat polymerization, material extrusion, powder bed fusion, directed energy deposition, sheet lamination, material jetting and binder jetting [2].

In this project two characteristics are paramount for successfully printing the structures: High resolution and easy removal of support material. The combination of these two characteristics is only found in technologies using material jetting. Material jetting methods are additive manufacturing techniques which directly originate from two-dimensional ink-jet printing techniques. Parts are built up by dispensing small droplets just like it is done in ink-jet printers, yet a third dimension is added. After a layer is formed, the substrate lowers one layer thickness, and another layer is stacked on top of the current layer. Often, layers are milled before the next layer is added to make sure the surface is flat. Several machines using this technique are commercially available, like the Objet Connex of Stratasys and the Projet of 3D systems. The Projet series of 3D Systems contains printers that dispense acrylic photopolymers. After a layer is formed, the layer is cured by flashing with ultraviolet light (Figure 4.1). The printing head carries hundreds of nozzles, enough to cover the entire x-axis. With a single move in the y-direction an entire layer can be deposited. Half of the nozzles is for part material, and half for the support material. Support material is used for voids and supporting overhanging structures. In the case of a Projet it is a wax which is deposited in a molten state and

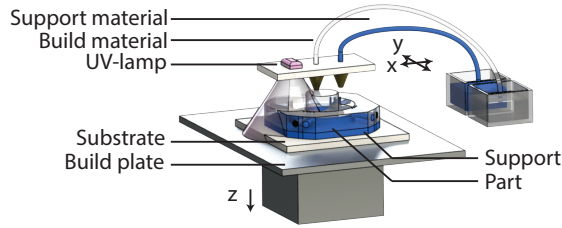


Figure 4.1: Basic representation of the printing process as used in the Projet. Adapted from [59].

solidifies on impact. It is this wax support material combined with the high resolution that makes this particular printer ideal for printing micro fluidic channels. Once printed, the support material can be liquified by putting the part in an oven and removed with the use of pressure. Washing with olive oil or ethanol removes the remainders. Some characteristics important for this project are listed in Table 4.1.

4.2 Channel filling

Two methods of channel filling have been considered, capillary filling and filling by a pressure driven flow. Both methods have been evaluated for a channel with height $h = 2b = 160 \mu\text{m}$, width $w = 2a = 510 \mu\text{m}$ and a length of $L = 40 \text{ mm}$. The channel cross-section is shown in Figure 4.2. The surface roughness of the channel as well as the possible influence of the particles in the fluid behavior are not taken into account in these evaluations. The main requirement for filling the channels is speed, as especially the carbon glue dries within minutes.

4.2.1 Capillary filling

In small channels the combination of adhesive forces between the channel walls and the liquid and the surface tension of the fluid can cause the liquid to flow in the channel. Some calculations are done to assess the viability of filling 3D printed channels with the paints described in chapter 3. In this example, a rectangular channel is taken in which

Table 4.1: Characteristics of the Projet 3500HD max and its build material [20, 60].

Machine	
Resolution	750x750x1600 DPI (xyz)
Accuracy	0.025–0.05 mm per 25.4 mm
Build material (VisiJet Crystal)	
Density	1.02 gcm ³
Young's modulus	1.463 GPa
Poisson's ratio	0.35
Relative Permittivity	6
Support material (VisiJet S300)	
Melting point	60 °C

$a \gg b$ (Figure 4.2). If an infinite source of fluid is assumed the capillary flow in a channel is expressed by the following equation [61]:

$$R_f = \frac{2k_{shape}\mu\Delta x}{D_h^2 A} = \frac{\Delta P}{\phi_v} \quad (4.1)$$

In which R_f is the hydraulic resistance (Pasm^{-3}). k_{shape} is a constant which depends on the channel shape. For channels with cross-sections like the one taken in this example its value is 24. Furthermore, μ is the viscosity of the liquid (Pa·s), Δx is the distance traveled in the channel (m), A is the cross-sectional area of the channel (m^2), ϕ_v is the volumetric flow rate (m^3s^{-1}) and ΔP is the Laplace pressure defined as [62]:

$$\Delta P = \gamma\left(\frac{1}{R_x} + \frac{1}{R_y}\right) = \gamma \cos\theta\left(\frac{1}{a} + \frac{1}{b}\right) \quad (4.2)$$

in which γ is the surface tension of the fluid (Nm^{-1}), θ is the contact angle of the fluid with the channel walls (indicated in Figure 4.2) and R_x and R_y are the radii of curvature of the meniscus (m). D_h is the hydraulic diameter which can be expressed as:

$$D_h = \frac{4A}{L_P} = \frac{4(2a2b)}{2(2a + 2b)} = \frac{4wh}{2w + 2h} \quad (4.3)$$

In which A is again the cross-sectional area (m^2) and L_P is the wetted perimeter (m). For channels in which $a \gg b$, this reduces to:

$$D_h \approx 4b \quad (4.4)$$

Finally, ϕ_v is the volume flow (m^3s^{-1}), for this channel defined as

$$\phi_v = 4ab \frac{dx}{dt} \quad (4.5)$$

Combining 4.2 to 4.5 into one equation, replacing x for the length L of the channel and solving for t yields:

$$t = \frac{3L^2\mu}{2b\gamma \cos\theta} \quad (4.6)$$

This relation can be used to calculate the time needed to fill a channel using capillary forces. To accurately describe the time needed to fill a channel, the viscosity of the fluid, the surface tension and the contact angle of the fluid with the channel walls is needed. Except for the viscosity ($\mu = 9500 \text{ mPa}\cdot\text{s}$) these are absent in the datasheet of the paint and glue. However, using an optimal contact angle in which $\cos\theta = 1$ and the surface tension of water at room temperature which is about 72 mNm^{-1} [63], an estimation can be made how long it would take to fill a channel using capillary force. These parameters would lead to a filling time of 0.55 h. During this time the liquids would have solidified so this leads to the conclusion that capillary filling is not an option in this project.

4.2.2 Pressure driven flow

For pressure driven flows in rectangular channels at low Reynolds numbers the volumetric flow rate of the fluid (m^3s^{-1}) and the pressure difference (Pa) between two points are related by [64]:

$$\Delta P = \phi_v R_f \quad (4.7)$$

In which R is the fluidic resistance ($\text{kgm}^{-4}\text{s}^{-1}$). For rectangular channels in which ($\frac{w}{h} > 1$) R is defined as:

$$R_f = \frac{\alpha\mu x}{wh^3} \quad (4.8)$$

Where μ is the viscosity of the fluid (Pas), x distance between the two points considered (m), w the width of the channel (m), h the height of the channel (m), and α is a dimensionless parameter that depends on the aspect ratio $\frac{w}{h}$ as:

$$\alpha = 12\left(1 - \frac{192h}{\pi^5 w} \tanh \frac{\pi w}{2h}\right)^{-1} \quad (4.9)$$

The volumetric flowrate can again be expressed as in 4.5 and this leads to solving resulting equation for t :

$$t = \frac{\frac{a\mu}{2h^2}x^2}{\Delta P} \quad (4.10)$$

The pressure difference will be generated by a human thumb pressing on the plunger of a syringe having a certain radius r :

$$\Delta P = \frac{F}{\pi r^2} \quad (4.11)$$

Assuming around 5N of force is generated and the plunger of the syringe has a radius of 2.5mm and again taking $\mu = 9500 \text{ mPas}$ yields a filling time of approximately 17s. The validity of this calculation also depends on the Reynold number of the system, which should remain low (< 1000). The Reynold number is defined as:

$$Re = \frac{\rho V D_h}{\mu} \quad (4.12)$$

In which ρ is the density of the fluid (kgm^{-3}), V the average velocity of the fluid (ms^{-1}), also defined as the ratio of the length L of the channel (m) to the time t it took to fill the channel (s), D_h is again the hydraulic diameter (m). In this example the Reynolds number is $Re \approx 6 \cdot 10^{-6}$

4.3 Interconnects

From preliminary experiments (Appendix H) a set of requirements has been drawn up which the interconnects have to meet.

- Post-processing the chip should remain possible. When the chip comes from the printer, all the channels are filled with support material. After the wax support is liquified by putting the part in the oven, it should be removed by flushing the

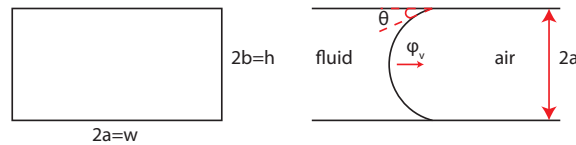


Figure 4.2: On the right the channel cross-section. On the left a longitudinal section of the channel with some relevant parameters for capillary filling of the channel.

channels with oil. The fluidic resistance of the inlets for the interconnects is much lower compared to the fluidic channels because they will be shorter and have larger diameters. The oil will leave the part directly via those inlets instead of going through the rest of the channels. Therefore it should remain possible to close the inlets of the interconnects to remove the support material from the rest of the channels. This may be temporarily but also permanently as described in the remainder of this paragraph.

- The addition of connections should not be too time consuming nor need a lot of wire assemblies to connect them to the measurement devices. The possibility of integrating standard male connectors in the chips on which standard receiving ends can be placed is evaluated.
- The chance of bubble inclusion should be minimized. The fluid should therefore only pass the connector on one side. If the fluid were to pass the connector on both sides, asymmetries in the placement of the connector can cause the inclusion of bubbles in the particulate track, which negatively influences the conductivity.
- The connector should not leave any space for the conductive liquid to go other than in the channel.
- Contaminations which may enter via the the inlets of the interconnects should not block the channel when the connectors are inserted.

All these requirements have been implemented in the design shown in Figure 4.3. The design makes use of an interference fit of the connector in the dedicated connector inlet. Cylindrical gold plated connectors are used having a diameter of 0.46 mm which are pressed in the connector inlet of 0.4 mm after the wax support is liquified. The pin continues a little further after it has reached the channel. This has the advantage that contaminations which might have entered the access hole are pressed past the channel. The channel sits around the pin on one side which minimizes the chance of bubble inclusion. At the interface of the channel with the connector the channel height is increased to twice its original height to increase the contact surface with the pin. Because the pin is gold plated, the contact resistance cannot deteriorated by oxidation. After the connectors

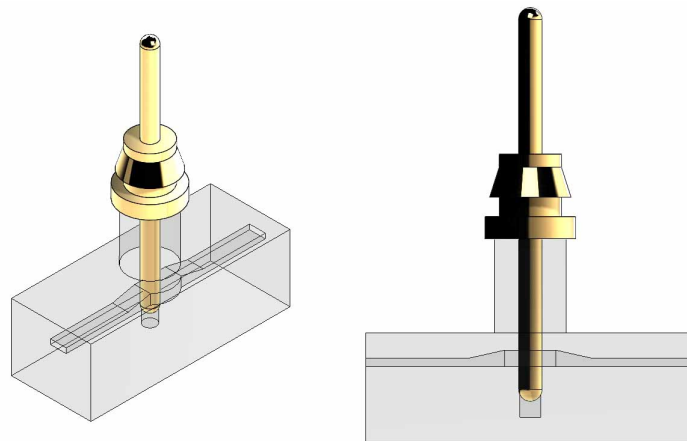


Figure 4.3: Two views on the channel layout around the interconnect.

are inserted, the remaining wax can be removed from the channel as the connectors now block the connector inlets. The press fits also make sure that the conductive liquids can only sit in the channels and not enter the connector inlets. Finally, the use of standard connectors simplifies the readout since standard receivers can be attached.

4.4 Conclusion

Several aspects of the fabrication of the sensor have been presented in this chapter.

First, the 3D printing technology to be utilized for the sensor has been determined. Two characteristics of the 3D printing technology are paramount for successfully printing the proposed structures: A high resolution and a support material that can easily be removed from cavities and channels. Only one technology meets the requirements. Printers using material jetting generally have high resolutions in comparison to other printing techniques. In particular, the Projet series of 3D Systems is found to be suitable. These printers dispense acrylic photopolymers with a resolution of up to $750 \times 750 \times 1600$ DPI (xyz). Additionally, the support material used in these printers is a wax. This wax can be liquified by putting the printed part in an oven and removed from channels with the use of pressure. Both the resolution and the support material make the Projet HDmax 3500 3D printer the ideal printer for utilization in this project.

Two methods of infusion of the channels have been evaluated: Capillary filling and filling with a pressure driven flow. The main concern for applicability of either of the filling techniques is speed as the carriers in the liquids to be used evaporate within minutes. Capillary filling did not meet the requirements as filling a channel similar to the ones later used in this project would take up to approximately half an hour. On the contrary, pressure driven flows will be able to fill up a channel within tens of seconds. Therefore, it is decided to use pressure driven flows to fill the 3D printed channels.

Finally, a technique is introduced which supposedly successfully interfaces the filled channels with measurement equipment by press fitting connectors in the 3D printed part. Several precautions are taken to warrant the quality of the particulate tracks: The chance of bubble inclusion is minimized because the fluids only pass the connector on one side. The connectors do not leave any space for the conductive liquid to go other than in the channel. Contaminations are pressed past the channels which minimizes the probability of channel blockades. Further, interference fits makes that post processing remains possible; connectors are inserted before any further post processing is done. This closes off the connector inlets and opens up the opportunity to later remove the support material from the rest of the channel. Inserting a standard connector in the interference fit only includes one step and the chip can easily be interfaced with other electronic equipment. This reduces the time of assembling a chip drastically. Cylindrical gold plated headers are chosen because cylindrical press fits work best and the contact resistances will not be deteriorated by oxidation.

Chapter 5

Experimental section

This chapter describes the different steps in characterizing the 3D prints, filling of the channels, the resulting resistances and testing the fabricated strain gauges.

5.1 Experiment 1: Determining the minimum channel size

To determine the minimum channel dimensions achievable by the Projet 3500HDMax, the part shown in Figure 5.1 is designed. The part has eleven channels going through a membrane. The channels have a layout comparable to those of the sensors which will be built later. Each channel has a 6 mm long inlet and outlet with a diameter of 1.6 mm, gradually tapered until it has the channel dimensions of h by w . The channels have different heights and widths, the aspect ratio varying from approximately 1 to approximately 3, Table 5.1. The heights and widths are multiples of the printer's resolution, being 16 μm in the z direction and 34 μm in the x and y direction. Except for channels 1 to 3, which have a height of 50 μm , the minimum feature size according to Rapidcenter (Rapidcenter, The Netherlands), a platform for 3D printing. This is the company at which the 3D prints are ordered. Once printed, the first post processing is done by Rapidcenter and consists of removing the support material. However, on the inside of the channels and inlets some wax remains. The part is put in the oven at 60–65 $^{\circ}\text{C}$ until the wax is melted. Then, the channels are cleaned by flushing the channels with olive oil. Subsequently, the channels and part are flushed with and immersed in deionized water with dish washing soap. Next the part is cleaned with pure deionized water followed by flushing with ethanol. The ethanol is removed with deionized water again since ethanol not only dissolves the support material but also the part itself is slightly dissolved. In the remainder of the text this process is referred to as a cleaning or post-processing step. In this experiment it is simply checked which channels can be opened up by the cleaning step and which remain closed.

Table 5.1: Dimensions of the channel cross-sections of the part presented in Figure 5.1

Channel	1	2	3	4	5	6	7	8	9	10	11
h (μm)	50	50	50	112	112	112	160	160	160	208	208
w (μm)	68	136	204	136	272	408	170	340	510	442	646

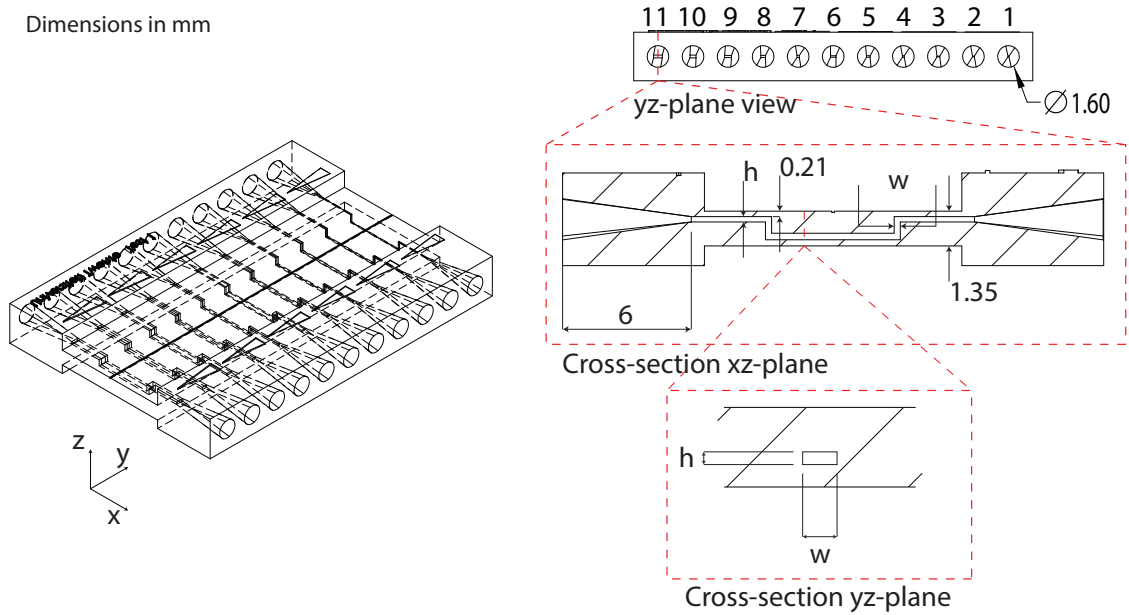


Figure 5.1: Design of a chip with eleven channels with varying channel dimensions. h and w can be found in Table 5.1.

5.2 Experiment 2: Determining the minimum membrane thickness

It is important to have an idea about what membrane thicknesses can be achieved by the printing technique as the thinner the membrane, the more sensitive sensors can be made. Strain gauges experience the highest strain at the surface of a bent membrane. Capacitors in the printed structure are modeled as three capacitors in series and the higher the capacitance of the printed membranes - that is, the thinner the membranes are - the more apparent the capacitance of the air gap is. To get an idea of the minimum thickness of a printed membrane, the structure depicted in Figure 5.2 is designed. It is part of a larger test structure. The membrane is 8.40 mm by 3.5 mm and covers a void with height 350 μm . The membrane has three different thicknesses being 50 μm , 100 μm and 150 μm . An inlet has been added on which the syringe can be connected to flush the void and an outlet through which the support material can exit the void. The chip is printed using the Frosted Extreme Detail option of Shapeways (Shapeways BV, The Netherlands). Selecting this option means that the parts are printed by a ProJet 3500HDMax using the highest resolution. After the print is received, the cleaning step is performed. The next thing is breaking the membrane out of the printed part, and inspecting the different thicknesses using a Scanning Electron Microscope (SEM).

5.3 Experiment 3: Analyzing channel and contact resistances

To characterize the built resistances, the chip shown in Figure 5.3 is designed. It is a 50 mm by 42.93 mm by 2.16 mm part containing twenty channels. Each channel has a 6 mm long inlet and outlet with a diameter of 1.6 mm, gradually tapered until it has the channel dimensions of 160 μm (height) by 510 μm (width). The chip contains alternately

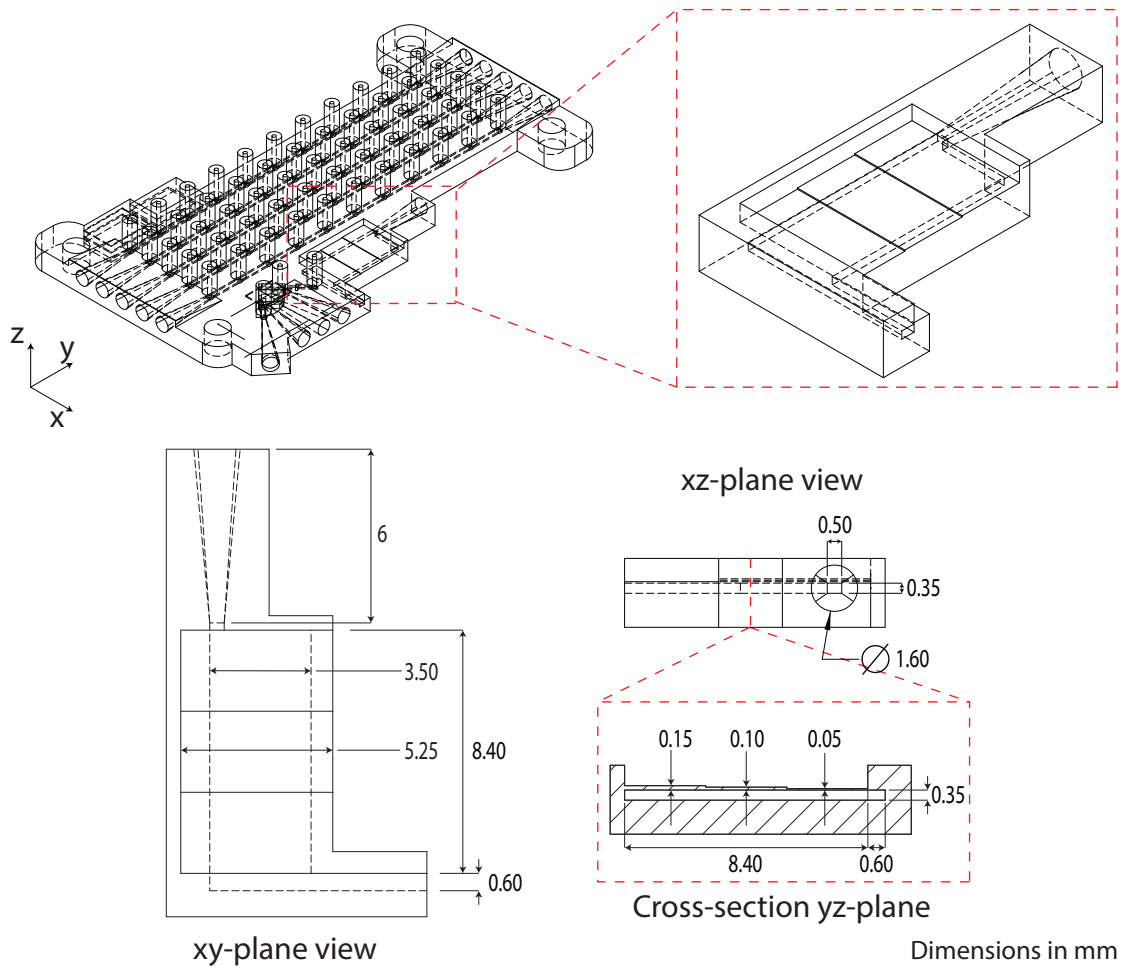


Figure 5.2: The printed membrane is part of a larger structure. The membrane is highlighted and shown as a separate part for clarity. The membrane has three thicknesses: 50 μm , 100 μm and 150 μm .

five plain channels and five channels with holes for the connectors. The five plain channels are included to compare the filling process with the channels with interconnects; if any hiccups occur in the channels with interconnects, the culprit can be the layout of the channel.

The chip is printed using the Frosted Extreme Detail option of Shapeways. The part is put in the oven at 60–65 $^{\circ}\text{C}$ until the wax is melted. Before performing the post processing, the BBS-132-G-A (Samtec Inc, United States) gold plated headers are inserted in the interference fits. After the part and the channels have dried after cleaning, the channels are ready to be filled with conducting fluid. The process of drying can be accelerated by venting with N_2 . Then, one half of the channels is filled with graphite paint whereas the other half will be filled with carbon glue. This is done using a 1 ml syringe (BD Plastipak REF 303172, Becton Dickinson S.A., Spain). Before sucking the conducting liquids into the syringe, the paint is stirred for one minute and the glue is shaken for one minute. After the paint is sucked in the syringe, a pipette tip (Eppendorf ep.T.I.P.S. Standard volume range 2 μl –200 μl) is placed on top of the syringe. The tip is appropriated by cutting about 5 mm from one side to make the fit with the syringe, and 2 mm from the front to reduce the pressure loss and make a better fit with the chip inlets. The channels are all infused from the same side of the chip.

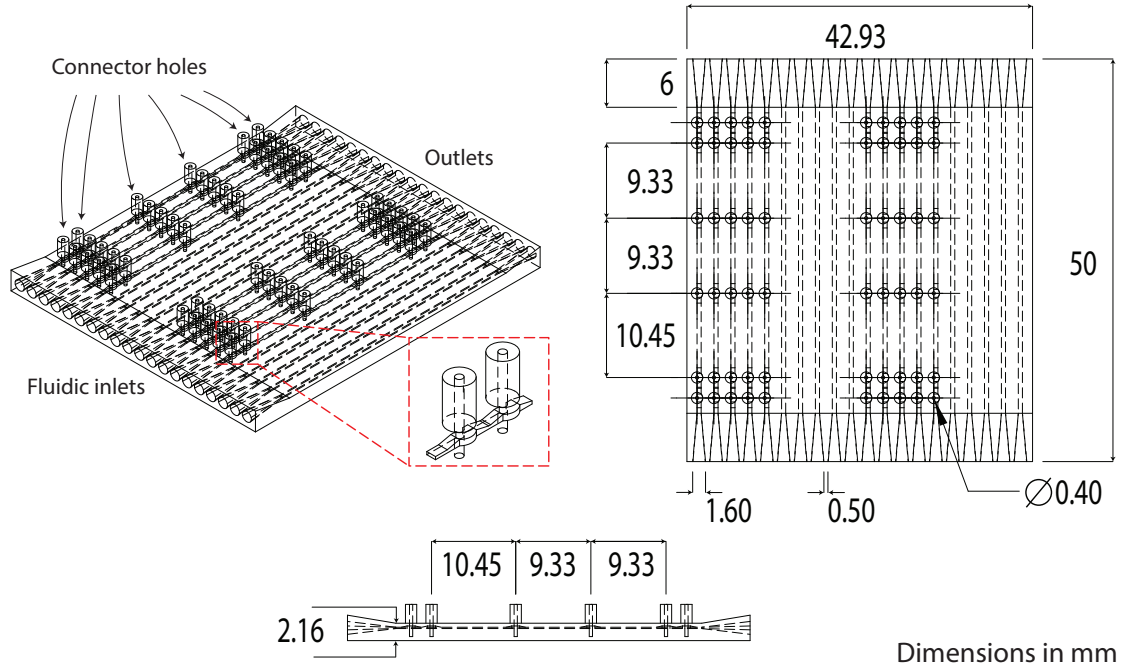


Figure 5.3: Design of a chip with twenty channels of which ten plain channels and ten channels with interfacing.

The channels with interconnects can be used for 2-wire and 4-wire measurements. A schematic for the setup is shown in Figure 5.4. The two outermost pins of the built resistances are used to measure the voltage. The connector closest to the fluidic inlet being the positive side of the measurement. The pin closest to the negative pin of the voltage measurement is used as a current outlet while the remaining three pins are used as current inlet. With the current and the three voltages with respect to the common pin known, the resistance from those pins to the current outlet can be calculated. When switching between a 4-wire and a 2-wire measurement, the resistance excluding and including the contact resistance is known. This way a measure for the quality of the interface between the connector and the fluid conductor is obtained. The device used for the measurements is a Keithley 2602 System Sourcemeter (Tektronix, Inc, United States). The settings are shown in Table 5.2. The four wires of the sourcemeter are connected to the correct connections of a particular channel by means of a HP 34970A Data Acquisition/Switch Unit (Hewlett Packard, United States) accommodating two Agilent 34901A multiplexers (Agilent Technologies Co Ltd, United States). The two devices are controlled by Labview (National Instruments Co, United States) on a PC. For each measurement, the current source is switched on after the switches of the multiplexer are thrown. Then, after a delay of 300 ms a measurement is performed. A 4-wire and a 2-wire measurement are

Table 5.2: Settings for the Keithley 2602 System SourceMeter.

Source (range)	Current (1.000 00 mA)
Measure	Voltage
Limit	40 V
Speed	Hi-Accuracy
Filter	Average, Repeat, 5x

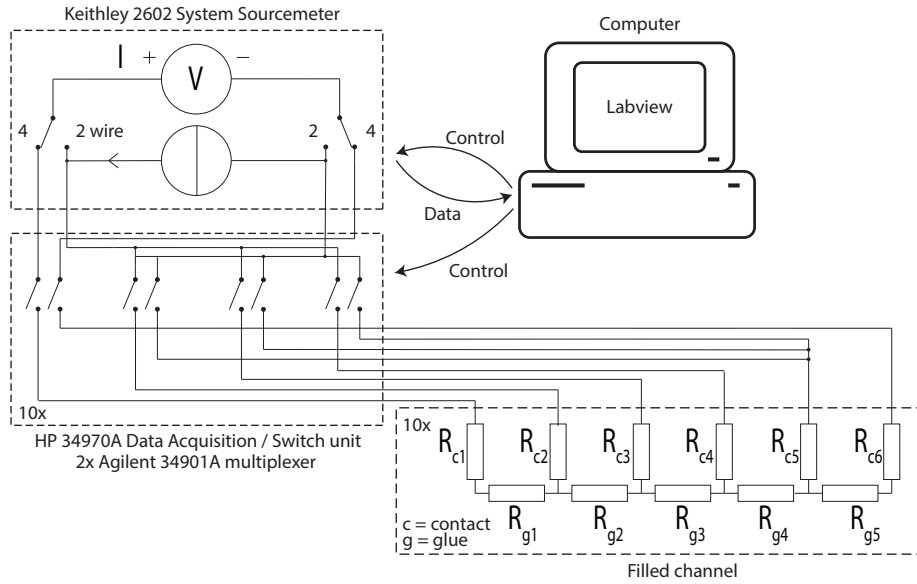


Figure 5.4: Measurement setup to do a 4 and 2 wire measurement on all ten channels. A computer makes sure that the matrixboard connects the sourcemeter probes to the correct pins of the filled channel and then collects the data.

subsequently performed following the described procedure. Currents from -1 mA to 1 mA and vice versa are applied in a logarithmic manner, the smallest step being 100 nA. The same experiment is performed twice with 23 days in between to assess the stability of the built structures over time.

5.4 Experiment 4: Using the channels as strain gauges

To see how the developed concepts of building strain gauges turn out in reality, a doubly clamped beam with ten channels has been developed (Figure 5.5). This structure is designed to be able to compare a multitude of channels in one structure. Because this beam is different from a circular clamped plate, modeling is done in Appendix E along a same line of reasoning as done for the circular plate. The beam contains ten channels of which five are mirrored in the neutral plane with respect to the other five. This way, the response for both compressive and tensile strain is compared for similar loads. The connectors have been placed as close as possible to the membrane to acquire an optimal signal. Two sensors have been prepared with graphite paint and two with carbon glue. The sensors have different beam thicknesses t and channel offsets z from the neutral plane; $860\ \mu\text{m}$ with a channel offset of $300\ \mu\text{m}$ and $1260\ \mu\text{m}$ with a channel offset of $450\ \mu\text{m}$. These difference in designs were mainly made to have one design which is on the edge of what is achievable with the printer and one more conservative design.

To measure the change in resistance for different loads, the measurement setup shown in Figure 5.6 is made. For applying loads, a PM50 (MB Dynamics, United States) voice coil is used fed by a Agilent E3631A (Agilent Technologies Co Ltd, United States) current source. This voice coil is connected to an air bearing with an aluminum rod. This air bearing contains a 1022M-3M-F-106 (Tedeia Ltd., Israel) load cell which is connected to a plunger and a P10 (Sylvac SA, Switzerland) displacement sensor. The displacement

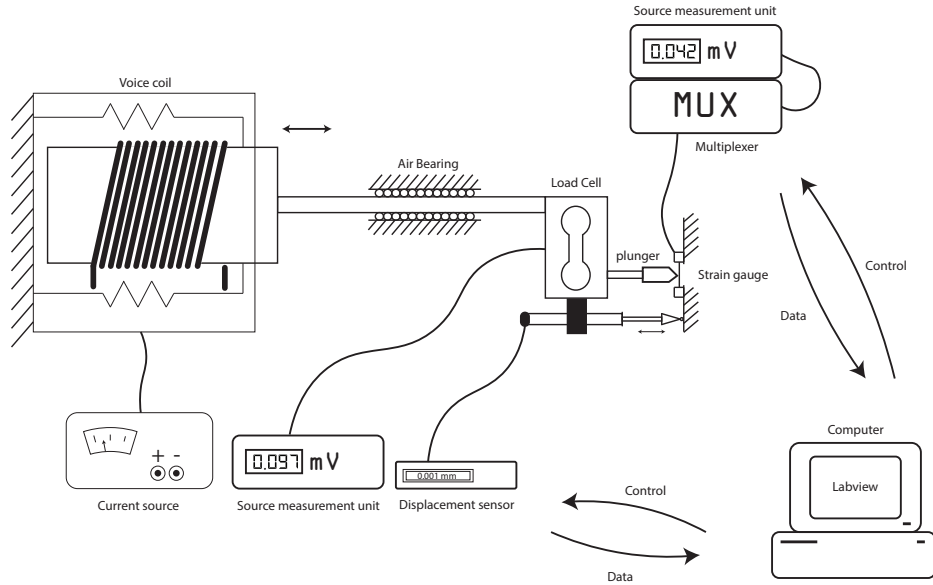


Figure 5.6: Measurement setup to analyze the response of the strain gauges. A voice coil actuator is connected to a load cell via a rod which slides over an air bearing. On the other side of the load cell a plunger is connected which is pushed on the strain gauge. The system is set to a certain force after which the resistance of the ten channels, the load cell and the displacement sensor are read out.

outcome will be compared to the response of the straight channels.

5.6 Experiment 6: Designing a circular 3DOF sensor

An onset has been made to the design of a 3DOF sensor (Figure 5.8). The parameters as described in the text will be used in this design. That is, the membrane will have a diameter of 15 mm, the inclusion will have a diameter of 6.5 mm, the inclusion will have a height of 3 mm and the membrane will be 1 mm thick. Also, the sizes of the channels will be as described in the text (Table 2.2). The air gap and the printed layers of material are designed conform Table 2.3. Each resistive channel has four connectors to be able to connect four wires for resistive measurements (Figure 5.9). Further, these four pins can be used to apply driving voltages in a capacitive ratio measurement [26]. The bottom plates contain two connectors to keep the influence of the resistance as low as possible during capacitance measurements. Between the drive pins and the pins of the bottom plates, holes are added in which ground pins are plugged. This prevents parasitic

Table 5.3: Settings for the Keithley SourceMeters.

Keithley 2600		Keithley 2410	
Source (range)	Current (100.000 mA)	Source (range)	Current (1.000 00 mA)
Measure	Voltage	Measure	Voltage
Limit	40 V	Limit	20 V
Speed	Normal	Speed	Fast
Filter	None	Filter	None

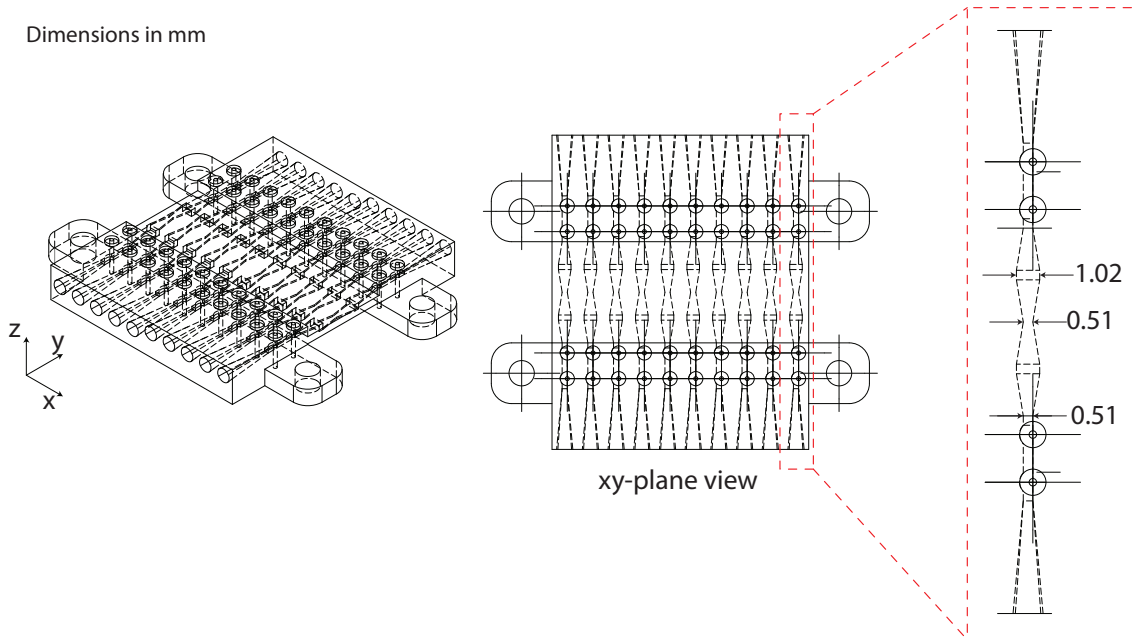


Figure 5.7: Strain gauge design with tapered channels. The only difference with respect to the design shown in Figure 5.5 is the width of the channels. The membrane is 860 μm thick.

capacitances between the drive pin and the sense pins of the bottom plate. This makes for a total of 36 connector inlets. To accommodate the resistive as well as the capacitive measurements, a printed circuit board is designed (Figure 5.10). This board fits the sensor, contains connectors for the four wire measurements and has the pre-amplifier of the charge amplifier implemented.

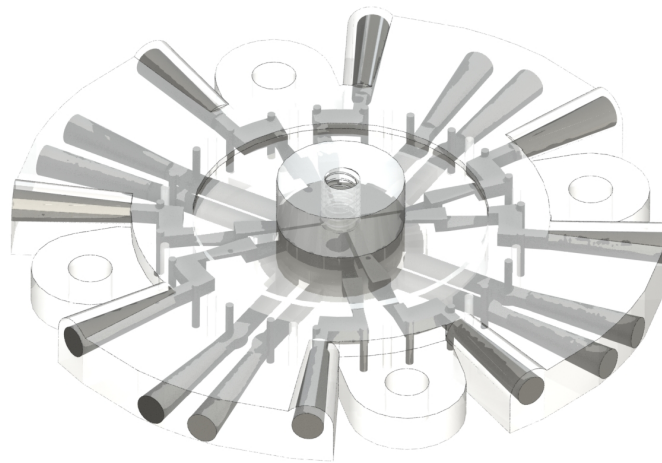


Figure 5.8: Design of a sensor implementing both a resistive and a capacitive readout.

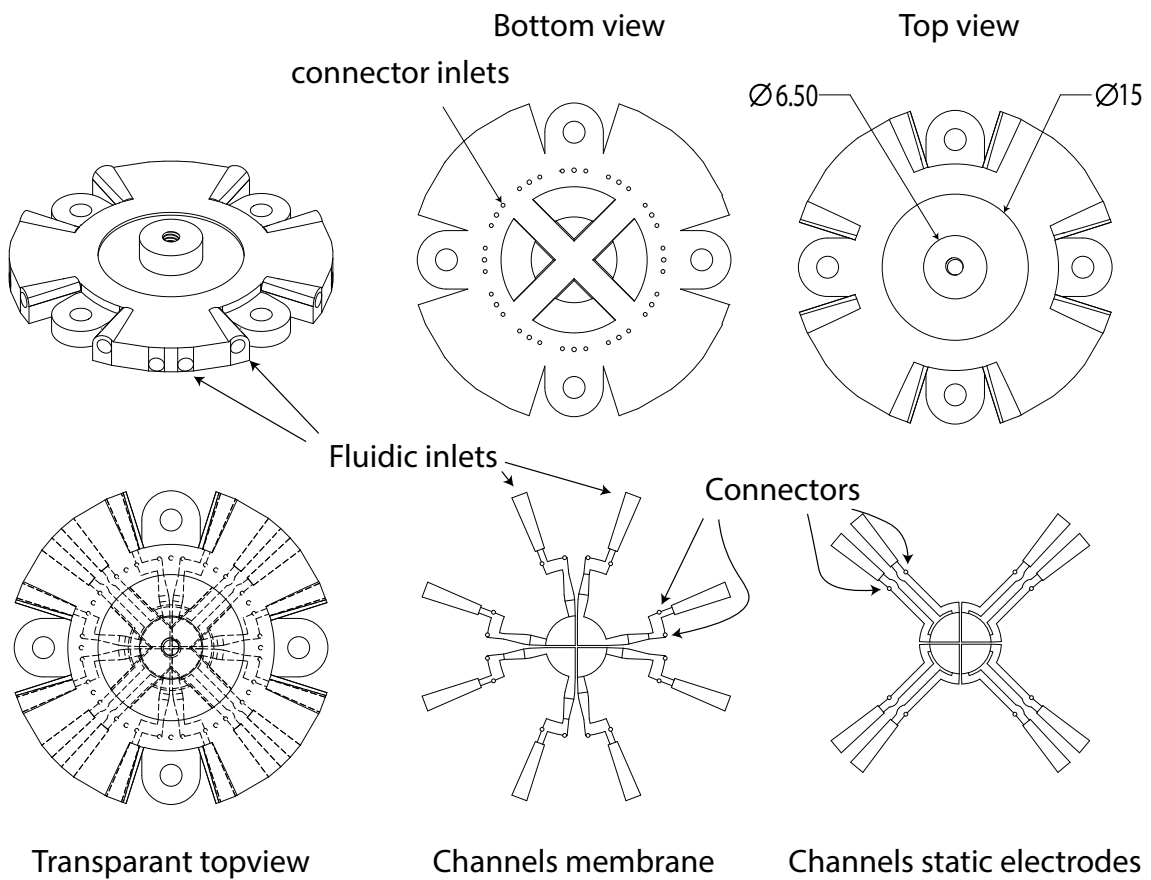


Figure 5.9: Different views on the designed 3DOF sensor. For clarity, the outside of the sensor is shown but also the channel shapes.

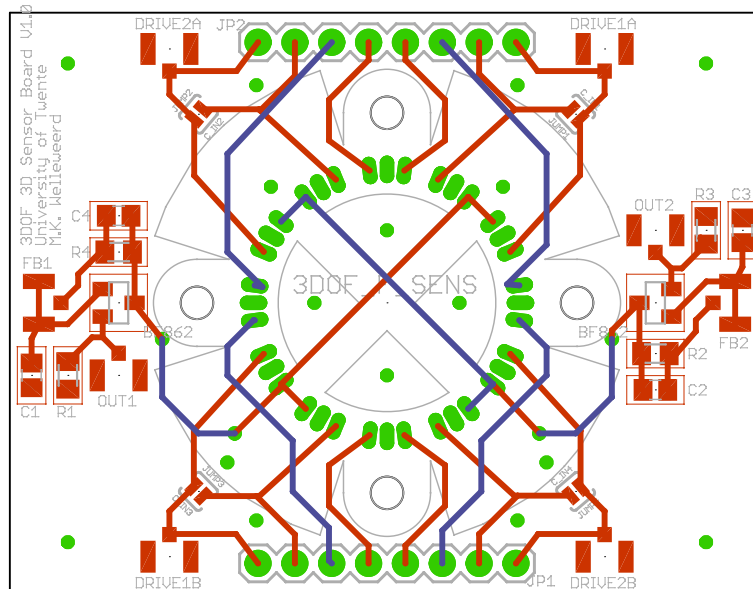


Figure 5.10: A vectorized version of the PCB designed for readout of the 3DOF sensor.

Chapter 6

Results and discussion

6.1 Experiment 1: Determining the minimum channel size

The part was ordered at Rapidcenter and two parts were received. Both parts were wrongly oriented on the printer's substrate. Once, the part was printed along the part's x-axis and once along the part's y-axis. One of the parts is shown in Figure 6.1 and in the photo it is indicated how the printer built up the parts. The parts were not built up as intended and this means that the machine could not as closely comply with the specified dimensions since they were not multiples of the resolution anymore. Nevertheless, it was still checked which channels were open and which were not. The outcome of the test is listed down in Table 6.1. The minimum channel size h by w is around $160\ \mu\text{m}$ by $510\ \mu\text{m}$. A SEM image of a printed $160\ \mu\text{m}$ by $510\ \mu\text{m}$ channel is shown Figure K.10. This photo shows that the channel is shaped like an ellipse rather than a rectangle. The width of the channel is very accurate in this particular cross-section ($510\ \mu\text{m}$ was stated in the design, $511.8\ \mu\text{m}$ was measured). This may be due to the fact that the channel width in this build orientation still is a multiple of the printer's resolution. The height of the channel is approximately $100\ \mu\text{m}$ larger than intended ($160\ \mu\text{m}$ versus $264.1\ \mu\text{m}$). This difference could be caused by the unfavorable printing orientation. Channels shaped like this result in a cross-sectional area which is about 25% larger than designed. It should however be kept in mind that this result was not obtained using the desired printing direction.

Table 6.1: Table showing which channels were opened and which channels were not.

Channel	1	2	3	4	5	6	7	8	9	10	11
h (μm)	50	50	50	112	112	112	160	160	160	208	208
w (μm)	68	136	204	136	272	408	170	340	510	442	646
x -direction	x	x	x	x	x	x	x	x	open	open	open
y -direction	x	x	x	x	x	x	x	open	open	open	open

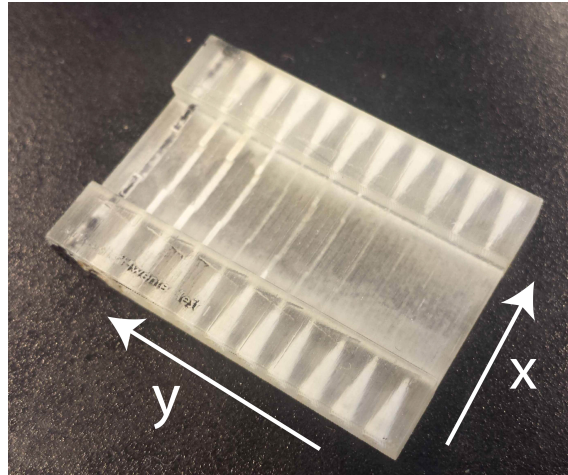


Figure 6.1: Printed version of the minimum channel dimensions test. The arrows indicate along which direction the two prints are built up. The black substance in the leftmost channel is conductive paint.

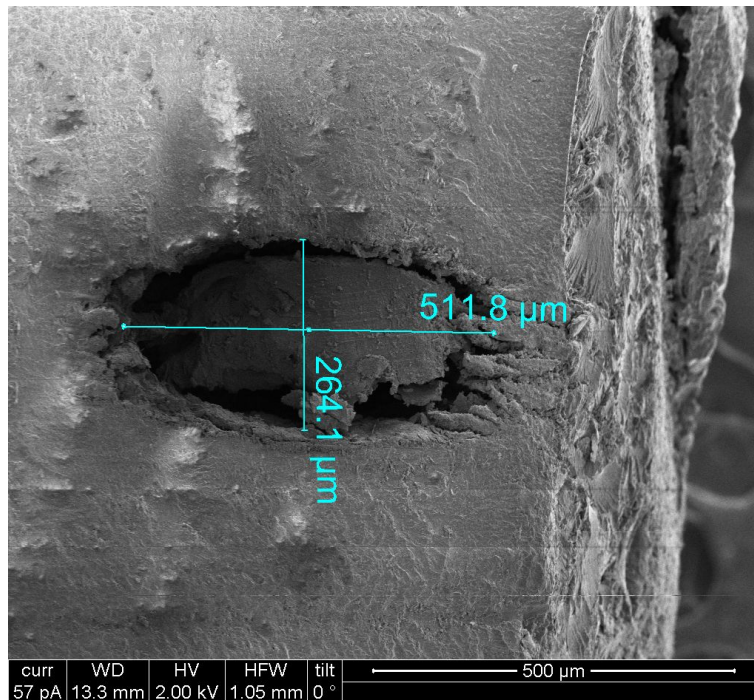


Figure 6.2: SEM photograph from a channel cross-section obtained from Figure I.2 by cutting through the channel with a knife. The channel was designed to be 160 μm (height) by 510 μm (width). It was built up with the height in the x-direction of the printer instead of the z-direction. The substance inside of the channel is graphite paint.

6.2 Experiment 2: Determining the minimum membrane thickness

The result of the fabrication is shown in Figure 6.3. After cleaning the part, the membrane is removed so that it can be viewed in the SEM. The result of performed measurements on the membrane is found in Figure 6.4. A picture is taken of each section of the membrane. It should be noted that a thickness of $50\ \mu\text{m}$ means that the membrane consists of three layer thicknesses. The printer does not have any problems with printing features in this range. The thicknesses all approximately have their specified values and any automated corrections to make models more suitable for the printer do not seem in place. However, the resulting membrane is brittle which perhaps makes it unsuitable to withstand the pressures which come with pressure driven flows.



Figure 6.3: Overview of the printed part including the membrane (left) and a microscopic close-up of the membrane (right) with the three different thicknesses: $50\ \mu\text{m}$ (left), $100\ \mu\text{m}$ (middle), and $150\ \mu\text{m}$.

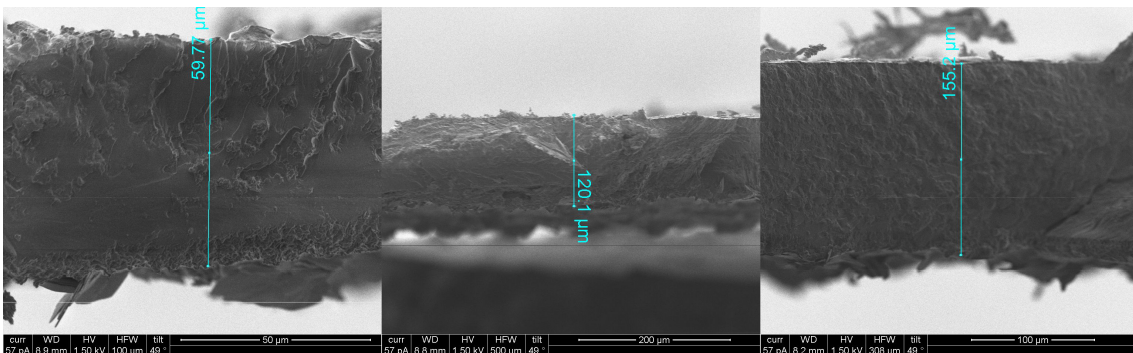


Figure 6.4: SEM-images of a membrane designed to be $50\ \mu\text{m}$ (left), $100\ \mu\text{m}$ (middle), and $150\ \mu\text{m}$.

6.3 Experiment 3: Analyzing channel and contact resistances

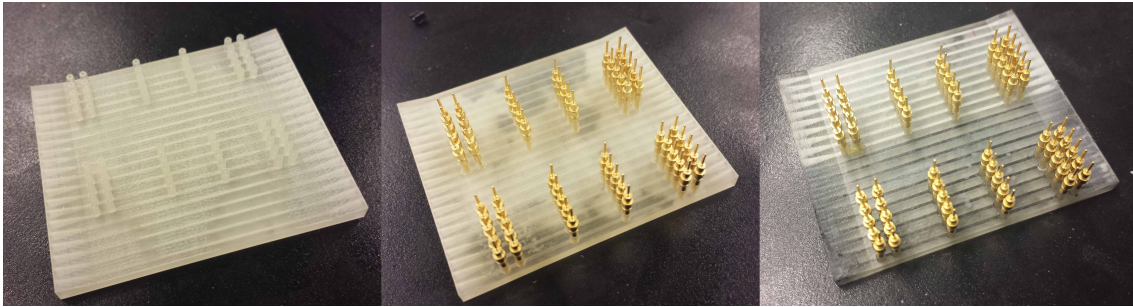


Figure 6.5: The different steps of assembly. From left to right: The chip as received from Shapeways, the chip after insertion of headers and cleaning, the chip after infusion with paint (upper ten) and glue (lower ten).

The fabrication of the chip is shown in Figure 6.5. The fabrication went mostly without any problems. Only one connector inlet partly broke off but still the connector was press fitted into place. Figure 6.6 shows typical curves obtained from the 4-wire measurements on the graphite paint and carbon glue after one week of curing (The measurement setup is shown in Figure I.3). The voltage is linearly dependent on the current and independent on the direction of the current. This means that the resistances behave linearly in the current range applied. Similar curves were obtained for 2-wire measurements, yet with a different slope (all curves are shown in Appendix J). From the current-voltage data several characteristics of the channel can be obtained. By differentiating the curves acquired by the 4-wire measurements, the resistance between that current inlet and the current outlet is determined. By doing this, the plots in Figure 6.7 are obtained, which show the course of the resistance over the length of the channel. The 0 point for every resistance is not measured but added 'as a guide to the eye' because at $d = 0$ the resistance theoretically is zero. It is shown that all the R^2 values are above 0.9703 for graphite paint with an average value of 0.9833 whereas the values for carbon glue are all above 0.9842 and have an average value of 0.9940. The infusion processes of both liquids produce resistances linearly proportional with the channel lengths.

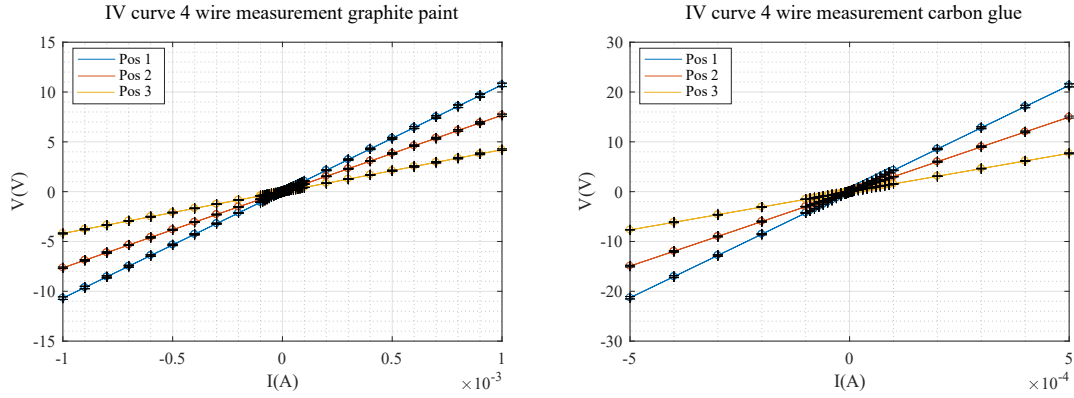


Figure 6.6: A current voltage plot for both a graphite paint (left) and carbon glue (right). The three curves are obtained at different positions in the same channel. The plot shows a average current and voltage for a current sweep back and forth which has performed ten times for each channel.

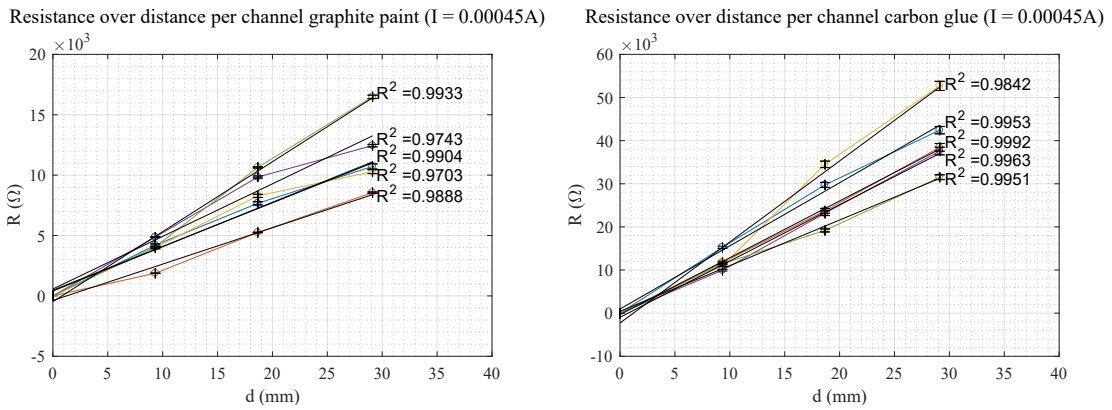


Figure 6.7: The cumulative resistance over distance, 0 mm being the point closest to the outlet. Linear fits are added to each line accompanied by their R-squared value. The left graphs shows the result for graphite paint whereas the right shows the result for carbon glue.

Comparing Figure 6.7 with Figure 6.8 shows that the graphite paint did not change much in 23 days. All resistances produced by carbon glue however have lowered several $k\Omega$. It seems that carbon glue needs at least more than a week to cure.

By subtracting the different data-points in Figure 6.7 the resistance per unit length is obtained in each section of the channel. These values are shown in Figure 6.9. It stands out that for both types of liquid, the middle section has the highest resistance per unit length. Compared to a 23 days later (Figure 6.10), graphite did not change much and carbon glue seems to have evened out. These variations in resistivity between the different sections could just be accidental, since the error bars are larger than the difference in the means between de different sections. However, it could have a reason as well. The curing in the middle section of the carbon glue can take longer, as the curing of the channel closes off the outlets and the overall cross-section through which the acetone can diffuse becomes smaller. Therefore, the middle section reaches a similar value as the side sections later. The graphite paint cured faster, and the middle section has got a higher resistance than the two side sections. A possible reason for this observation could be the outward flow patterns induced by water evaporating from the graphite particles

[65]. These flow patterns may have pushed particles to the outlets of the channel giving the regions near the outlet a higher conductivity than the middle section.

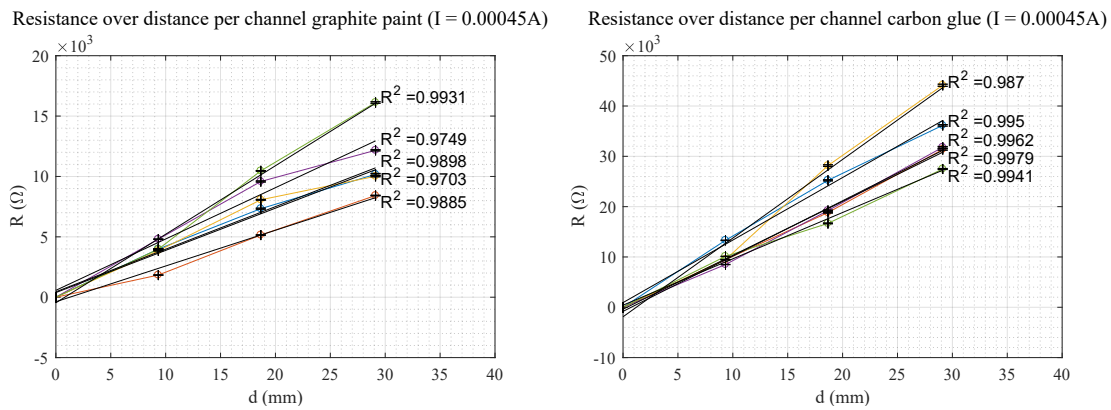


Figure 6.8: The cumulative resistance over distance, 0 mm being the point closest to the outlet. Linear fits are added to each line accompanied by their R-squared value. The left graphs shows the result for graphite paint where as the right shows the result for carbon glue. These data are acquired 23 days after the initial measurement.

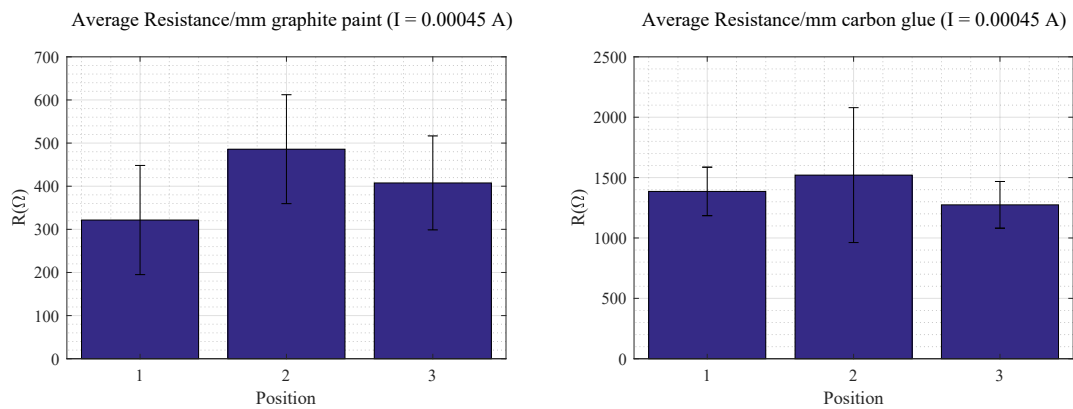


Figure 6.9: The average resistance per millimeter in rectangle channels of $160 \mu\text{m}$ by $510 \mu\text{m}$ for graphite paint (left) and carbon glue (right).

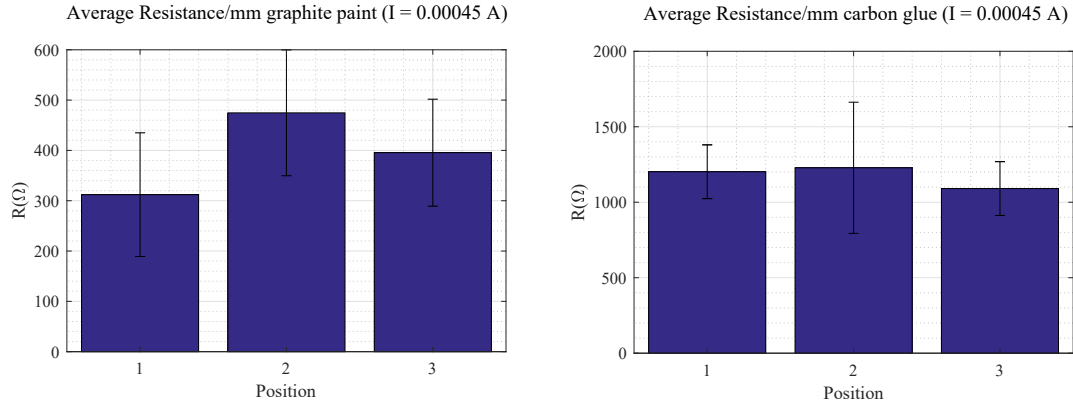


Figure 6.10: The average resistance per millimeter in rectangle channels of $160\ \mu\text{m}$ by $510\ \mu\text{m}$ for graphite paint (left) and carbon glue (right). These data are acquired 23 days after the initial measurement.

The graphite paint has an average resistivity of $394\ \Omega\text{mm}^{-1}$ with a standard deviation of $68\ \Omega\text{mm}^{-1}$ in channels of $160\ \mu\text{m}$ by $510\ \mu\text{m}$. Compared with the calculations previously done, which predicted $0.1\text{--}1\ \text{k}\Omega\text{mm}^{-1}$, this is in the expected range. The resistance of the carbon glue however, which is $1174\ \Omega\text{mm}^{-1}$ with a standard deviation of $167\ \Omega\text{mm}^{-1}$, is far off from the predicted resistance of $100\ \Omega\text{mm}^{-1}$. It is not sure why this is the case. The particles in the carbon glue are relatively large ($5\text{--}10\ \mu\text{m}$) compared to the channel height and width ($160\ \mu\text{m}$ by $510\ \mu\text{m}$). A defect (two particles not connected or particles missing) thus has a larger influence on the overall resistance of the channel than a defect in the graphite paint, which has a mean particle size of $1\ \mu\text{m}$.

By subtracting the resistance values obtained with the 4-wire measurements from the values obtained with the 2-wire measurements, the contact resistances can be acquired. These values are depicted in Figure 6.11 and in Figure 6.12. Every value contains two contact resistances: The one at the current inlet and the one at the current outlet. One could thus divide these values by two to obtain an approximation of the contact resistance per electrode. Doing so, a contact resistance per contact of $75\ \Omega$ with a standard deviation of $26\ \Omega$ for graphite paint is obtained and $187\ \Omega$ with a standard deviation of $152\ \Omega$ for carbon glue. The contact surface between the suspensions and the gold connector is approximately $0.46\ \text{mm}^2$.

Aside from a lower resistance and contact resistances due to curing, both the suspensions seem to produce stable contacts and resistances over time. The final resistance over $29.11\ \text{mm}$ is $11.4\ \text{k}\Omega$ with a standard deviation of $2.97\ \text{k}\Omega$ for graphite paint and $34.2\ \text{k}\Omega$ with a standard deviation of $6.35\ \text{k}\Omega$ for carbon glue. This means that graphite paint produces a lower resistance but carbon glue produces resistances with relatively higher consistency.

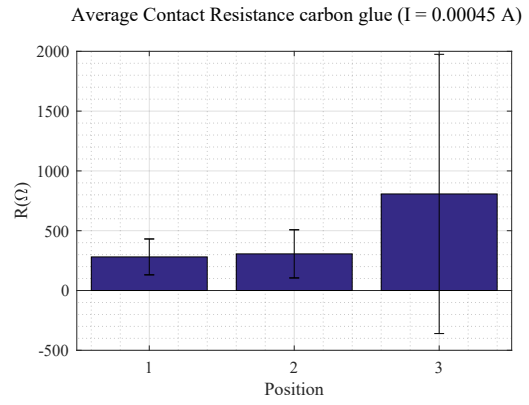
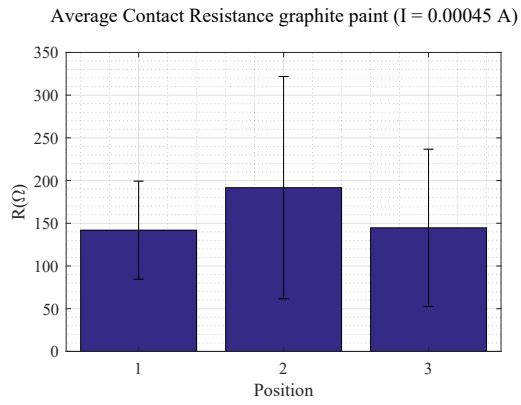


Figure 6.11: The average contact resistance of the current inlet and current outlet for graphite paint (left) and carbon glue (right).

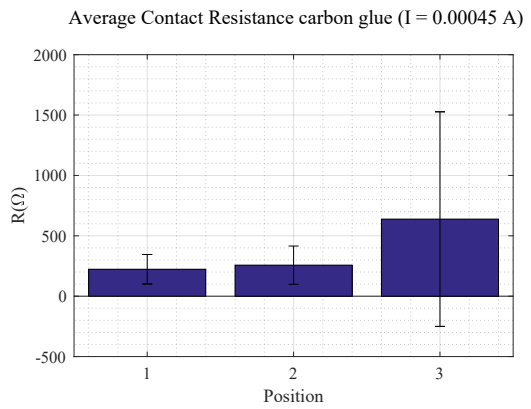
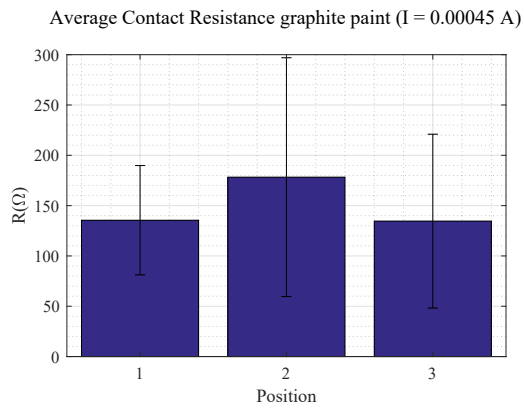


Figure 6.12: The average contact resistance of the current inlet and current outlet for graphite paint (left) and carbon glue (right). These data are acquired 23 days after the initial measurement.

6.4 Experiment 4: Using the channels as strain gauges

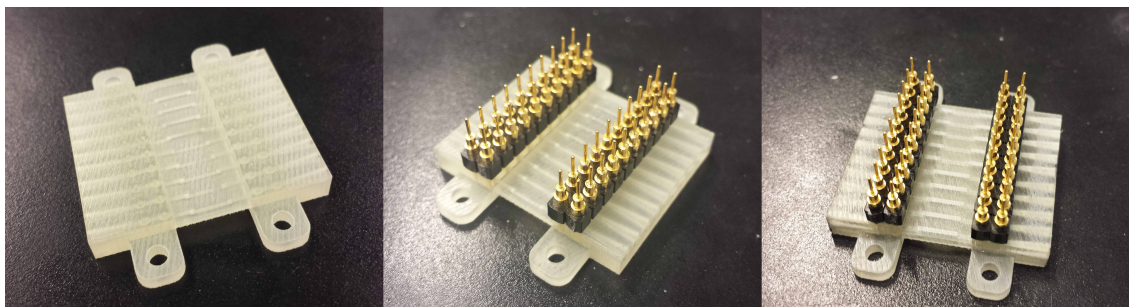


Figure 6.13: Assembly of a strain gauge sensor with straight channels. From left to right: The chip as received from Shapeways, the chip after insertion of headers and cleaning, the chip after infusion with paint.

The process of assembling a strain gauge is illustrated in Figure 6.13. This is the first sensor which fitted the standard connectors without any adaptations. The fabrication led to the resistances as noted down in Table 6.5. It is noteworthy that these values are all high compared to the resistivities obtained in Experiment 3. The carbon glue resistors additionally have a large spread in values. Carbon glue resistivities were found as low as $1.65 \text{ k}\Omega\text{mm}^{-1}$ but also as high as $53 \text{ k}\Omega\text{mm}^{-1}$. The latter is about 45 times as high as the resistivities obtained for carbon glue in the experiment with straight channels. Two phenomena could underlie these observations: When the suspensions dry, the perpendicular parts in the channel possibly create stress in the corners which leads to a higher resistance. Again this effect might be larger for the carbon glue since the conducting particles in this glue are larger. A second, simpler, explanation is a deviation in the accuracy of the printer between prints. To find out about the cause of this deviation, more research is needed.

Table 6.2: Average resistances of the strain gauges after fabrication.

Graphite paint		
Sensor	Mean	Range (min-max)
860 μm membrane	$0.849 \text{ k}\Omega\text{mm}^{-1}$	$0.696\text{--}0.965 \text{ k}\Omega\text{mm}^{-1}$
1260 μm membrane	$0.873 \text{ k}\Omega\text{mm}^{-1}$	$0.596\text{--}1.11 \text{ k}\Omega\text{mm}^{-1}$
Carbon glue		
Sensor	Mean	Range (min-max)
860 μm membrane	$7.29 \text{ k}\Omega\text{mm}^{-1}$	$1.93\text{--}20.2 \text{ k}\Omega\text{mm}^{-1}$
1260 μm membrane	$16.2 \text{ k}\Omega\text{mm}^{-1}$	$1.65\text{--}53.0 \text{ k}\Omega\text{mm}^{-1}$

In Figure 6.14, the deflection of the 860 μm thick doubly clamped beam filled with graphite paint is shown as a function of time and as a function of force (a photo of the setup is shown in Figure I.4). Over time, the curve clearly shows creep. The minimums and maximums are increased as the number of cycles increases. Also, a hysteresis loop is clearly visible in the deflection versus force graphs as the loading curve does not follow the unloading curve.

The graphs show a positive offset as well as a first load unload loop which deviates from the other loops. This is an artefact of the measurement setup. The plunger is made to evenly spread the force over the beam and can therefore move around its axis (Figure I.4). This mechanism also gives the plunger some leeway to rotate in the unwanted direction. After the plunger is set in position and the measurement is started, the plunger moves to the most energetically favorable position. This results in a first loop that creates an offset and also looks differently than the rest of the loops.

Initially, the linear model as presented in Appendix E underestimated the deflection. The model relies on an accurate value for the Youngs modulus, which in the material datasheet was mentioned to be 1.463 GPa. A possible explanation of this underestimation is that Youngs modulus in reality is lower than the value used in the model. Further literature research lead to the conclusion that for tensile strains the VisiJet material has a Youngs modulus of 620–760 MPa [66]. Utilizing a Youngs modulus of 700 MPa (for flat printed structures), the dashed red line in Figure 6.14 is obtained. Another adaptation of the linear model in which it is tried to incorporate the mechanical effects of the channels in the spring constant is worked out in Appendix F. The result is the dashed green line in Figure 6.14. Especially in the right graph the deflections predicted by the linear models are close to the results of the measurement. At the end of the measurement, the red line deviates a maximum of 12 μm whereas the green line deviates a maximum of approximately 10 μm in the returning loop. In the left graph, the red and the green line deviate a maximum of approximately 16 μm and 14 μm in the returning loop, respectively. There is however a sort of cusp, around 4 N in the left graph, whereas also the right graph shows a clear deviation from a straight line, which self-evidently cannot be explained by a linear model.

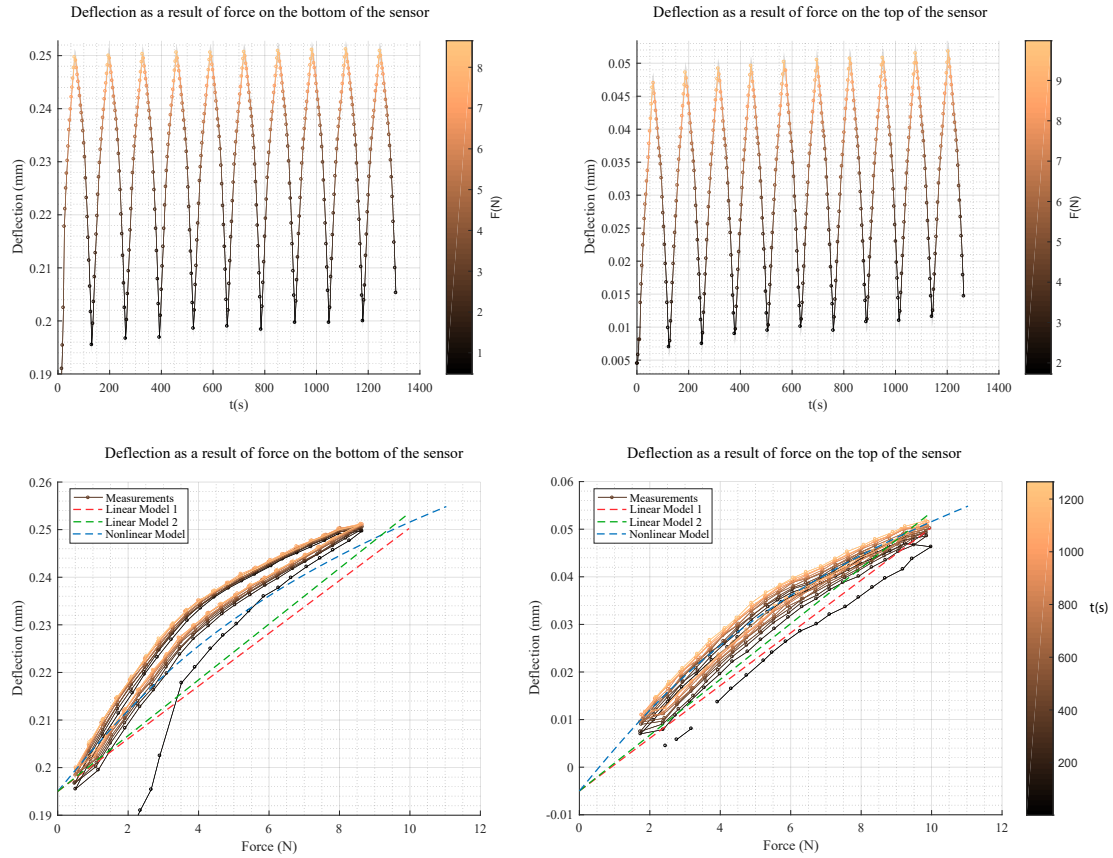


Figure 6.14: The deflection generated by a load on the middle of the membrane from the bottom (left) and from the top (right). The dashed lines indicate the outcomes of three different modeling approaches.

The linear models make several assumptions as to why the resulting deflections would be linearly related to the force. The clamps of the beam are in reality not infinitely stiff as is assumed in the theoretical model; they are made from the very same polymer as the beam itself. This can give an extra degree of freedom making the spring constant different than anticipated. Further, the linear models do not take into account beam stiffening. This is an effect in which the spring constant increases as deflection increases due to stretching of the beam. A third model, which takes nonlinear bending-effects into account, is investigated, see Appendix G. This model takes into account both the bending strain and axial strain. Working out the deflection utilizing this method leads to a polynomial expression with two constants (C_b and C_s) to be determined. This is done by fitting the function to the measurement data of the right graph. Self-evidently, the resulting model fits well with the measurements plotted on the right. The nonlinear model resembles the measurements plotted on the left more closely than the linear ones. However, the deflection is still underestimated with a maximum of about $8\ \mu\text{m}$. Also the cusp is not explained by the nonlinear model. The cusp much resembles the nonlinear stress strain relation of the printing material. Normally this nonlinear effects are only present at higher magnitudes of strain but the time scale of the applied loads - a load unload cycle takes about two minutes in this experiment - increases the nonlinear effect in the stress-strain relation [66]. However, this does not explain the differences between applying loads from the top or from the bottom.

Figure 6.15 shows the electrical response of the sensor with $860\ \mu\text{m}$ beam incorporating

straight channels filled with graphite paint to repetitive loading and unloading. During each measurement, five channels experience a tensile strain and five a compressive strain. Since the five measurements for a particular channel orientation are done within half a second, the response is averaged and possible creep in that time frame is neglected. The standard deviation of the averaging is shown in the shaded area. The sensor output is normalized with respect to the first measurement. It is shown in the four graphs that the output of the sensor drifts upward during the first cycle load unload cycle. Initially, the sensor values return to a value larger than $\frac{\Delta R}{R} = 0$ when the load reaches its minimum. Though, after the initial load unload cycle, the output seems to drift downwards. Both observations are opposite to the mechanical response of the beam, which shows residual strains at the load minimum. Residual bend strains would result in an upward drift of the output signal for the elongated channels whereas compressed channels should show a downward drift. A residual axial strain would lead to a gradual upward drift for both elongated and compressed channels. This behavior thus is prescribed to the conductor inside the channels. It remains unclear what is the exact reason for this effect.

If the average sensor response is plotted with the force on the x-axis, Figure 6.16 is obtained. The drift in the resistance values is clearly shown. All resistors change value during the first cycle and during the following cycles drift downward again. A total drift of up to approximately 1.5% is shown in the bottom left graph. By taking the derivative of the plotted lines, and averaging the obtained values, something can be said about the sensitivity of the resistive channels. The obtained values are listed down in Table 6.3. Especially in the latter five channels, the standard deviation is rather large compared to the mean. The strain gauges do not show a consistent increase or decrease in sensitivity when switching from compressive strain to tensile strain.

Table 6.3: Responsivity of the straight channels in a 860 μm beam filled with graphite paint.

Responsivity (N^{-1})				
Channel number	1-5		6-10	
Strain	mean	σ	mean	σ
Tensile	0.003	0.001	0.002	0.001
Compressive	-0.004	0.002	-0.001	0.001

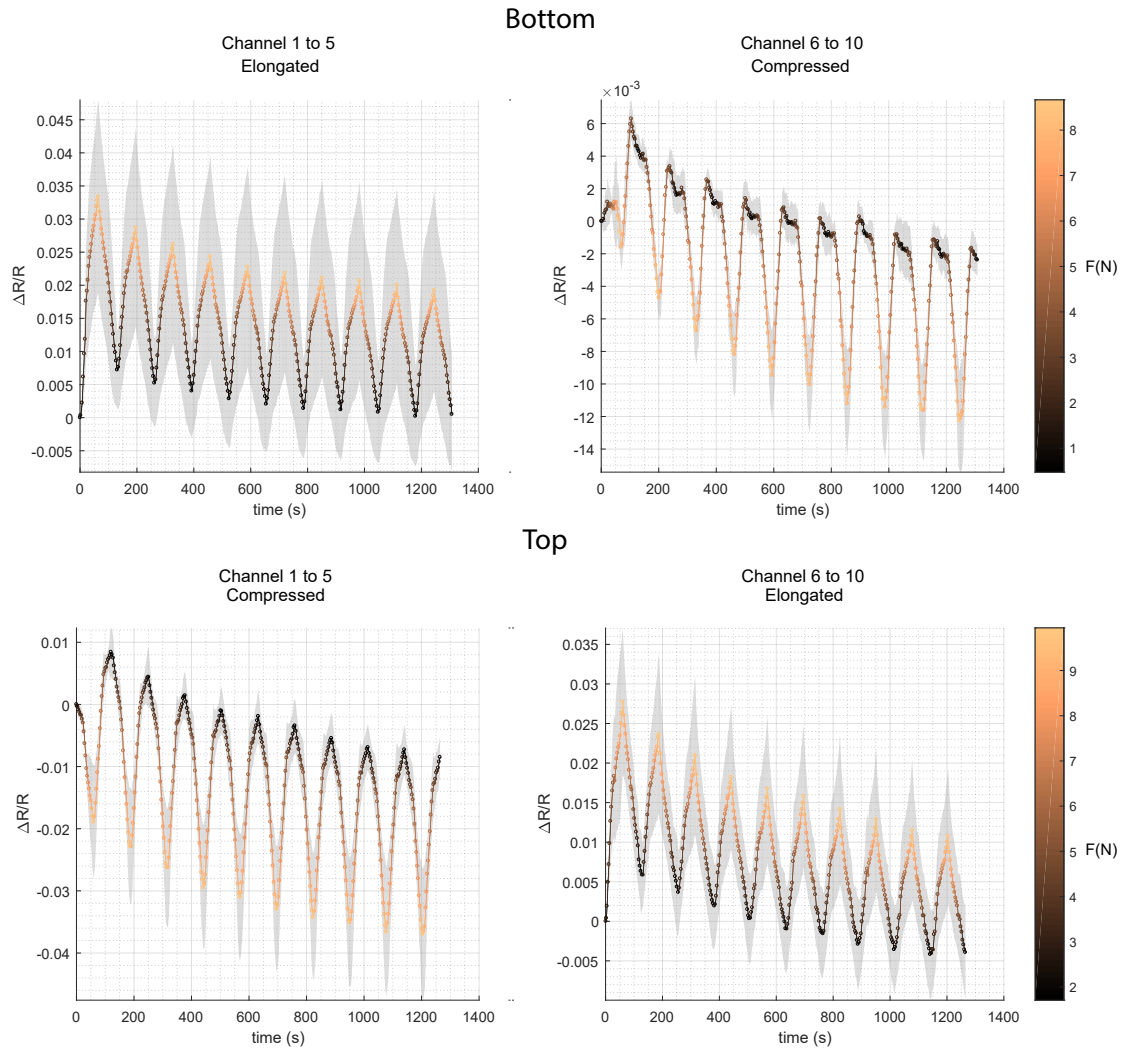


Figure 6.15: The measurements showing the load-unload cycles over time for the 860 μm beam incorporating straight channels infused with graphite paint. Loads are applied from the bottom and the top, color indicating the magnitude of the force. In each measurement, five channels are elongated and five compressed due to their orientation in the beam. The graphs show the average response and the shaded area is the standard deviation.

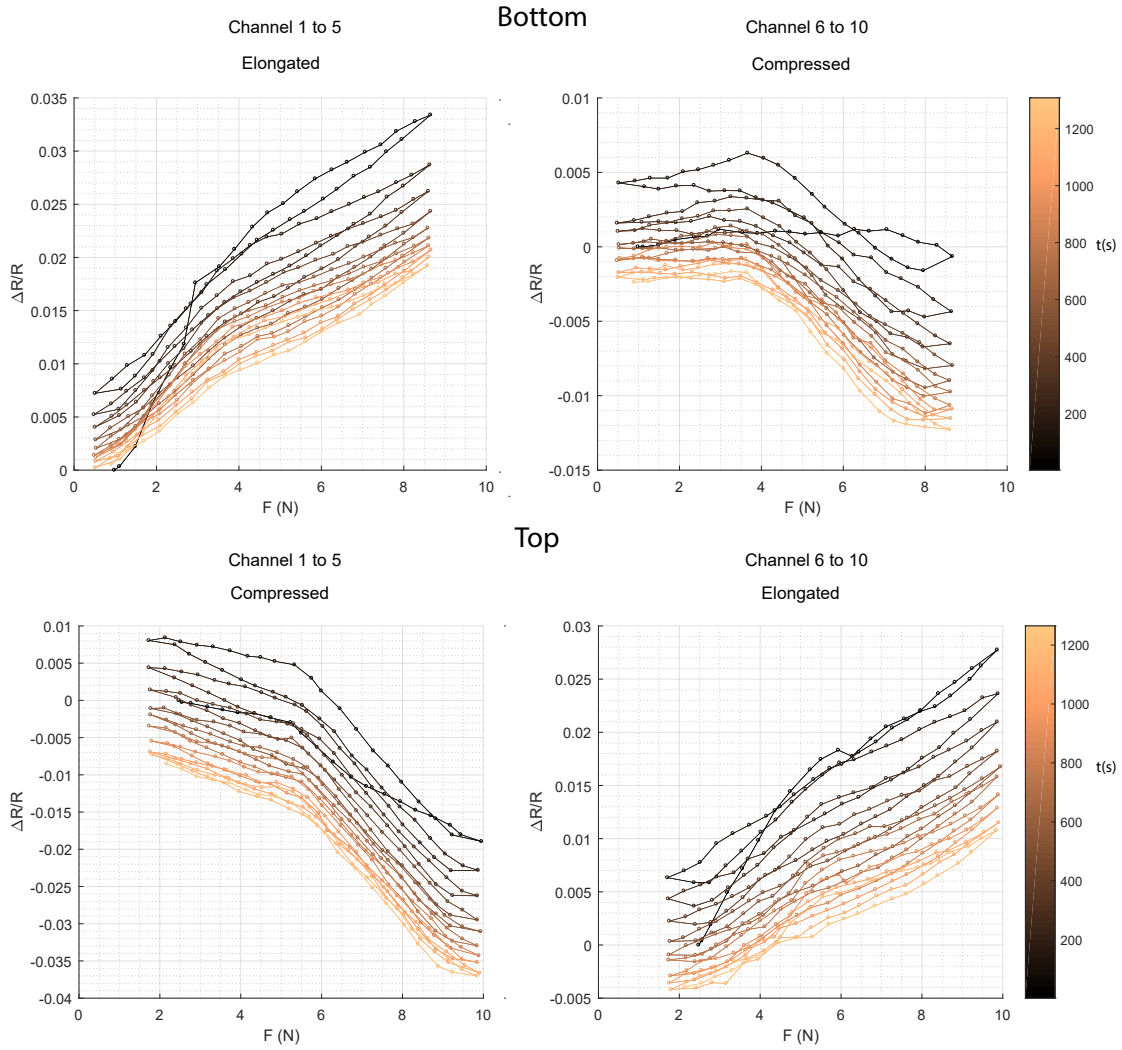


Figure 6.16: The data from Figure 6.15 presented in a different manner; the relative resistance change plotted as a function of the force. The response over time is indicated by the colorbar.

Figure 6.17 shows the response of the sensor with 860 μm beam incorporating straight channels filled with carbon glue to repetitive loading and unloading. The responses of channel 6 to 10 while loading from the bottom of the sensor are characterized by a small average signal and a large standard deviation. Some resistances show large shifts in resistance during the measurement which offset the output signal. Individual particles disconnect during loading and unloading and cause the resistance to shift upward. This was not so much the case with channel 1 to 5, which were elongated. Also, the overall response of first five channels is more consistent, and less noisy than the response of channel 6 to 10. This may be due to the fact that the average resistance of the first five channels is lower than the latter five. A possible reason for the variation in resistance could be a non uniform distribution of conducting particles in the syringe and hence a difference in resistance due to the order in which they were filled. The exact reason is however unclear.

This difference in response is also shown in Figure 6.18. Again, the average sensitivity can be calculated by taking the derivative of the resistance change to the force. The obtained values are listed down in Table 6.4.

Table 6.4: Responsivity of the straight channels in a 860 μm beam filled with carbon.

Responsivity (N^{-1})				
Channel number	1-5		6-10	
Strain	mean	σ	mean	σ
Tensile	0.003	0.004	0.002	0.007
Compressive	-0.0008	0.004	-0.0004	0.005

Both sets of channels show a higher sensitivity when elongated than when compressed. A possible explanation for this difference is the axial strain, which adds in sensitivity in the elongated channels and opposes the sensitivity in the compressed channels. However, calculations show that the axial strain is an order of magnitude smaller than the bend strain in the range of loads applied (Appendix G). Also, this effect was not observed in the channels filled with graphite paint.

For both the elongated and compressed parts it remains unknown what role the perpendicular sections of the channel play in the sensor output. Of course, according to theory these sections should remain neutral, but in practice this does not have to be the case. Especially if the majority of the resistance is located here, there is a possibility that the perpendicular sections play a significant role.

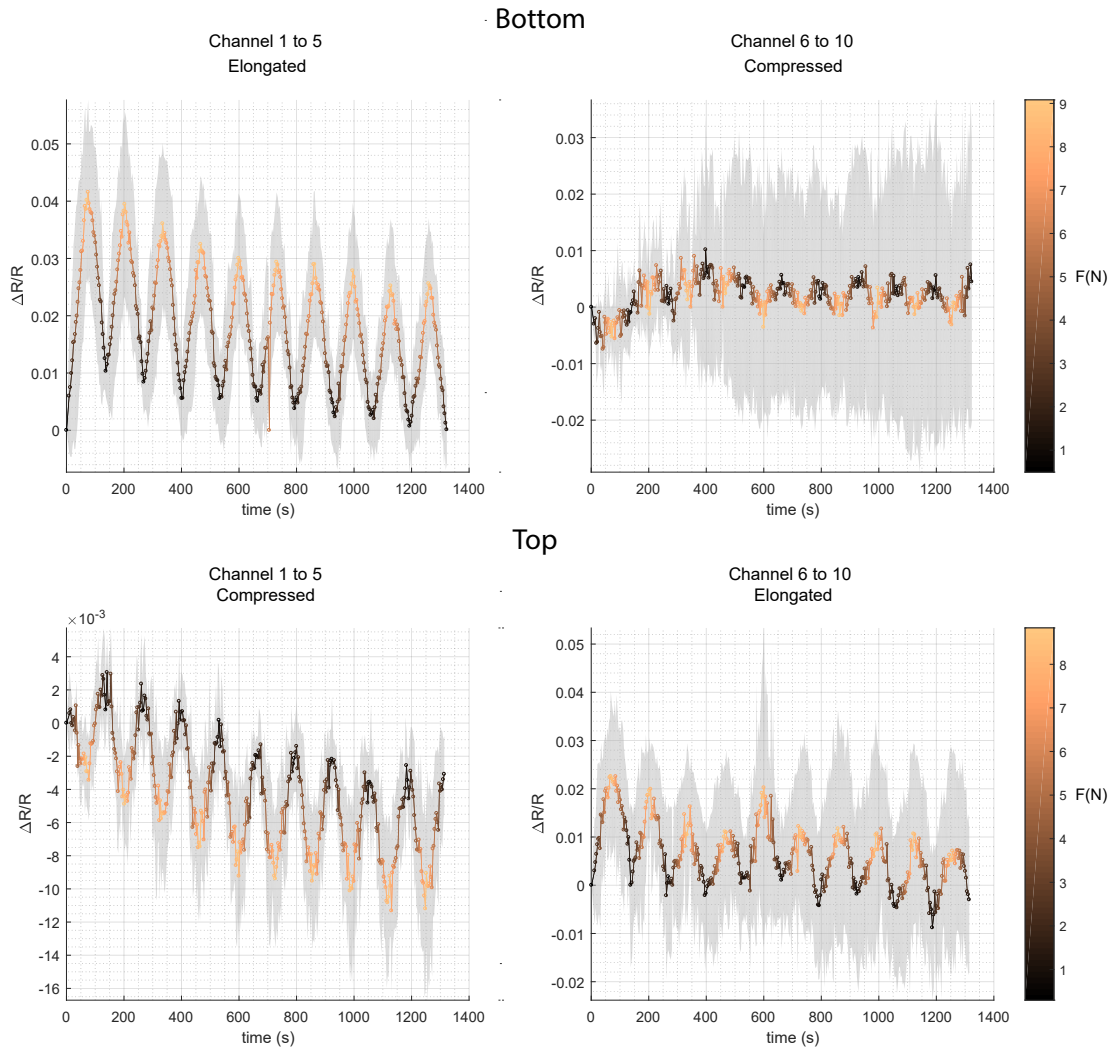


Figure 6.17: The measurements showing the load-unload cycles over time for the 860 μm beam incorporating straight channels infused with carbon glue. Loads are applied from the bottom and the top, color indicating the magnitude of the force. In each measurement, five channels are elongated and five channels are compressed due to their orientation in the beam. The graphs show the average response and the shaded area is the standard deviation.

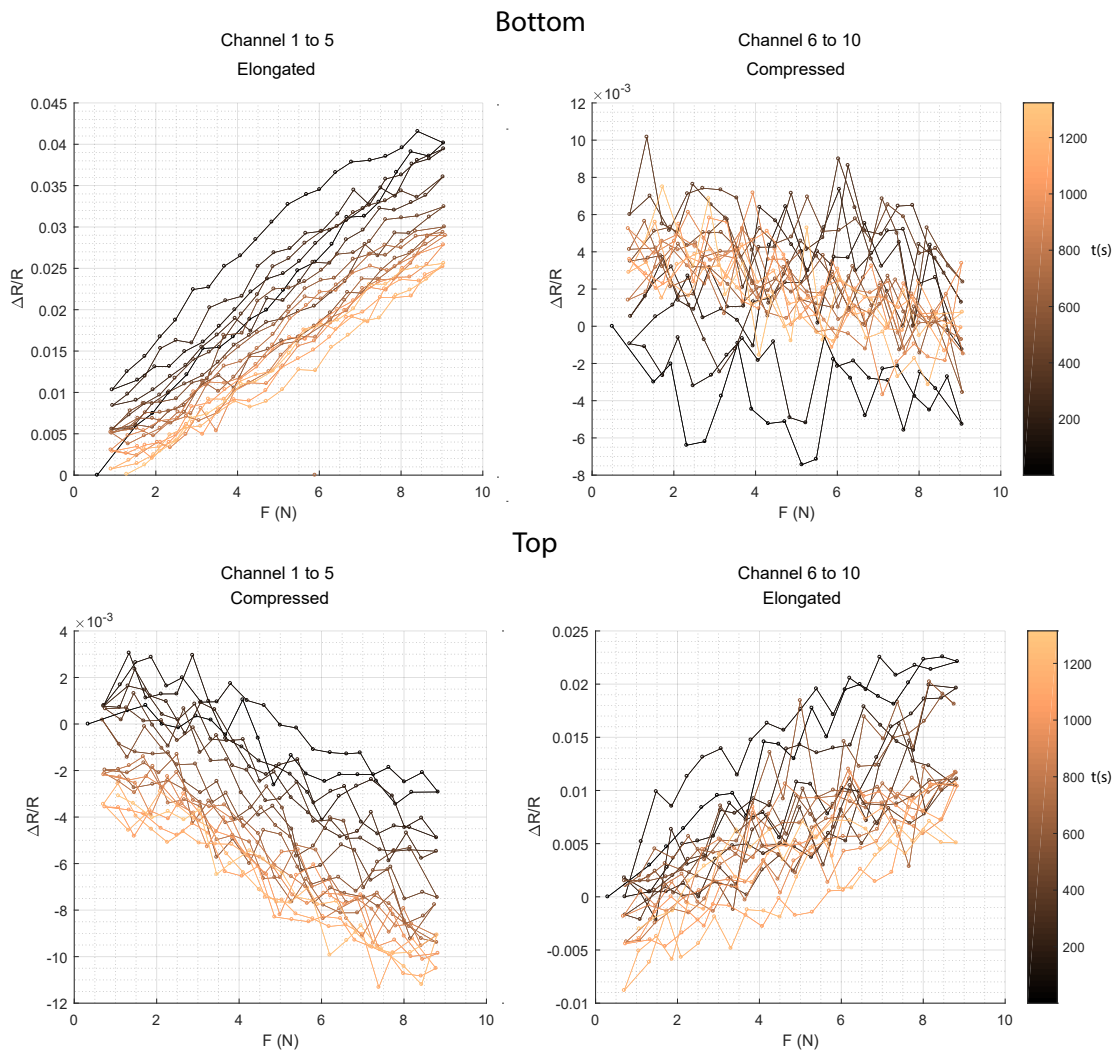


Figure 6.18: The data from Figure 6.17 presented in a different manner; the relative resistance change plotted as a function of the force. The response over time is indicated by the colorbar.

6.5 Experiment 5: Changing from straight to tapered channels

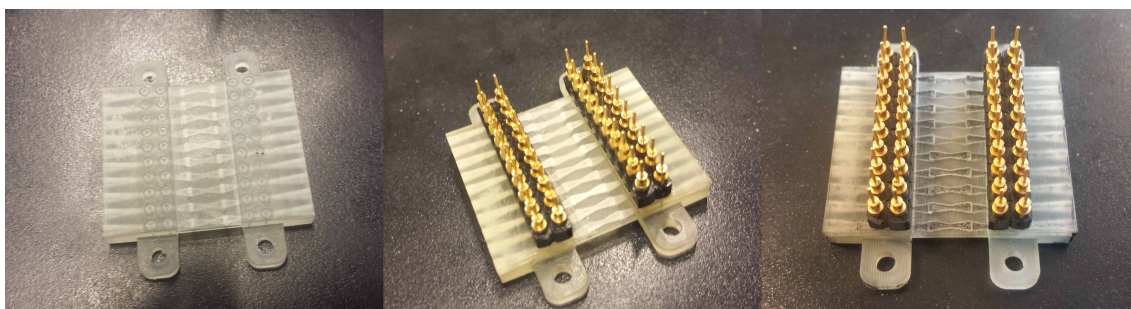


Figure 6.19: Assembly of a strain gauge sensor with tapered channels. From left to right: The chip as received from Shapeways, the chip after insertion of headers and cleaning, the chip after infusion with paint.

Table 6.5: Average resistances of the strain gauge with tapered channels after fabrication.

Graphite paint		
Sensor	Mean	Range (min-max)
860 μm membrane	$3.64 \text{ k}\Omega\text{mm}^{-1}$	$0.927\text{--}16.5 \text{ k}\Omega\text{mm}^{-1}$

The assembly of the chip is illustrated in Figure 6.19. The channels of this structure were more difficult to clean than previous structures. During the process of filling, two channels got blocked. The fabrication resulted in an average resistivity of $3.64 \text{ k}\Omega\text{mm}^{-1}$. The highest resistance being approximately $16.5 \text{ k}\Omega\text{mm}^{-1}$ and the lowest approximately $0.927 \text{ k}\Omega\text{mm}^{-1}$. This is remarkable, since the designed channel on average has larger cross-sectional area than the previously designed strain gauges, which should evidently lead to a lower resistance. These observations lead to the suspicion that the printing process might show deviations in accuracy over time or on different printers. Inconsistencies in the filling process are however not ruled out since the suspicion cannot be checked on.

Figure 6.20 shows the response of the sensor with 860 μm beam incorporating tapered channels filled with graphite paint to repetitively loading and unloading. The graphs show a large range of sensitivities over the different channels, especially when being elongated. It is unclear as to where these large variations in sensitivity come from as there is no clear relation between the resistance of a channel and the sensitivity. Also, the lower left graph shows large drift in the unloaded resistance. The grey area extends up to 5% of the initial resistance.

Figure 6.21 shows the response of the sensor plotted versus the force. From these graphs, the responsivity of the various channels have been derived. The responsivities are listed down in Table 6.6. The averages are higher than the previously tested sensors. Also, the sensitivity of the elongated channels are closer to the sensitivity of the compressed channels in this configuration. However, the spread in sensitivity and also the spread in resistance values is higher for the tapered channels compared to the straight channels.

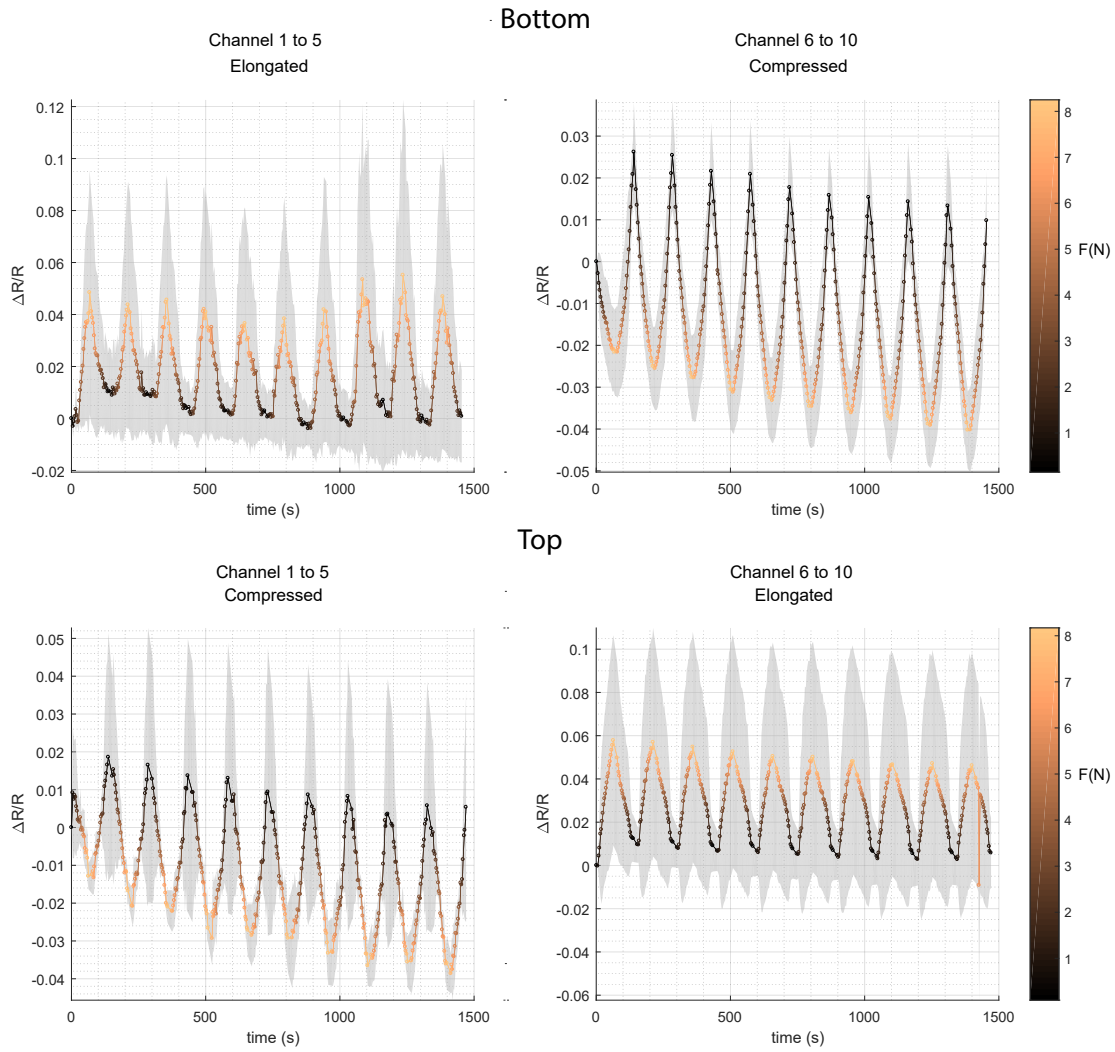


Figure 6.20: The measurements showing the load-unload cycles over time for the 860 μm beam incorporating tapered channels infused with graphite paint. Loads are applied from the bottom and the top, color indicating the magnitude of the force. In each measurement, five channels are elongated and five channels are compressed due to their orientation in the beam. The graphs show the average response and the shaded area is the standard deviation.

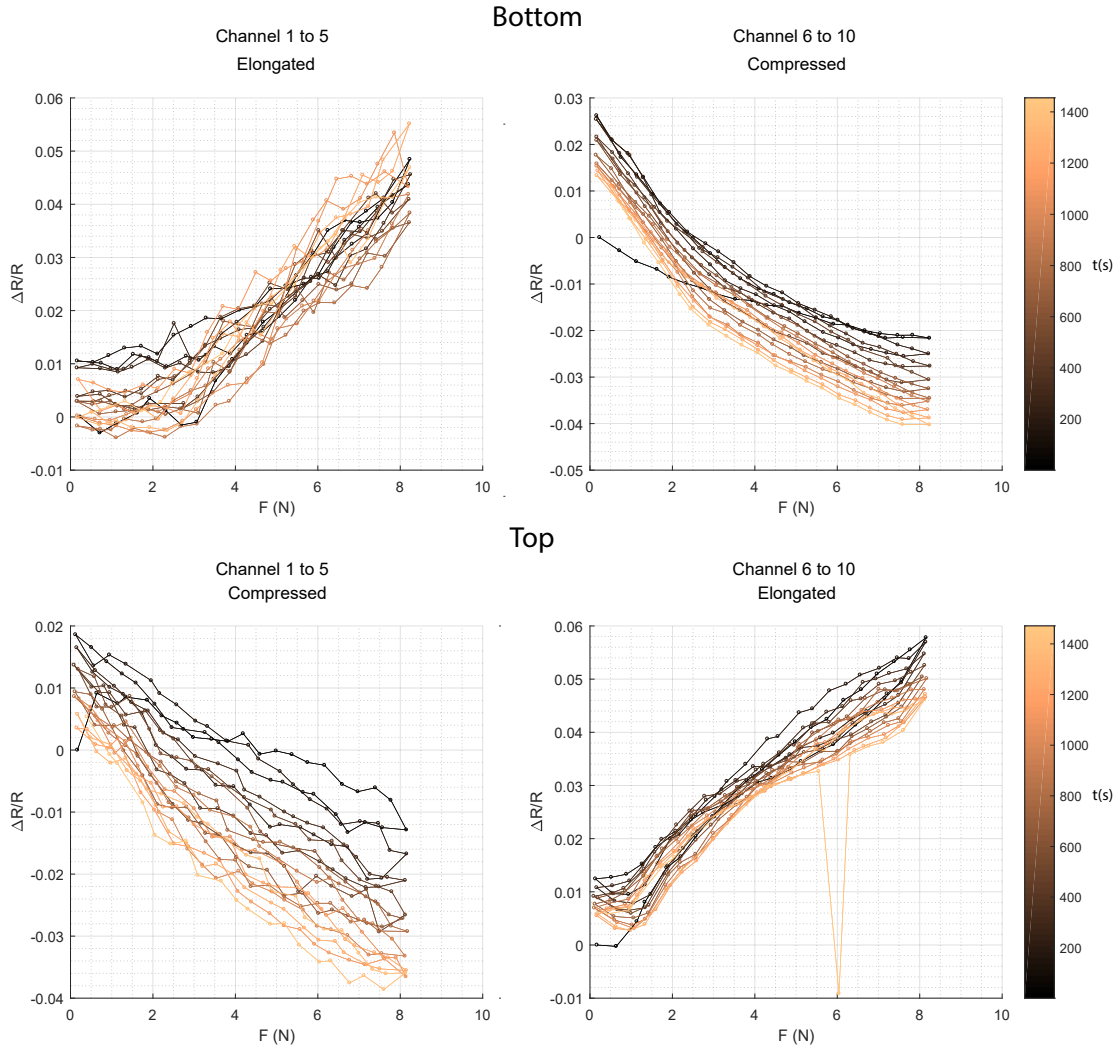


Figure 6.21: The data from Figure 6.20 presented in a different manner; the relative resistance change plotted as a function of the force. The response over time is indicated by the colorbar.

Table 6.6: Responsivity of the tapered channels in a 860 μm beam filled with carbon.

Responsivity (N^{-1})				
Channel number	1-5		6-10	
Strain	mean	σ	mean	σ
Tensile	0.006	0.01	0.005	0.01
Compressive	-0.005	0.005	-0.006	0.008

6.6 Experiment 6: Designing a circular 3DOF sensor

The sensor as designed is printed and shown in Figure 6.22. The printed circuit board is shown in Figure 6.23. Due to time constraints these have not been further assembled yet.



Figure 6.22: The sensor as received from Shapeways.

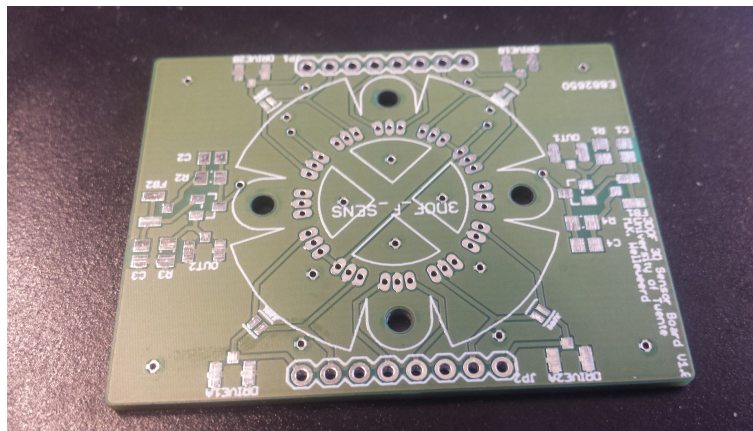


Figure 6.23: The printed circuit board as received from Eurocircuits.

6.7 Conclusion

A series of experiments has been carried out to characterize the various aspects of producing a sensor: the printing technique itself, the resistances produced by the infusion process of both types of liquid (graphite paint and carbon glue), the behavior of strain gauges in doubly clamped beams and finally the sensor itself.

The printing technique was characterized and it was found that the Projet 3500HD-Max produces channels with minimum channel dimensions of $160\ \mu\text{m}$ (height) by $510\ \mu\text{m}$ (width). It seems that the channels are shaped like an ellipse rather than a rectangle. It should however be kept in mind that these results were achieved printing the parts in the non-preferred print orientations. The minimum membrane thickness is determined to be $50\ \mu\text{m}$.

Next, an experiment was performed to determine the quality of resistances formed by both the graphite paint and carbon glue in channels of $160\ \mu\text{m}$ by $510\ \mu\text{m}$. Also the contact resistance formed with the gold connectors was evaluated. The built resistors all behave linearly over the range of currents applied. Graphite paint is found to have an average resistivity of $394\ \Omega\text{mm}^{-1}$ and carbon glue a resistivity of $1174\ \Omega\text{mm}^{-1}$. Both suspensions produced a linear resistance over the channel. Graphite paint produces less linear resistances with an average R^2 value of 0.9833 whereas the average R^2 value for carbon glue is determined to be 0.9940. Also, carbon glue has a higher consistency in resulting resistances when filling multiple channels. Graphite paint has a lower resulting

resistance. Both suspensions are stable over time though the carbon glue needs over a week to stabilize. For graphite paint, the average contact resistance with the gold plated connectors is found to be $75\ \Omega$ on average whereas the resulting contact resistance of carbon glue is $187\ \Omega$. Both contact resistances were obtained with a contact surface between the glue and the gold pin of approximately $0.46\ \text{mm}^2$. A summary of the characteristics of both paints is listed down in Table 6.7. Doubly clamped beams are designed

Table 6.7: Average resistances of the strain gauge with tapered channels after fabrication.

Property	Graphite paint		Carbon glue	
	mean	σ	mean	σ
Resistivity ($\text{k}\Omega\text{mm}^{-1}$)	0.394	0.068	1.174	0.167
Contact resistance (Ω)	75	26	187	152
Linearly proportional (R^2)	0.9833		0.9940	
Curing time	Less than a week		Over a week	

incorporating ten channels to verify the validity of the design principles stated in the development of a circular 3DOF sensor. The resistivities resulting from the fabrication are listed down in Table 6.9. These resistivities are high compared to the resistivities found in the experiments with straight channels. Especially for the carbon glue the difference between the minimum and maximum obtained resistance is high. Thus, this time the graphite paint had a higher repeatability than the carbon glue. More research is needed as to why the resistances are this high in the fabricated chips. Both print inaccuracy and induced stress can underlie this observation. The $860\ \mu\text{m}$ thick strain gauges were tested as a force sensor by repetitively loading and unloading them. It was found that including beam stiffening in the deflection model gives a better prediction of the deflection. In each sensor, two sets of five channels which were each others mirror-images in the neutral plane were compared with each other. The average responsivities are listed down in Table 6.9.

Table 6.8: Average resistances of the strain gauge with tapered channels after fabrication.

Graphite paint		Carbon glue	
Resistivity ($\text{k}\Omega\text{mm}^{-1}$)			
Mean	Range (min-max)	Mean	Range (min-max)
0.861	0.596-1.11	11.8	1.65-53.0
Responsivity (N^{-1})			
Mean	σ	Mean	σ
0.002	0.0008	0.002	0.002

A doubly clamped channel incorporating tapered channels was subsequently fabricated to evaluate which consequences the channel shape has on the sensitivity of the sensor. The channels were filled with graphite paint and resistivities as listed down in ?? were acquired. It is not sure as to why the infusion of these channels resulted in higher resistances than previously infused channels while the channel cross-section is larger. The sensor showed the responsivities as listed down in ??.

All the strain gauges respond in a similar way as modeled; that is, when the gauges are elongated, the relative resistance change goes up, and when they are compressed, the relative resistance change goes down. Also, the tapered channels show a higher sensitivity

Table 6.9: Average resistances of the strain gauge with tapered channels after fabrication.

Graphite paint	
Resistivity ($\text{k}\Omega\text{mm}^{-1}$)	
Mean	Range (min-max)
3.64	0.927-16.5
Responsivity (N^{-1})	
Mean	σ
0.005	0.005

than the straight ones. But there is a difference between the mechanical response and the strain gauge response which indicates that there are higher order effects which mainly take place in the resistor itself. There is little consistency in several aspects of the strain gauges at the moment. The absolute values of the resistive channels vary between the various channels although they were produced at the same time. Especially for carbon glue resistors and the graphite paint in the tapered channels this is the case. The sensitivity of the gauges shows large variations, mainly in the tapered channels. Also, variations exist between elongation and compression. The sensors additionally show drift during the measurement.

Finally, the proposed sensor was successfully designed and printed. Also, a PCB for the readout was designed and fabricated. However, due to time restrictions these have not been assembled and tested yet.

Chapter 7

Conclusion

A fabrication and design approach is presented which enables single material printers to be utilized for the fabrication of sensors. In a single material print channels and voids are incorporated which later are infused with a conducting liquid. Using this technique, several chips/sensors were successfully fabricated. Setups has been made to characterize the fabricated chips.

The fabrication of the 3D printed structures was successful. The ProJet 3500HDMax turned out to be a printer with the right characteristics. 3D printing proved to be very useful in this project. The printing technique allows a lot of design freedom and also rapid prototyping. Projects using micro machining normally only have one chance to fabricate a series of chips. In this project, eight different structures were built. Each newly produced chip had improvements with respect to its predecessor. Not only is designing and producing a new part fast, it is also cheap: The printed parts cost about twenty euro per piece.

The technique of infusion produced resistances which were linearly proportional over distance in straight channels. However, between various resistors produced at the same time, differences were found in the absolute value of the resistance. The later produced strain gauges had a higher average resistance compared to the straight channels and showed even more variations in resistance across the different channels. It is unsure yet what exactly is the cause of these variations. During this research it was tried to keep the channel dimensions as small as possible. A result of this is that fluctuations in the printing quality have a large influence on the resulting resistances. By scaling up the dimensions in the future, the variation in the resulting resistances and sensitivity may be lower. Another aspect that deserves more careful investigation is the integration of bends in the channel. A straight channel may have to be incorporated next to the bent ones to compare channels built in the same process. Another approach would be to compare bends with different radii of curvature and the resulting resistance.

Further, the liquids utilized in this research have a relatively large resistivity. As a result, the electrical connections have to be placed close to the measurement elements not to diminish the sensor readings. This is a major drawback of the proposed fabrication approach. Ways have to be found to cleverly connect the resistive carbon tracks to tracks with a higher conductivity. An example of this is to infuse the graphite paint tracks, which leave a lot of voids, partly with silver ink, which has a lower viscosity and a higher

conductivity.

The strain gauges produced in this research show many unfavorable characteristics. Phenomena such as creep and hysteresis were to be expected since the material that contains the strain gauges has these attributes as well. But there is a clear difference between the mechanical response and the strain gauge response. This makes it hard to relate the sensor output to the mechanical input. Additionally, there is a difference in response between the various produced strain gauges. The previously mentioned differences in absolute resistance values plus differences in responsivity will make it difficult to use the gauges in a Wheatstone bridge as intended for the designed sensor. The difference in absolute values will create an unbalanced bridge of which the output is difficult to amplify. Readout is further complicated by the drift in the resistors. For now, the graphite paint seems the more appropriate candidate for usage in strain sensing as the produced resistances are more consistent and lower than the ones produced with carbon glue. However, before the strain gauges can actually be used in sensing applications, the production method should be more reliable.

To conclude, the onset to a different approach of fabricating sensors is introduced but there are still several bumps in the road to a reliable process.

Acknowledgements

I want to thank some people in particular who have helped me during this assignment.

Gijs, I want to thank you for giving me the opportunity for doing this research. A project entirely about 3D printing was something I could only dream of (At the end of the project though, sometimes these dreams became nightmares). I really enjoyed the many fruitful discussions we had, sometimes not even about the project itself. There was always the need to stay sharp and I think I have learned a lot from this. Further, you were always there to help me solving theoretical problems but also more practical problems involving building a proper Latex main file for example.

Remco (Pino), without your help I would be nowhere. Both your theoretical and practical knowledge about building measurement setups were invaluable. Next to the technical help, it was your humor which helped me survive this assignment.

Theo, you helped me a lot with designing the capacitive parts of the sensor and the corresponding measurement setup. Thank you for that.

I want to thank Johan and Wouter for taking the time to be a member of my committee and to read this report.

Further, I want show my gratitude to everybody who came by in the lab for the help, countless enlightening conversations and criticizing my music taste (and computer mouse), the people who read the report searching for some final textual improvements, and all my fellow students who made that I had a great time doing my assignment.

References

- [1] Kenneth H Church, Harvey Tsang, Ricardo Rodriguez, Paul Defembaugh, Raymond Rumpf, and El Paso. Printed Circuit Structures , the Evolution of Printed Circuit Boards The University of Texas at El Paso. 2013.
- [2] Mohammad Vaezi, Srisit Chianrabutra, Brian Mellor, and Shoufeng Yang. Multiple material additive manufacturing – Part 1: a review. *Virtual and Physical Prototyping*, 8(1):19–50, mar 2013. ISSN 1745-2759. doi: 10.1080/17452759.2013.778175. URL <http://www.tandfonline.com/doi/abs/10.1080/17452759.2013.778175>.
- [3] Graphene3DLabs. Investor Presentation. URL <http://graphenelab.com/pdf/Investor-Presentation-GGG.pdf>.
- [4] Jorge Mireles, Ho-Chan Kim, In Hwan Lee, David Espalin, Francisco Medina, Eric MacDonald, and Ryan Wicker. Development of a Fused Deposition Modeling System for Low Melting Temperature Metal Alloys. *Journal of Electronic Packaging*, 135(1):011008, feb 2013. ISSN 1043-7398. doi: 10.1115/1.4007160. URL <http://electronicpackaging.asmedigitalcollection.asme.org/article.aspx?doi=10.1115/1.4007160>.
- [5] Dr. Ian Gibson, Dr David W. Rosen, and Dr. Brent Stucker. *Additive Manufacturing Technologies*. Springer Science & Business Media, 2010. ISBN 978-1-4419-1119-3.
- [6] Yi Liu, Tianhong Cui, and Kody Varahramyan. All-polymer capacitor fabricated with inkjet printing technique. *Solid-State Electronics*, 47(9):1543–1548, sep 2003. ISSN 00381101. doi: 10.1016/S0038-1101(03)00082-0. URL <http://linkinghub.elsevier.com/retrieve/pii/S0038110103000820>.
- [7] Amit J. Lopes, In Hwan Lee, Eric MacDonald, Rolando Quintana, and Ryan Wicker. Laser curing of silver-based conductive inks for in situ 3D structural electronics fabrication in stereolithography. *Journal of Materials Processing Technology*, 214(9):1935–1945, sep 2014. ISSN 09240136. doi: 10.1016/j.jmatprotec.2014.04.009. URL <http://linkinghub.elsevier.com/retrieve/pii/S0924013614001411>.
- [8] Seung Hwan Ko, Jaewon Chung, Heng Pan, Costas P. Grigoropoulos, and Dimos Poulikakos. Fabrication of multilayer passive and active electric components on polymer using inkjet printing and low temperature laser processing. *Sensors and Actuators A: Physical*, 134(1):161–168, feb 2007. ISSN 09244247. doi: 10.1016/j.sna.2006.04.036. URL <http://linkinghub.elsevier.com/retrieve/pii/S0924424706003220>.
- [9] Efrain Aguilera, Jorge Ramos, David Espalin, and Fernando Cedillos. 3D Printing of Electro Mechanical Systems. pages 950–961, 2013.

- [10] Matt Saari, Bin Xia, Bryan Cox, Paul S. Krueger, Adam L. Cohen, and Edmond Richer. Fabrication and Analysis of a Composite 3D Printed Capacitive Force Sensor. *3D Printing and Additive Manufacturing*, 3(3):136–141, 2016. ISSN 2329-7662. doi: 10.1089/3dp.2016.0021. URL <http://online.liebertpub.com/doi/10.1089/3dp.2016.0021>.
- [11] J Mizuno, S Takahashi, and A Design Considerations. Design and Fabrication of an Electrostatically Actuated Parallel-Plate Mirror by 3D-Printer. 8(5):923–925, 2014.
- [12] P Laszczak, L Jiang, D L Bader, D Moser, and S Zahedi. Development and validation of a 3D-printed interfacial stress sensor for prosthetic applications. *Medical engineering & physics*, 37(1):132–7, jan 2015. ISSN 1873-4030. doi: 10.1016/j.medengphy.2014.10.002. URL <http://www.ncbi.nlm.nih.gov/pubmed/25455164>.
- [13] Yoshio Ishiguro and Ivan Poupyrev. 3D Printed Interactive Speakers. 2014.
- [14] B. B. Edin, L. Ascari, L. Beccai, S. Roccella, J. J. Cabibihan, and M. C. Carrozza. Bio-inspired sensorization of a biomechatronic robot hand for the grasp-and-lift task. *Brain Research Bulletin*, 75(6):785–795, 2008. ISSN 03619230. doi: 10.1016/j.brainresbull.2008.01.017.
- [15] Ahmed M. Almassri, W. Z. Wan Hasan, S. A. Ahmad, A. J. Ishak, A. M. Ghazali, D. N. Talib, and Chikamune Wada. Pressure sensor: State of the art, design, and application for robotic hand. *Journal of Sensors*, 2015, 2015. ISSN 16877268. doi: 10.1155/2015/846487.
- [16] Changcheng Wu, Aiguo Song, Yun Ling, Nan Wang, and Lei Tian. A control strategy with tactile perception feedback for emg prosthetic hand. *Journal of Sensors*, 2015, 2015. ISSN 16877268. doi: 10.1155/2015/869175.
- [17] Michela Borghetti, Emilio Sardini, and Maur Serpelloni. Sensorized glove for measuring hand finger flexion for rehabilitation purposes. *IEEE Transactions on Instrumentation and Measurement*, 62(12):3308–3314, 2013. ISSN 00189456. doi: 10.1109/TIM.2013.2272848.
- [18] Eric Macdonald, Rudy Salas, David Espalin, Mireya Perez, Efrain Aguilera, D A N Muse, and Ryan B Wicker. 3D Printing for the Rapid Prototyping of Structural Electronics. *IEEE Access*, 2:234–242, 2014.
- [19] John P Swensen, Brandon Araki, and Aaron M Dollar. Printing Three-Dimensional Electrical Traces in Additive Manufactured Parts for Injection of Low Melting Temperature Metals. *Journal of Mechanisms and Robotics*, 7(May):1–10, 2015. doi: 10.1115/1.4029435.
- [20] Sung-yueh Wu, Chen Yang, Wensyang Hsu, and Liwei Lin. 3D-printed microelectronics for integrated circuitry and passive wireless sensors. *Microsystems & Nanoengineering*, 1(June):1–9, 2015. doi: 10.1038/micronano.2015.13.
- [21] Hiroki Ota, Sam Emaminejad, Yuji Gao, Allan Zhao, Eric Wu, Samyuktha Challa, Kevin Chen, Hossain M Fahad, Amit K Jha, Daisuke Kiriya, Wei Gao, Hiroshi Shiraki, Kazuhito Morioka, Adam R Ferguson, Kevin E Healy, Ronald W Davis, and Ali Javey. Application of 3D Printing for Smart Objects with Embedded Electronic

- Sensors and Systems. *Advanced Materials Technologies*, pages 1–8, 2016. doi: 10.1002/admt.201600013.
- [22] Shingo Harada, Kenichiro Kanao, Yuki Yamamoto, Takayuki Arie, Seiji Akita, and Kuniharu Takei. Fully Printed Flexible Fingerprint-like Three-Axis Tactile and Slip Force and Temperature Sensors for Artificial Skin. *ACS Nano*, 8(12):12851–12857, 2014.
- [23] See Tingrui. Microfluidic tactile sensors for three-dimensional contact force measurements. *Lab on a Chip*, 14(22):4344–4353, 2014. ISSN 1473-0197. doi: 10.1039/C4LC00746H. URL <http://dx.doi.org/10.1039/C4LC00746H>.
- [24] Nima Izadi. Bio-Inspired MEMS Aquatic Flow Sensor Arrays. Technical report, University of Twente, 2011.
- [25] D.M. Stefanescu. *Handbook of Force Transducers*. 2011. ISBN 9788578110796. doi: 10.1017/CBO9781107415324.004.
- [26] T.S.J. Lammerink, J Groenesteijn, J.C. Lötters, and R.J. Wiegerink. Readout circuit for capacitance ratio measurement. In *41st International Conference on Micro- and Nano-Engineering*, 2015.
- [27] Hyunki In, Brian Byunghyun Kang, and MinKi Sin. Exo-Glove: A Wearable Robot for the Hand with a Soft Tendon Routing System. *IEEE Robotics & Automation Magazine*, 22(1):97–105, 2015.
- [28] G. N. Weisensel. Natural Frequency Information Plates for Circular and Annular Plates. *Sound and Vibration*, 133(1):129–134, 1989.
- [29] R. J. Roark, W. C. Young, and R. Plunkett. *Formulas for Stress and Strain*, volume 43. 1976. ISBN 0070530319. doi: 10.1115/1.3423917.
- [30] Edin Terzic, Jenny Terzic, Romesh Iagarajah, and Muhammad Alamgir. *A Neural Network Approach to Fluid Quantity Measurement in Dynamic Environments*. Springer Science & Business Media, 1st edition, 2012. ISBN 978-1-4471-4060-3.
- [31] F. Molina-Lopez, D. Briand, and N.F. de Rooij. All additive inkjet printed humidity sensors on plastic substrate. *Sensors and Actuators B: Chemical*, 166-167:212–222, may 2012. ISSN 09254005. doi: 10.1016/j.snb.2012.02.042. URL <http://linkinghub.elsevier.com/retrieve/pii/S0925400512001748>.
- [32] David Roylance. Engineering viscoelasticity. *Department of Materials Science and Engineering - Massachusetts Institute of Technology, Cambridge*, pages 1–37, 2001. ISSN 0885-3010. doi: 10.1007/978-1-4614-8139-3.
- [33] Chawla k.k. meyers M.A. *Mechanical Behavior of Materials. 2007*. 2007. ISBN 9780521866750.
- [34] María L Cerrada. Introduction to the Viscoelastic Response in Polymers. *Thermal Analysis. Fundamentals and Applications to Material Characterization.*, pages 175–177, 2005. URL <http://ruc.udc.es/dspace/handle/2183/11487>.

- [35] Song Chen, Yong Wei, Siman Wei, Yong Lin, and Lan Liu. Ultrasensitive Cracking-Assisted Strain Sensors Based on Silver Nanowires/Graphene Hybrid Particles. *ACS Applied Materials and Interfaces*, 8(38):25563–25570, 2016. ISSN 19448252. doi: 10.1021/acsami.6b09188.
- [36] Michela Borghetti, Mauro Serpelloni, Emilio Sardini, and Stefano Pandini. Mechanical behavior of strain sensors based on PEDOT:PSS and silver nanoparticles inks deposited on polymer substrate by inkjet printing. *Sensors and Actuators, A: Physical*, 243:71–80, 2016. ISSN 09244247. doi: 10.1016/j.sna.2016.03.021. URL <http://dx.doi.org/10.1016/j.sna.2016.03.021>.
- [37] Chaoyi Yan, Jiangxin Wang, Wenbin Kang, Mengqi Cui, Xu Wang, Ce Yao Foo, Kenji Jianzhi Chee, and Pooi See Lee. Highly stretchable piezoresistive graphene-nanocellulose nanopaper for strain sensors. *Advanced Materials*, 26(13):2022–2027, 2014. ISSN 15214095. doi: 10.1002/adma.201304742.
- [38] Chan Ho Park, Hector F Rios, Qiming Jin, Megan E Bland, Colleen L Flanagan, Scott J Hollister, and William V Giannobile. Biomimetic hybrid scaffolds for engineering human tooth-ligament interfaces. *Biomaterials*, 31(23):5945–5952, aug 2010. ISSN 1878-5905. doi: 10.1016/j.biomaterials.2010.04.027. URL <http://www.pubmedcentral.nih.gov/articlerender.fcgi?artid=2893240&tool=pmcentrez&rendertype=abstract>.
- [39] Ruben D. Ponce Wong, Jonathan D. Posner, and Veronica J. Santos. Flexible microfluidic normal force sensor skin for tactile feedback. *Sensors and Actuators, A: Physical*, 179:62–69, 2012. ISSN 09244247. doi: 10.1016/j.sna.2012.03.023. URL <http://dx.doi.org/10.1016/j.sna.2012.03.023>.
- [40] Daniel M. Vogt, Yong-Lae Park, and Robert J. Wood. Design and Characterization of a Soft Multi-Axis Force Sensor Using Embedded Microfluidic Channels. *IEEE Sensors Journal*, 13(10):4056–4064, 2013. ISSN 1530-437X. doi: 10.1109/JSEN.2013.2272320. URL <http://ieeexplore.ieee.org/lpdocs/epic03/wrapper.htm?arnumber=6553251>.
- [41] Yong Lae Park, Bor Rong Chen, and Robert J. Wood. Design and fabrication of soft artificial skin using embedded microchannels and liquid conductors. *IEEE Sensors Journal*, 12(8):2711–2718, 2012. ISSN 1530437X. doi: 10.1109/JSEN.2012.2200790.
- [42] Bin Li, Adam K. Fontecchio, and Yon Visell. Mutual capacitance of liquid conductors in deformable tactile sensing arrays. *Applied Physics Letters*, 108(1):1–4, 2016. ISSN 00036951. doi: 10.1063/1.4939620. URL <http://dx.doi.org/10.1063/1.4939620>.
- [43] H O Michaud, J Teixidor, and S P Lacour. Soft flexion sensors integrating stretchable metal conductors on a silicone substrate for smart glove applications. *Micro Electro Mechanical Systems (MEMS), 2015 28th IEEE International Conference on*, pages 760–763, 2015. doi: 10.1109/MEMSYS.2015.7051069.
- [44] Frank L. Hammond, Yi??it Menguc, and Robert J. Wood. Toward a modular soft sensor-embedded glove for human hand motion and tactile pressure measurement. *IEEE International Conference on Intelligent Robots and Systems*, (Iros):4000–4007, 2014. ISSN 21530866. doi: 10.1109/IROS.2014.6943125.

- [45] Yong-Lae Park, Bor-rong Chen, Néstor O Pérez-Arancibia, Diana Young, Leia Stirling, Robert J Wood, Eugene C Goldfield, and Radhika Nagpal. Design and control of a bio-inspired soft wearable robotic device for ankle-foot rehabilitation. *Bioinspiration & biomimetics*, 9(1):016007, 2014. ISSN 1748-3190. doi: 10.1088/1748-3182/9/1/016007. URL <http://iopscience.iop.org/article/10.1088/1748-3182/9/1/016007>.
- [46] Yin Nee Cheung, Yun Zhu, Ching Hsiang Cheng, Chen Chao, and Wallace Woon Fong Leung. A novel fluidic strain sensor for large strain measurement. *Sensors and Actuators, A: Physical*, 147(2):401–408, 2008. ISSN 09244247. doi: 10.1016/j.sna.2008.05.013.
- [47] Andreas Frutiger, Joseph T Muth, Daniel M Vogt, Yiğit Mengüç, Alexandre Campo, Alexander D Valentine, Conor J Walsh, and Jennifer a Lewis. Capacitive Soft Strain Sensors via Multicore-Shell Fiber Printing. *Advanced materials (Deerfield Beach, Fla.)*, 27(15):2440–6, apr 2015. ISSN 1521-4095. doi: 10.1002/adma.201500072. URL <http://www.ncbi.nlm.nih.gov/pubmed/25754237>.
- [48] Joel Geerlings. *Functional scanning probes for sensing, actuation and deposition*. 2016. ISBN 9789036540339.
- [49] Susan E. Habas, Heather A S Platt, Maikel F A M Van Hest, and David S. Ginley. Low-cost inorganic solar cells: From ink to printed device. *Chemical Reviews*, 110(11):6571–6594, 2010. ISSN 00092665. doi: 10.1021/cr100191d.
- [50] J. Czyzewski, P. Burzyński, K. Gaweł, and J. Meisner. Rapid prototyping of electrically conductive components using 3D printing technology. *Journal of Materials Processing Technology*, 209(12-13):5281–5285, 2009. ISSN 09240136. doi: 10.1016/j.jmatprotec.2009.03.015.
- [51] Morteza Vatani, Yanfeng Lu, Erik D. Engeberg, and Jae-Won Choi. Combined 3D printing technologies and material for fabrication of tactile sensors. *International Journal of Precision Engineering and Manufacturing*, 16(7):1375–1383, 2015. ISSN 2234-7593. doi: 10.1007/s12541-015-0181-3. URL <http://link.springer.com/10.1007/s12541-015-0181-3>.
- [52] Seung Hwan Ko, Jaewon Chung, Nico Hotz, Koo Hyun Nam, and Costas P Grigoriopoulos. Metal nanoparticle direct inkjet printing for low-temperature 3D micro metal structure fabrication. *Journal of Micromechanics and Microengineering*, 20(12):125010, 2010. ISSN 0960-1317. doi: 10.1088/0960-1317/20/12/125010.
- [53] Joseph T. Muth, Daniel M. Vogt, Ryan L. Truby, Yi??it Meng????, David B. Kolesky, Robert J. Wood, and Jennifer A. Lewis. Embedded 3D printing of strain sensors within highly stretchable elastomers. *Advanced Materials*, 26(36):6307–6312, 2014. ISSN 15214095. doi: 10.1002/adma.201400334.
- [54] Ted Pella. Conductive carbon glue. URL <https://www.tedpella.com/technote{ }html/TN{ }16050.pdf>.
- [55] Conor S Boland, Umar Khan, Claudia Backes, Arlene O Neill, Joe Mccauley, Shane Duane, Ravi Shanker, Yang Liu, Izabela Jurewicz, Alan B Dalton, and Jonathan N

- Coleman. Terms of Use Bodily Motion Sensors Based on Graphene À Rubber Composites. (Xx):8819–8830, 2014. ISSN 1936-0851. doi: 10.1021/nn503454h.
- [56] Honglie Song, Junqiu Zhang, Daobing Chen, Kejun Wang, Shichao Niu, Zhiwu Han, and Luquan Ren. Superfast and high-sensitivity printable strain sensors with bioinspired micron-scale cracks. *Nanoscale*, 2017. ISSN 2040-3364. doi: 10.1039/C6NR07333F. URL <http://xlink.rsc.org/?DOI=C6NR07333F>.
- [57] Rosliza Mohamad Zin, Chin Phong Soon, Syalina Ghadafi, Riyaz Ahmad Mohamed Ali, and Nafarizal Nayan. Fabrication and characterisation of the electrical and physical properties of the mask printed graphite paste electrodes on paper substrates. *International Journal of Nanoelectronics and Materials*, 8(1):47–53, 2015. ISSN 22321535. doi: 10.4028/www.scientific.net/AMR.925.510.
- [58] Junhui Zhao, Kun Dai, Chenggang Liu, Guoqiang Zheng, Bo Wang, Chuntai Liu, Jingbo Chen, and Changyu Shen. A comparison between strain sensing behaviors of carbon black/polypropylene and carbon nanotubes/polypropylene electrically conductive composites. *Composites Part A: Applied Science and Manufacturing*, 48(1):129–136, 2013. ISSN 1359835X. doi: 10.1016/j.compositesa.2013.01.004. URL <http://dx.doi.org/10.1016/j.compositesa.2013.01.004>.
- [59] MJM schematic. URL <https://kylestetzerp.wordpress.com/2009/05/20/inkjet-and-multijet-printing/>.
- [60] 3DSystems. Projet characteristics. URL <http://www.3dsystems.com/sites/www.3dsystems.com/files/mjp{ }plastic{ }specsheet{ }07.29.16{ }usen.pdf>.
- [61] Kyusuk Baek. Integrated microvalves for cortical drug- delivery at the cellular level. Technical report, University of Michigan, 2009.
- [62] Dong Sung Kim, Kwang-Cheol Lee, Tai Hun Kwon, and Seung S Lee. Micro-channel filling flow considering surface tension effect. *Journal of Micromechanics and Microengineering*, 12(3):236–246, 2002. ISSN 0960-1317. doi: 10.1088/0960-1317/12/3/307. URL <http://stacks.iop.org/0960-1317/12/i=3/a=307>.
- [63] Robin J. Speedy. Kauzmann ’ s paradox and the glass transition. *Biophysical Chemistry*, 105(September 2002):411–420, 2003. ISSN 03014622. doi: 10.1016/S0301-4622. URL <http://www.sciencedirect.com/science/article/pii/S0301462203001054{#}BIB13>.
- [64] Michael J Fuerstman, Ann Lai, Meghan E Thurlow, Sergey S Shevkoplyas, Howard a Stone, and George M Whitesides. The pressure drop along rectangular microchannels containing bubbles. *Lab on a chip*, 7(11):1479–1489, 2007. ISSN 1473-0197. doi: 10.1039/b706549c.
- [65] C. Buffone, K. Sefiane, and J. R E Christy. Experimental investigation of self-induced thermocapillary convection for an evaporating meniscus in capillary tubes using micro-particle image velocimetry. *Physics of Fluids*, 17(5):1–18, 2005. ISSN 10706631. doi: 10.1063/1.1901688.
- [66] Ante Tony Lausic. Manufacturing Optimal Nanocrystalline Microtruss Materials. Technical report, Materials Science and Engineering University of Toronto, 2016.

[67] Stephen D Senturia. *Microsystem Design*, volume 49. 2001. ISBN 0792372468. doi: 10.1007/0-306-47601. URL <http://www.amazon.fr/Microsystem-Design-Stephen-D-Senturia/dp/0792372468>.

Appendix A

Implementing deflection in Matlab

```
1 function [W, DWDRHO, DDWDRHO2, W_S, DW_SDRHO, DDW_SDRHO2, XI, YI ] = ...
2 defl_field(a,b,h_inc,D,P,F_s,phi,res)
3 %function calculating the deflection for a membrane with radius a ...
4   with an
5   %inclusion of radius b. h_inc is the height of the inclusion, D the
6   %flexural rigidity of the membrane, P the normal force applied, F_s the
7   %shear force and phi the direction in which that shear force is applied.
8   %res is the resolution in which the field is evaluated.
9
10  w=zeros(1,res*res);
11  dw_drho=zeros(1,res*res);
12  ddw_drho2=zeros(1,res*res);
13  r=zeros(1,res+1);
14  theta=zeros(1,res+1);
15  polar=zeros(1,res^2,2);
16  w_shear=zeros(1,res*res); %deflection due to shear forces
17  dw_shear_drho=zeros(1,res*res); %first derivative of w_shear
18  ddw_shear_drho2=zeros(1,res*res); %second derivative of w_shear
19  rho=zeros(1,res+1); %normalised radius
20  zeta=b/a; %constant which is the ratio of inclusion to membrane diameter
21  M=F_s*h_inc;
22  A=(M/(8*pi*D)); %constant in front of deflection formula as a ...
23   function of
24   %moment
25  B=(P*a^2)/(16*pi*D); %constant in front of deflection formula as a ...
26   function
27   %of force
28  for i=1:res
29      r(1,i)=((i-1)/res)*a; %coordinate on the radius
30      rho(1,i)=r(1,i)/a; %rho is the normalised radial coordinate
31
32      for j=1:res
33          theta(1,j)=((2*pi)/res)*(j-1); %theta is the angle of the polar
34          %coordinates
35          w(1,((i-1)*res)+j)=B*(1-rho(1,i)^2+2*rho(1,i)^2*...
36          log(rho(1,i))-((2*zeta^2*log(zeta))/(1-zeta^2))*(1-rho(1,i))^2 ...
37          ...
38          +2*log(rho(1,i)));
39          dw_drho(1,((i-1)*res)+j)=B*((4*r(1,i)*log(r(1,i)/a))/a^2-...
40          (2*(2/r(1,i)-(2*r(1,i))/a^2)*zeta^2*log(zeta))/(1-zeta^2));
```

```

38     ddw_drho2(1, ((i-1)*res)+j)=B*(4/a^2-(2*zeta^2*...
39     (-2/a^2-2/r(1,i)^2)*log(zeta))/(1-zeta^2)+(4*log(r(1,i)/a))/a^2);
40     w_shear(1, ((i-1)*res)+j)=A*((a*(rho(1,i)^2*(1-zeta^2-...
41     rho(1,i)^2+2*log(rho(1,i))+2*log(rho(1,i))*zeta^2)+zeta^2)*...
42     cos(theta(1,j)-phi))/(rho(1,i)*(1+zeta^2)));
43     dw_shear_drho(1, (i-1)*res+j)=A*cos(theta(1,j)-phi)*...
44     (2*log(r(1,i)/a)-((a^2*zeta^2-3*r(1,i)^2)*(a^2-r(1,i)^2))/...
45     (a^2*(1+zeta^2)*r(1,i)^2));
46     ddw_shear_drho2(1, (i-1)*res+j)=(2*A*cos(theta(1,j)-phi)*...
47     (a^4*zeta^2+a^2*(1+zeta^2)*r(1,i)^2-3*r(1,i)^4))/...
48     (a^2*(1+zeta^2)*r(1,i)^3);
49     polar(1, ((i-1)*res)+j,1)=theta(1,j);
50     polar(1, ((i-1)*res)+j,2)=rho(1,i);
51     end
52 end
53 [x,y]=pol2cart(polar(1,:,1),polar(1,:,2));
54 steps = -1:1/res:1;
55 [XI,YI] = meshgrid(steps, steps);
56 for i=1:length(XI)
57     for j=1:length(XI)
58         if(sqrt(XI(i,j)^2+YI(i,j)^2)-(b/a)<0.0001)
59             XI(i,j)=NaN;
60             YI(i,j)=NaN;
61         end
62         if(sqrt(XI(i,j)^2+YI(i,j)^2)>1)
63             XI(i,j);
64             YI(i,j);
65             XI(i,j)=NaN;
66             YI(i,j)=NaN;
67         end
68     end
69 end
70 % now interpolate - find z values for these grid points
71
72 W=griddata(x,y,w,XI,YI);
73 DWDRHO=griddata(x,y,dw_drho,XI,YI);
74 DDWDRHO2=griddata(x,y,ddw_drho2,XI,YI);
75
76 W_S = griddata(x,y,w_shear,XI, YI);
77 DW_SDRHO = griddata(x,y,dw_shear_drho,XI, YI);
78 DDW_SDRHO2 = griddata(x,y,ddw_shear_drho2,XI,YI);
79
80 end

```

Appendix B

Strain in a circular membrane with inclusion

```
1 function [str_N, str_S, r] = ...
2     strain(a,b,D,P,F_s,phi,theta, z,h_inc,res)
3 %STRAIN this function calculates the strain in a circular membrane with
4 %radius a with an thick inclusion of radius b and height h_inc. D is the
5 %flexural rigidity of the membrane. P is the applied force in newton and
6 %F_s the applied shear force. Phi is the direction of the applied shear
7 %force in radian and theta the direction in which the strain is ...
8     evaluated.
9 %z is the distance from the neutral plane at which the strain is
10 %calculated. res is the resolution with which the calculations are done.
11 %The function returns an array with strains due to normal force str_N
12 %and a multidimensional array str_S which contains the strain on both
13 %sides of the inclusion generated by the shear force. r contains the
14 %evaluated positions.
15     M=F_s*h_inc;
16     A=(M/(8*pi*D));
17
18     B=(P*a^2)/(16*pi*D); %constant in front of deflection formula as ...
19     a ...
20     %function of force
21     zeta=b/a; %constant which is the ratio of inclusion to membrane ...
22     diameter
23     str_N=zeros(1,res+1);
24     str_S=zeros(2,res+1);
25     r=zeros(1,res+1);
26
27     for i=1:res+1
28         r(1,i)=b+(a-b)/res*(i-1);
29         str_N(1,i)= ...
30             z*B*(4/a^2-(2*zeta^2*(-2/a^2-2/r(1,i)^2)*log(zeta))/ ...
31                 (1-zeta^2)+(4*log(r(1,i)/a))/a^2);
32         str_S(1,i)= ...
33             z*(2*A*cos(theta-phi)*(a^4*zeta^2+a^2*(1+zeta^2)* ...
34                 r(1,i)^2-3*r(1,i)^4))/(a^2*(1+zeta^2)*r(1,i)^3);
35     end
36     theta=theta+pi;
37     for i=1:res+1
```

```
36     str_S(2,i)= ...
37         z*(2*A*cos(theta-phi)*(a^4*zeta^2+a^2*(1+zeta^2))* ...
38         r(1,i)^2-3*r(1,i)^4)/(a^2*(1+zeta^2)*r(1,i)^3);
39     end
40 end
```

Appendix C

Resistance change in straight and tapered channels

This appendix contains a more detailed explanation for solving the relative resistance change in straight and tapered channels. The path of the strain gauge goes from one side to the neutral plane to the other. This way it experiences the same sign strain all along its way until it ends up at the capacitor plate (Figure C.1). The equation to be solved to assess the relative change in resistance due to strain as a result of normal force is as follows:

$$\begin{aligned} \frac{\Delta R}{R} &= (1 + 2\nu) \frac{\int_{R_h}^{S-\frac{1}{2}d} \frac{1}{A_a(r)} \epsilon(r) dr + \int_{S+\frac{1}{2}d}^{R_m} \frac{1}{A_b(r)} \epsilon(r) dr}{\rho_R \int \frac{1}{A(r)} dr} \\ &= (1 + 2\nu) \frac{-z \int_{R_h}^{S-\frac{1}{2}d} \frac{1}{A_a(r)} \frac{d^2 w_n}{dr^2} dr + z \int_{S+\frac{1}{2}d}^{R_m} \frac{1}{A_b(r)} \frac{d^2 w_n}{dr^2} dr}{\int_{R_h}^{S-\frac{1}{2}d} \frac{1}{A_a(r)} dr + \int_{-z-\frac{1}{2}h}^{z+\frac{1}{2}h} \frac{1}{A_c} dz + \int_{S+\frac{1}{2}d}^{R_m} \frac{1}{A_b(r)} dr + \frac{1}{2} \int \frac{1}{A_{\text{cap}}(y)} dy} \end{aligned} \quad (\text{C.1})$$

For both the straight and the tapered channel counts:

$$\frac{\partial^2 w_n(r)}{\partial r^2} = \frac{P \cdot R_m^2}{16 \cdot \pi \cdot D} \left(\frac{4}{R_m^2} - \frac{2 \cdot \zeta^2 \left(-\frac{2}{R_m^2} - \frac{2}{r^2}\right) \cdot \ln(\zeta)}{1 - \zeta^2} + \frac{4 \cdot \ln\left(\frac{r}{R_m}\right)}{R_m^2} \right) \quad (\text{C.2})$$

Also, the shape of the capacitor plate will be the same for both channels. The resistance of half of the capacitance plate is approximated by expressing the width of the plate as a function of y and then integrating from $y = 0$ to $y = E$ (Figure C.2). The height is constant being $2z + h$. The resulting integral is as follows:

$$\frac{1}{2} \int \frac{1}{A_{\text{cap}}(y)} dy = \int_0^E \frac{1}{A_{\text{cap}}(y)} dy = \int_0^{R_h \sin \theta} \frac{1}{(h + 2 \cdot z) (\sqrt{b^2 - y^2} - \left(\frac{\cos(\theta)}{\sin(\theta)}\right) \cdot y + r_0)} dy \quad (\text{C.3})$$

with:

$$\theta = 2 \cdot \tan^{-1} \left(\frac{\sqrt{2 \cdot R^2 - r_0^2} - R}{r_0 + R} \right) \quad (\text{C.4})$$

Furthermore, for straight channels:

$$A_a(r) = A_b(r) = wh \quad (\text{C.5})$$

$$A_c = dw \quad (C.6)$$

And for tapered channels:

$$A_a(r) = h \cdot \left(\frac{w}{T - \frac{1}{2}d} \right) \quad (C.7)$$

$$A_b(r) = 2 \cdot h \cdot \left(\frac{\frac{1}{2}w_1 - \frac{1}{2}w_3}{a - T + \frac{1}{2}d} \cdot \left(\frac{(a - T + \frac{1}{2}d) \cdot \frac{1}{2}w_3}{\frac{1}{2}w_1 - \frac{1}{2}w_3} + a \right) - \frac{(\frac{1}{2}w_1 - \frac{1}{2}w_3)}{(a - T + \frac{1}{2}d)} \cdot r \right) \quad (C.8)$$

$$A_c = dw_1 \quad (C.9)$$

These relations for cross-sectional area and strain have been implemented in C.1. The result is worked out and solved using the Matlab code found on the next pages.

```

1 function [ Rel_R_ch ] = RelRChange_new_new(P,a,b,D,mu,z,h,rho_c,T,...
2     w_1,d,w_2,r0,type )
3 %RelRChange calculates the relative resistance change and the ...
4     resistance of
5 %two types of channels. one channel is chaped like <=> and the other
6 %channel is simply straight =. P is the pressure on the sensor, a is the
7 %radius of the membrane, b is the diameter of the inclusion, D is the
8 %flexural rigidity of the membrane, mu is the poisson ratio of the ...
9     material
10 %the membrane is made of, z is the distance of the channels with respect
11 %to the neutral plane, h is the height of the channels, rho_c is the
12 %conductivity of the material in the channels, T is the point ...
13     between b and
14     a where the strain changes sign, w is either the final width of the
15 %channel or the width of the channel in case of a straight channel, ...
16     d is
17 %the width of the zero-crossing channel.
18
19 %select type of channel.
20 if type==1
21     Z=[-z z];
22 end
23
24 if type==2
25     Z=[z -z];
26 end
27
28 num=zeros(2,4); %contains the resistance change/rho_c of the resistor
29 %parts parallel to the neutral plane
30 den=zeros(2,4); %contains the R/rho_c of the resistor parts parallel
31 %to the neutral plane
32 int=[b T-0.5*d T+0.5*d a]; %the integration boundaries for the different
33 %parts of the channels
34 zeta=b/a; %ratio of the radius of the membrane to the radius of the
35 %inclusion
36 K=(P*a^2)/(16*pi*D); %constant in front of deflection formula as a
37 %function of force
38 Rel_R_ch=zeros(2,2); %1,1 and 1,2 contain the relative resistance
39 %changes, 2,1 and 2,2 the resistances
40 D=1/((w_1/(T-0.5*d))*h); %rate of with change first part of the channel
41 %integrals for first parts channel (b to T-0.5d)
42 for i=1:2
43     r=int(i);
44     num(1,i)=D*(2*K*(zeta^2*log(zeta)*(a^2-2*r^2*log(r))+(-1+zeta^2)...
45         *r^2*(2*log(r)+log(r/a)^2)))/(a^2*(-1+zeta^2)*r^2);
46     den(1,i)=D*log(r);
47     num(2,i)=(K*((4*r*log(r/a))/a^2-(2*(2/r-(2*r)/a^2)*zeta^2*log(zeta))...
48         /(1-zeta^2)))*(1/(h*w_1));
49     den(2,i)=r/(h*w_1);
50 end
51 %constants which define the offset and the rate of change of the ...
52     line which
53 %defines the width of the last part of the channel.
54 c=w_2; % (0.5*w_1)/(T-(1/2)*d)*b;
55 A=((0.5*w_1-c)/(a-T+0.5*d))*((a-T+0.5*d)*c)/(0.5*w_1-c+a);
56 B=(0.5*w_1-c)/(a-T+0.5*d);
57 %integrals for the last parts of the channel (T+0.5d to a)

```

```

53 for i=3:4
54     r=int(i);
55     num(2,i)=(K*((4*r*log(r/a))/a^2-(2*(2/r-(2*r)/a^2)*zeta^2*...
56         log(zeta))/(1-zeta^2)))/(1/(h*w_1));
57     den(1,i)=-((log(2*h*(A-B*r)))/(2*h*B));
58     den(2,i)=r/(w_1*h);
59 end
60
61 fun = @(x) (K.*(4./a.^2-(2.*zeta.^2.*(-2./a.^2-2./x.^2).*log(zeta))...
62     ./ (1-zeta.^2)+(4.*log(x./a))/a.^2))./(2.*h.*(A-B.*x));
63 dPart3 = integral(fun,T+0.5*d,a); %'AbsTol',0,'RelTol',1e-10)
64 %crossing is the part of the channel which crosses the neutral plane
65 crossing = (2*z+h)/(w_1*d);
66
67 %the resistance of the plate is taken into account here
68 %theta is used to calculate the max y coordinate of the plate and
69 %accompanying x value (E and D)
70 theta = 2*atan((sqrt(2*b^2-r0^2)-b)/(r0+b));
71 phi = atan((0.5*w_1)/(T-0.5*d));
72 gamma = theta-phi;
73 %C is the y-coordinate of the middle of the end of the resistance ...
    channel
74 C=sin(gamma)*b;
75 D=cos(theta)*b;
76 E=sin(theta)*b;
77 %with and therefore the surface of the resistor changes with y
78 fun2 = @(x) (1./((sqrt(b.^2-x.^2)-((D./E).*x+r0)).*(h+2.*z)));
79 ymin=0;
80 ymax=E;
81 %integration from 0 to C to get half of the resistance (rho_c not ...
    included)
82 R_plate=integral(fun2,ymin,ymax);
83 %multiplying by 2 to get the entire resistance (rho_c not included)
84 R_plate=2*R_plate;
85
86
87 %relative resistance change in <=> channel. Remember, 2 resistance ...
    channels
88 %to the plate, hence times 2.
89 Rel_R_ch(1,1)=(1+2*mu)*((2*Z(1)*(num(1,2)-num(1,1))+2*Z(2)*dPart3)/...
90     (2*(den(1,2)-den(1,1)+crossing+den(1,4)-den(1,3))+R_plate));
91 %absolute resistance under no strain
92 Rel_R_ch(2,1)=rho_c*(2*(den(1,2)-den(1,1)+crossing+den(1,4)-den(1,3))...
93     +R_plate);
94 %relative resistance change in straight channel =
95 Rel_R_ch(1,2)=(1+2*mu)*((2*Z(1)*(num(2,2)-num(2,1))+2*Z(2)*...
96     (num(2,4)-num(2,3)))/(2*(den(2,2)-den(2,1)+crossing+...
97     den(2,4)-den(2,3))+R_plate));
98 %absolute resistance under no strain
99 Rel_R_ch(2,2)=rho_c*(2*(den(2,2)-den(2,1)+crossing+den(2,4)-den(2,3))...
100     +R_plate);
101
102 end

```

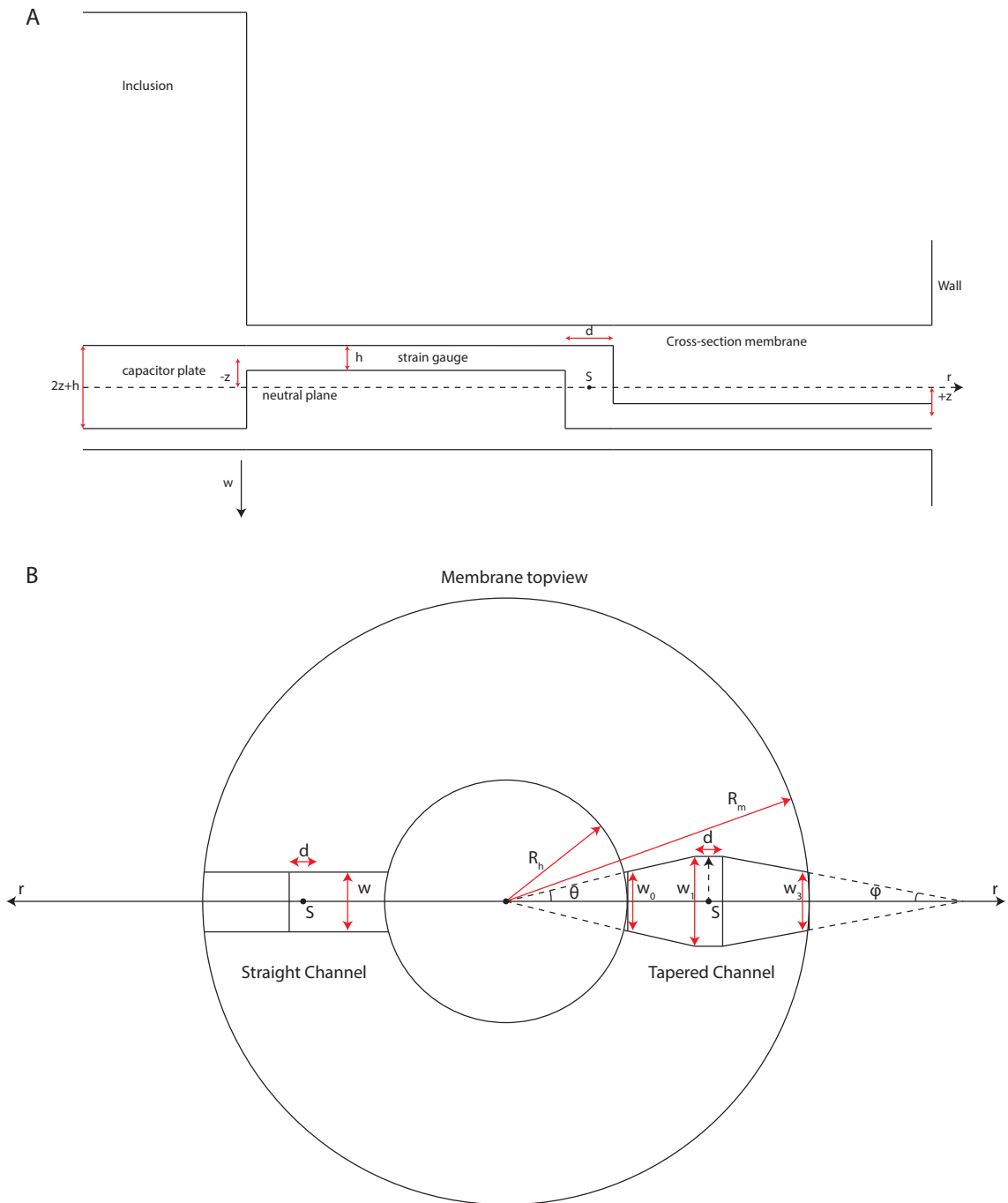


Figure C.1: A. A cross section of the membrane. The strain gauge goes from one side to the neutral plane to the other and ends up in the capacitor plate. B. Two channels are evaluated; One with straight channel walls and one with tapered walls.

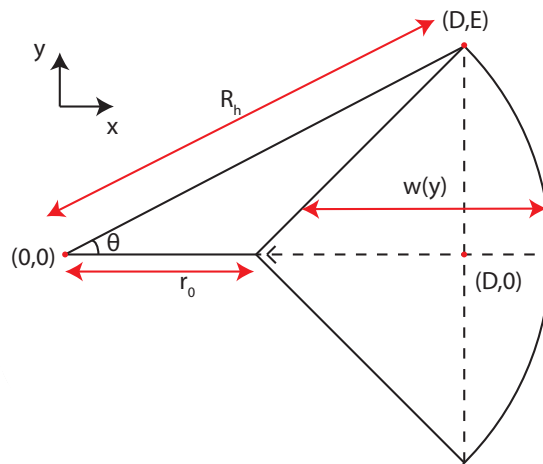


Figure C.2: The resistance of the capacitor plate is estimated by expressing the width as a function of y and integrating from 0 to E .

Appendix D

Capacitance of capacitor plates in a circular membrane with an inclusion

```
1 function [Cap] = capacitance(a,b,D,h_inc,d0,r0,eps,F_s,P,phi)
2 %capacitance: this function returns the capacitance of each of four
3 %capacitorplates of a sensor consisting of a membrane with radius a (m)
4 %with an inclusion with radius (b). The capacitor plates are located ...
   in the
5 %inclusion forming a quarter with radius b. Instead of being a total
6 %quarter, the edges forming an angle of 90 degrees come together ...
   with an
7 %offset r0 with respect to the center. One can apply a normal force ...
   P (N)
8 %and a shear force F_s (N) with direction phi (radians. The initial ...
   gap is
9 %defined by d0 (m), the height of the inclusion is defined by h_inc ...
   (m). D
10 %is the flexural rigidity of the plate. eps1, eps2 and eps3 are
11 %the dielectric constants of the materials between the plates.
12
13
14 zeta = b/a; %ratio of the radius of the membrane to the radius
15 %of the inclusion
16 eps0 = 8.85e-12; %vacuum permittivity
17 M = h_inc*F_s; %shear force converted to Moment
18 %vertical deflection as a result of the normal force:
19 W_n = ((P*a^2)/(16*pi*D))*(1-(b/a)^2+2*(b/a)^2*log(b/a)-...
20         (2*zeta^2*log(zeta))/(1-zeta^2))*(1-(b/a)^2+2*log(b/a));
21 %the gap d0 minus the deflection due to normal force
22 G=d0(1)-W_n;
23 %derivative of w due to moment at r=b. cos not included
24 C = (M/(8*pi*D))*(2*log(b/a)-((a^2*zeta^2-3*b^2)*(a^2-b^2))/...
25         (a^2*(zeta^2+1)*b^2));
26 gamma=[0 0.5*pi pi 1.5*pi];
27 Cap=zeros(1,4);
28 for i=1:4
29     %functions which should be integrated over the surface (polar
30     %coordinates, x means theta, y means theta) to obtain capacitance
31     fun = @(x,y) y./(G-C.*cos(x-phi-gamma(i)).*y);
32     fun2 = @(x,y) y./d0(2);
33     fun3 = @(x,y) y./d0(3);
```

```

34 %integration boundaries, the lower r boundary (y) is a function
35 %of theta (x)
36 ymin = @(x) r0.*sin(x).*tan(x+(1./4)*pi) + cos(x).*r0;
37 %max r (y) is just the radius of the inclusion
38 ymax = b;
39 %integration of one plate will be done in two times
40 xmin = 0;
41 xmax = 2*atan((sqrt(2*b^2-r0^2)-b)/(r0+b));
42
43 Cap1a = eps0*eps(1)*integral2(fun,xmin,xmax,ymin,ymax, ...
44     'method','iterated','AbsTol',0,'RelTol',1e-10);
45 Cap2a = eps0*eps(2)*integral2(fun2,xmin,xmax,ymin,ymax, ...
46     'method','iterated','AbsTol',0,'RelTol',1e-10);
47 Cap3a = eps0*eps(3)*integral2(fun3,xmin,xmax,ymin,ymax, ...
48     'method','iterated','AbsTol',0,'RelTol',1e-10);
49 ymin = @(x) r0.*sin(x).*tan((x-(1./4)*pi)) + cos(x).*r0;
50 Cap1b = eps0*eps(1)*integral2(fun,2*pi-xmax,2*pi,ymin,ymax, ...
51     'method','iterated','AbsTol',0,'RelTol',1e-10);
52 Cap2b = eps0*eps(2)*integral2(fun2,2*pi-xmax,2*pi,ymin,ymax, ...
53     'method','iterated','AbsTol',0,'RelTol',1e-10);
54 Cap3b = eps0*eps(3)*integral2(fun3,2*pi-xmax,2*pi,ymin,ymax, ...
55     'method','iterated','AbsTol',0,'RelTol',1e-10);
56 %In the end, the two capacitor halves (a and b) are added and
57 %the 3 capacitors in series are combined to one capacitor value
58 Cap(i) = ((Cap1a+Cap1b) * (Cap2a+Cap2b) * (Cap3a+Cap3b)) / ...
59     (((Cap1a+Cap1b) * (Cap2a+Cap2b)) + ((Cap2a+Cap2b) * (Cap3a+Cap3b)) + ...
60     ((Cap1a+Cap1b) * (Cap3a+Cap3b)));
61 end
62
63
64 end

```

Appendix E

Linear deflection of a clamped clamped beam

This appendix describes the modeling of and gives the Matlab code which calculates the deflection of a clamped-clamped beam generated by a normal force applied in the middle (Figure E.1).

For small displacements, the deflection of a clamped-clamped beam is given by:

$$w(x) = \frac{F_N x^2}{48EI} (3L - 4x) \quad (\text{E.1})$$

In which P is the applied force (N), E is the Young's modulus (Pa), L is the length of the beam (m), x is the position on which the deflection is evaluated (m) and I is the inertia of the beam:

$$I = \frac{bt^3}{12} \quad (\text{E.2})$$

Where b is the width of the beam (m) and t is the thickness of the beam (m). All functions described are valid for $0 \leq x \leq \frac{L}{2}$ and can be mirrored in $x = \frac{L}{2}$ to get results for the entire beam. Figure E.2 shows the modeled deflection of a beam with thickness $1260 \mu\text{m}$ and width 25.37 mm for forces in the range of $0 \text{ N} - 25 \text{ N}$.

If again it is assumed that the middle plane remains unstrained, the strain at a

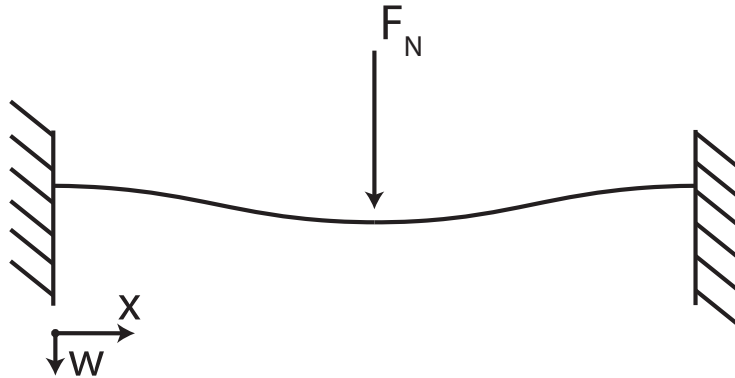


Figure E.1: Deflection of a clamped-clamped beam as a result of a normal force F_n in the middle of the beam.

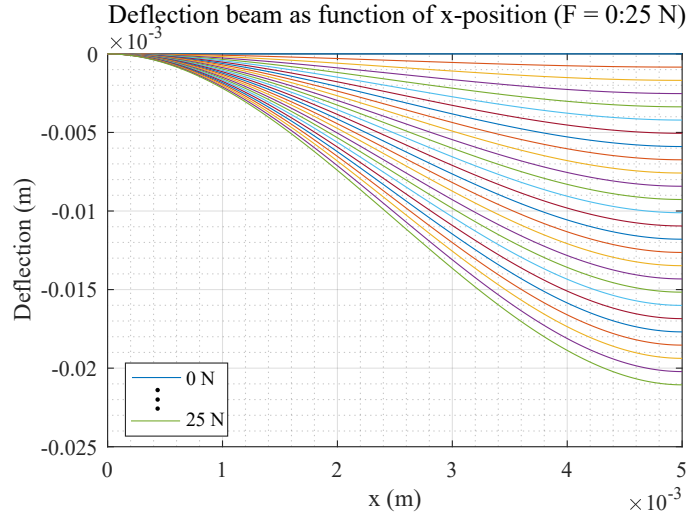


Figure E.2: Graph showing the deflection of a beam w for forces in the range of 0 N–25 N for $x = 0$ to $x = \frac{L}{2}$.

distance z from this plane can be calculated using:

$$\epsilon = z \left(\frac{d^2 w}{dx^2} \right) \quad (\text{E.3})$$

The first and second derivative with respect to x are given by:

$$\frac{dw(x)}{dx} = \frac{F_N}{48EI} (6xL - 12x^2) \quad (\text{E.4})$$

$$\frac{d^2 w(x)}{dx^2} = \frac{F_N}{48EI} (6L - 24x) \quad (\text{E.5})$$

The strain varies linearly over the length of the beam from $x = 0$ to $x = \frac{L}{2}$ as is shown in Figure E.3.

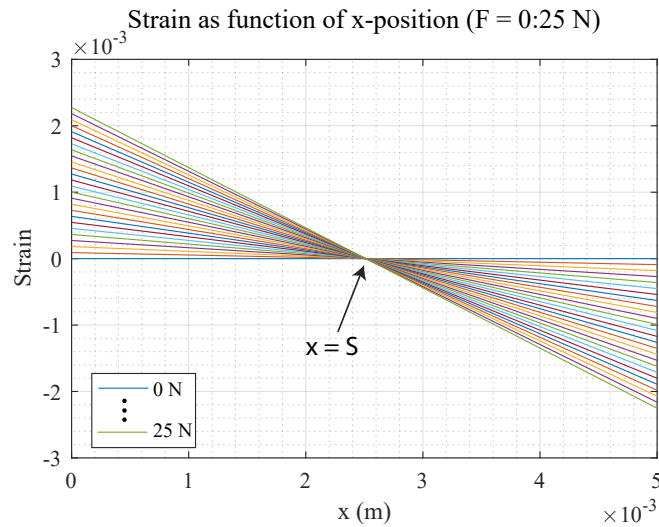


Figure E.3: Graph showing the strain in a beam at a distance $z = 450 \mu\text{m}$ from the neutral plane for forces in the range of 0 N–25 N for $x = 0$ to $x = \frac{L}{2}$.

For each applied force, the graph crosses the zero strain point at $x = S$. For a clamped-clamped beam this point is located at $x = \frac{L}{4}$. This leads to a channel design as shown in Figure E.4, in which the channel crosses the neutral plane and goes from z to $-z$ at point $x = S$.

To assess the relative resistance change in the channel generated by a strain one has to divide the resistance after straining the gauge by the original resistance:

$$\frac{\Delta R}{R} = \frac{\rho_R \int \left(\frac{1}{A(r)}\right) (1 + 2\nu) \epsilon(r) dx}{\rho_R \int \frac{1}{A(x)} dx} = \frac{\int \left(\frac{1}{A(x)}\right) (1 + 2\nu) \epsilon(x) dx}{\int \frac{1}{A(x)} dx} \quad (\text{E.6})$$

Two channels shapes will be compared, as E.6 indicates that channels which locally have a higher resistance at higher strained areas have a higher relative resistance change when strained. One channel has got the same height and width over the entire channel length. The other has the same height, but the width increases from w_0 to $w_0 + 2w_1$ from $x = 0$ to $x = b$, then remains $w_0 + 2w_1$ from $x = b$ to $x = c$, and from $x = c$ to $x = \frac{L}{2}$ the width decreases again to w_0 . Version one will be called the straight channel whereas the latter will be called the tapered channel.

First E.6 will be carried out for the straight channel. The channel basically consists out of two horizontal parts and one vertical one. Each part has their own integration boundaries as stated in Figure E.4. This leads to working out E.7 in the following manner:

$$\frac{\Delta R}{R} = \frac{z\rho_R(1 + 2\nu)(M(x) - N(x))}{\rho_R(O(x) + P(x) + Q(x))} \quad (\text{E.7})$$

Where:

$$\begin{aligned} M(x) &= \frac{1}{wh} \int_0^b \epsilon(x) dx = \frac{1}{wh} \int_0^b \frac{F_N}{48EI} (6L - 24x) dx = \frac{F_N}{48whEI} [6xL - 12x^2]_0^b \\ &= \frac{F_N}{48whEI} (6bL - 12b^2) \end{aligned}$$

$$\begin{aligned} N(x) &= \frac{1}{wh} \int_c^{\frac{1}{2}L} \epsilon(x) dx = \frac{1}{wh} \int_c^{\frac{1}{2}L} \frac{F_N}{48EI} (6l - 24x) dx = \frac{F_N}{48whEI} [6xL - 12x^2]_c^{\frac{1}{2}L} \\ &= \frac{F_N}{48whEI} (12c^2 - 6cL) \end{aligned}$$

$$O(x) = \int_0^b \frac{1}{A(x)} dx = \frac{b}{wh}$$

$$P(x) = \int_{-z-\frac{1}{2}h}^{z+\frac{1}{2}h} \frac{1}{w(c-b)} dz = \frac{2z+h}{w(c-b)}$$

$$Q(x) = \int_c^{\frac{1}{2}L} \frac{1}{A(x)} dx = \frac{\frac{1}{2}L - c}{wh}$$

Finally, the relative resistance change for a straight channel can be evaluated by:

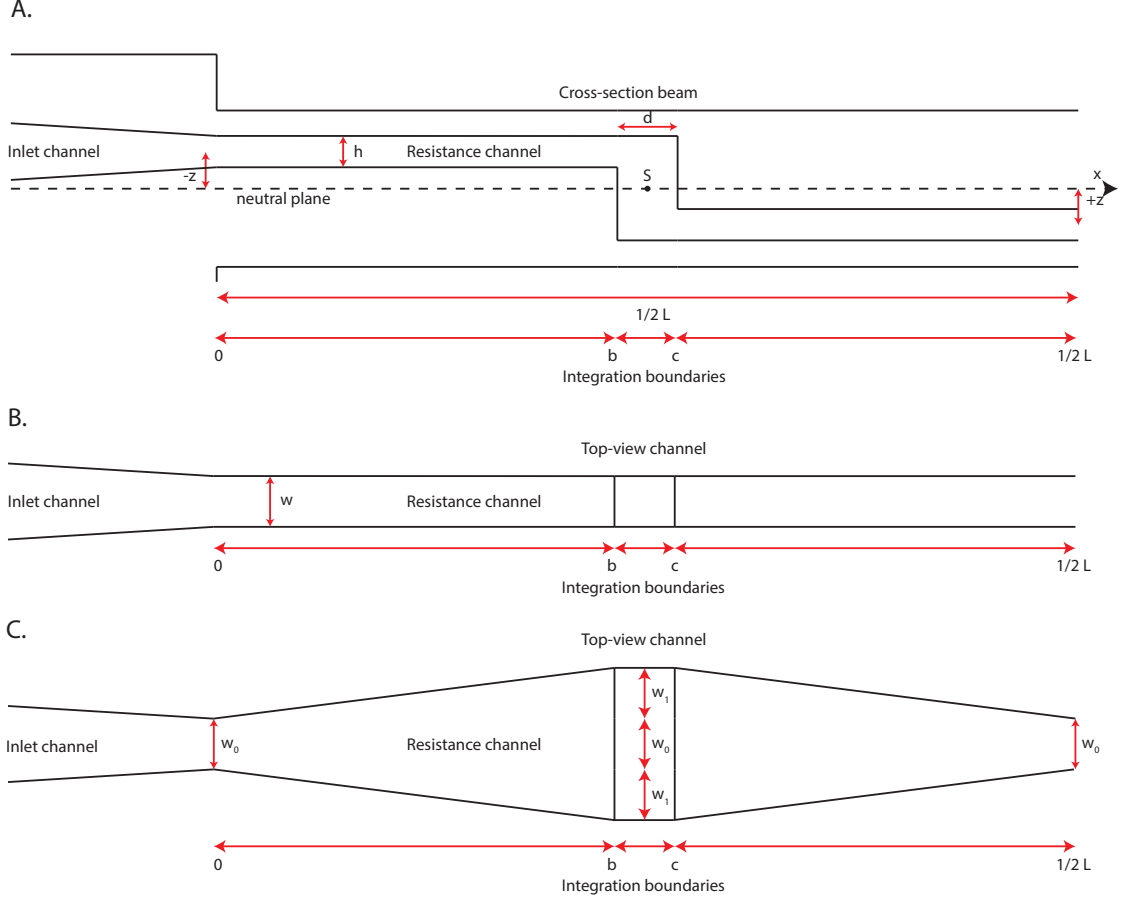


Figure E.4: Different views of the channel. The upper image views the channel from the side. The other two images contain a topview of the straight and tapered version of the channel.

$$\frac{\Delta R}{R} = \frac{\frac{z(1+2\nu)F_N}{48whEI} (6bL - 12b^2 - 12c^2 + 6cL)}{\frac{b+\frac{1}{2}L-c}{wh} + \frac{2z+h}{w(c-b)}} \quad (\text{E.8})$$

Doing the same for a tapered channel is slightly more complicated, but the solution can be found algebraically:

$$\frac{dR}{R} = \frac{\frac{z(1+2\nu)F_N}{48EI} (M(x) - N(x))}{O(x) + P(x) + Q(x)} \quad (\text{E.9})$$

Where:

$$\begin{aligned} M(x) &= \int_0^b \frac{\epsilon(x)}{A(x)} dx = \int_0^b \frac{\frac{F_N}{48EI} (6l - 24x)}{h(w_0 + (\frac{2w_1}{b})x)} dx \\ &= \frac{F_N}{48EI} \left[\frac{6((\frac{2w_1}{b})L + 4w_0) \log((\frac{2w_1}{b})x + w_0) - 4(\frac{2w_1}{b})x}{h(\frac{2w_1}{b})^2} \right]_0^b \end{aligned}$$

$$\begin{aligned}
N(x) &= \int_c^{\frac{1}{2}L} \frac{\epsilon(x)}{A(x)} dx = \int_c^{\frac{1}{2}L} \frac{\frac{F_N}{48EI} (6l - 24x)}{h((2w_1 + w_0) - (\frac{2w_1}{\frac{1}{2}L-c})(x - c))} dx \\
&= \frac{F_N}{48EI} \left[\frac{6((4c(\frac{2w_1}{\frac{1}{2}L-c}) + 4(2w_1 + w_0) - L(\frac{2w_1}{\frac{1}{2}L-c})) \log(c(\frac{2w_1}{\frac{1}{2}L-c}) + (2w_1 + w_0) - (\frac{2w_1}{\frac{1}{2}L-c})x) + 4(\frac{2w_1}{\frac{1}{2}L-c})x)}{h(\frac{2w_1}{\frac{1}{2}L-c})^2} \right]_{\frac{1}{2}L}^c
\end{aligned}$$

$$O(x) = \int_0^b \frac{1}{A(x)} dx = \int_0^b \frac{1}{h(w_0 + (\frac{2w_1}{b})x)} dx = \left[\frac{\log(h((\frac{2w_1}{b})x + w_0))}{h(\frac{2w_1}{b})} \right]_0^b$$

$$P(x) = \int_{-z-\frac{1}{2}h}^{z+\frac{1}{2}h} \frac{1}{(w_0 + 2w_1)(c - b)} dz = \frac{2z + h}{(w_0 + 2w_1)(c - b)}$$

$$\begin{aligned}
Q(x) &= \int_c^{\frac{1}{2}L} \frac{1}{A(x)} dx = \int_c^{\frac{1}{2}L} \frac{1}{h((2w_1 + w_0) - (\frac{2w_1}{\frac{1}{2}L-c})(x - c))} dx \\
&= \left[\frac{-\log(h(c(\frac{2w_1}{\frac{1}{2}L-c}) + (2w_1 + w_0) - (\frac{2w_1}{\frac{1}{2}L-c})x))}{h(\frac{2w_1}{\frac{1}{2}L-c})} \right]_{\frac{1}{2}L}^c
\end{aligned}$$

Implementing $M(x)$, $N(x)$, $O(x)$, $P(x)$ and $Q(x)$ in E.9 leads to a very obscure relation, so this is omitted. An implementation of both a straight and a tapered channel is found in the Matlab code. Figure E.5 shows the outcome of the modeling. Using tapered channels instead of straight ones is expected to yield an improvement in sensitivity of about 18%.

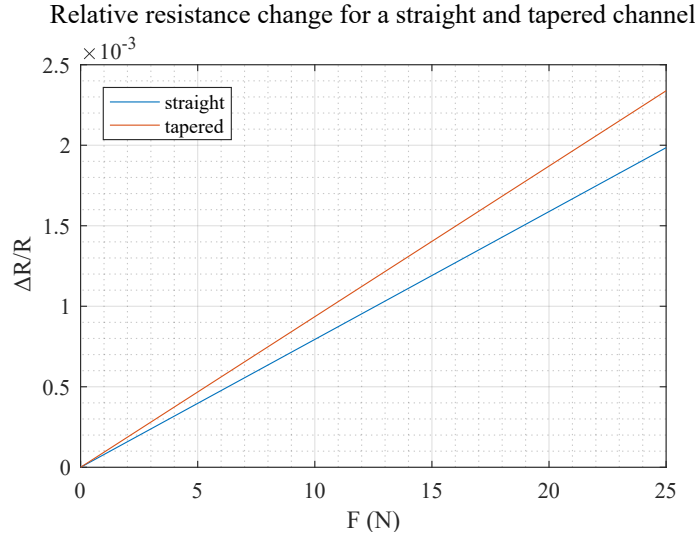


Figure E.5: The relative change in resistance $\frac{\Delta R}{R}$ as a function of force $F(N)$ for a straight and tapered channel.

```

1 %%%%%%%%%%%%%%%%%%%%%%%%%%%%%%%%%%%%%%%%%%%%%%%%%%%%%%%%%%%%%%%%%%%%%%%%%
2 %   Embedded strain sensor beam crossing neutral line ...
3 %   3D Printing Project ...
4 %   Marcel Welleweerd 18-10-16 ...
5 %%%%%%%%%%%%%%%%%%%%%%%%%%%%%%%%%%%%%%%%%%%%%%%%%%%%%%%%%%%%%%%%%%%%%%%%%
6
7 close all;
8 clear all;
9 clc
10
11 %_Parameters_-----
12 res = 1000;           % Resolution calculations
13 max_W = 25;          % [N] Load in middle beam
14 l = 10e-3;           % [m] Length total beam
15 h_b = 1260e-6;       % [m] Thickness beam
16 w_b = 25.35e-3;      % [m] Width beam
17 I = (w_b*h_b^3)/12;  % [m^4] Moment of inertia beam
18 E= 1.463e+09;        % [Pa] Modulus of Elasticity
19 z=0.450e-3;          % [m] Distance channels from neutral plane
20 mu=0.35;             % Poisson ratio material
21 ro = 0.3e-3;         % [Ohm cm] Resistivity strain material
22 h_ch=160e-6;         % [m] Height channel
23 w_ch=512e-6;         % [m] Width channel
24 w_0=w_ch;            %start width for tapered channel
25 w_1=w_ch;            %final width tapered channel (w_0+2w_1)
26 A=h_ch*w_ch;         % [m^2] Surface area channel
27 b=1/4*l-0.5*w_ch;    % [m] x-position start channel crossing
28 %the neutral plane
29 c=1/4*l+0.5*w_ch;    % [m] x-position end channel crossing the ...
    neutral plane
30 R=ro*((1/2*l-(c-b))/A + (z+h_ch)/(w_ch*(c-b))); % [ohm] estimated ...
    resistance
31 %of the channel
32
33 %_Defining ...
    variables_-----
34 x=zeros(1,res+1);    % [m] x-position on beam
35 w=zeros(max_W+1,res+1); % [m] z-deflection beam
36 dwdx=zeros(max_W+1,res+1); % [m/m] first derivative of deflection ...
    to x
37 ddwdx=zeros(max_W+1,res+1); % [m/m^2] second derivative of ...
    deflection to x
38 strain=zeros(max_W+1,res+1); % [] Strain in beam
39 av_strain=zeros(1,max_W+1); % [] Average strain over total channel
40 Rel_Res_str=zeros(1,max_W+1); % [] Relative resistance change over total
    %length beam straight
42 Rel_Res_tap=zeros(1,max_W+1); % [] Relative resistance change over total
    %length beam tapered
43
44
45
46 % R=ro*(l/A);        % [Ohm] Estimated resistance of unstrained ...
    channel
47
48

```

```

49 %_Calculations-----
50 for W=0:max_W % Counter to cycle through ...
    different loads
51 for i=1:(res+1) % Counter to calculate deflections etc.
52 % Use deflection formulae to calculate the deflection, its
53 % derivatives and the strain
54 x(1,i)=(i-1)/res)*0.5*1;
55 w(W+1,i)=-((W*x(1,i)^2)/(48*E*I))*(3*1-4*x(1,i));
56 dwdx(W+1,i) = ...
    ((2*W*x(1,i))/(48*E*I))*(3*1-4*x(1,i))+((W*x(1,i)^2)...
    / (48*E*I))*(3*1-4);
57 dwdx(W+1,i) = ((2*W)/(48*E*I))*(3*1-4*x(1,i))+((2*W*x(1,i))/...
    (48*E*I))*(3*1-4)+((2*W*x(1,i))/(48*E*I))*(3*1-4);
58 strain(W+1,i)=z*ddwdx(W+1,i);
59 end
60 % Average strain over the channel
61 av_strain(1,W+1)=sum(abs(strain(W+1,:)))/(res+1);
62 % Calculate the relative resistance change straight channel
63 Rel_Res_str(1,W+1) = ...
64 ((z*(1+2*mu)*W)/(48*w_ch*h_ch*E*I)*(6*b*1-12*b^2-12*c^2+6*c*1))...
65 /((b+0.5*1-c)/(w_ch*h_ch)+(2*z+h_ch)/(w_ch*(c-b)));
66
67 %Calculate the relative resistance change tapered channel
68 temp = (2*w_1)/b;
69 nom1 = (6*((temp*1+4*w_0)*log(temp*b+w_0)-4*temp*b))/(h_ch*temp^2);
70 nom2 = (6*((temp*1+4*w_0)*log(temp*0+w_0)-4*temp*0))/(h_ch*temp^2);
71 temp = 2*w_1+w_0;
72 temp2 = (2*w_1)/((1/2)*1-c);
73 nom3 = ...
74 ((6*((4*c*temp2+4*temp-1*temp2)*log(c*temp2+temp-temp2*(1/2)*1)...
75 +4*temp2*(1/2)*1))/(h_ch*temp2^2);
76 nom4 = (6*((4*c*temp2+4*temp-1*temp2)*log(c*temp2+temp-temp2*c)...
77 +4*temp2*c))/(h_ch*temp2^2);
78 temp = (2*w_1)/b;
79 den1 = (log(h_ch*(temp*b+w_0)))/(h_ch*temp)
80 den2 = (log(h_ch*(temp*0+w_0)))/(h_ch*temp)
81 temp = 2*w_1+w_0;
82 temp2 = (2*w_1)/((1/2)*1-c);
83 den3 = (2*z+h_ch)/(temp*(c-b))
84 den4 = (-log(h_ch*(c*temp2+temp-temp2*(1/2)*1)))/(h_ch*temp2)
85 den5 = (-log(h_ch*(c*temp2+temp-temp2*c)))/(h_ch*temp2)
86 Rel_Res_tap(1,W+1) = ((z*(1+2*mu)*W)/(48*E*I)*((nom1-nom2)-...
87 (nom3-nom4)))/((den1-den2)+den3+(den4-den5));
88 end
89
90 improve = Rel_Res_tap(1,max_W)/Rel_Res_str(1,max_W);
91
92
93
94 to_plot = zeros(size(w,1),size(w,2),4);
95 for i=1:size(w,1)
96 to_plot(i,:,1) = x(1,:);
97 to_plot(i,:,3) = w(i,:);
98 to_plot(i,:,2) = NaN;
99 to_plot(i,:,4) = NaN;
100 end
101
102 file3 = strcat('Deflection clamped-clamped beam');
103 names = {'Deflection beam as function of x-position (F = 1:25 N)' ...

```

```

104     'x (m)' 'Deflection (m)'};
105 ploterrbar(names, to_plot, [], [], [], 1, '-', file3)
106
107 to_plot = zeros(size(w,1),size(w,2),4);
108 for i=1:size(w,1)
109     to_plot(i,:,1) = x(1,:);
110     to_plot(i,:,3) = strain(i,:);
111     to_plot(i,:,2) = NaN;
112     to_plot(i,:,4) = NaN;
113 end
114
115 file3 = strcat('Strain clamped-clamped beam');
116 names = {'Strain as function of x-position (F = 1:25 N)' 'x (m)' ...
          'Strain'};
117 ploterrbar(names, to_plot, [], [], [], 1, '-', file3)
118
119 to_plot = zeros(2,size(Rel_Res_tap,2),4);
120 to_plot(1,:,1) = 0:max_W;
121 to_plot(1,:,3) = Rel_Res_str(1,:);
122 to_plot(1,:,2) = NaN;
123 to_plot(1,:,4) = NaN;
124
125 to_plot(2,:,1) = 0:max_W;
126 to_plot(2,:,3) = Rel_Res_tap(1,:);
127 to_plot(2,:,2) = NaN;
128 to_plot(2,:,4) = NaN;
129
130 file3 = ...
131 strcat('Relative resistance change for a straight and tapered channel');
132 names = ...
133 {'Relative resistance change for a straight and tapered channel' ...
134  'F (N)' 'dR/R'};
135 labels = {'straight' 'tapered'}
136 ploterrbar(names, to_plot, labels, [], [], 1, '-', file3)

```

Appendix F

Linear deflection with channels included

In Appendix E, it was shown that the deflection in the middle of a doubly clamped beam is defined as:

$$x = F_N \frac{\frac{1}{4}L^3}{48EI} \quad (\text{F.1})$$

This equation can be regarded as a linear spring which relates the force F and the deflection x via a spring constant. A way to integrate the incorporated channels in this relation is to model the beam as a series of parallel springs. The material on both sides of the channel is modeled as two beams in parallel, each with its own moment of inertia. The channels alternate with solid beams, which also have their own moment of inertia. The new spring constant is the sum of all separate constants. This situation is shown in Figure F.1 and leads to the following equation:

$$\frac{F_N}{x} = k_{\text{spring}} = 2 \frac{48EI_1}{\frac{1}{4}L^3} + (n-1) \frac{48EI_2}{\frac{1}{4}L^3} + n \frac{48E(I_3 + I_4)}{\frac{1}{4}L^3} \quad (\text{F.2})$$

In this equation, n is the amount of channels in the beam. If the origin is chosen in the middle of the beam, the four moments of inertia can be expressed as:

$$\begin{aligned} I_1 &= \frac{d_1 h}{12} \\ I_2 &= \frac{d_2 h}{12} \\ I_3 &= \frac{1}{3} d_3 \left(\left(\frac{h}{2} \right)^3 - \left(\frac{h}{2} - h_2 \right)^3 \right) \\ I_4 &= \frac{1}{3} d_4 \left(\left(\frac{h}{2} \right)^3 - \left(\frac{h}{2} - h_1 \right)^3 \right) \end{aligned}$$

The result of this modeling is used in the discussion of the deflection curves acquired by loading and unloading the fabricated beams.

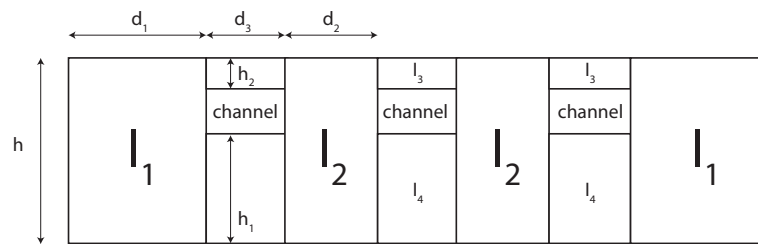


Figure F.1: The beam schematically as parallel subsections of smaller solid beams.

Appendix G

Nonlinear deflection of a clamped clamped beam

The linear approximation of the clamped-clamped beam assumes that the deflection is sufficiently low to neglect the increase in length of the beam and thus the axial strains in the beam. In reality however, the further a clamped-clamped beam is bent, the more significant is the axial strain energy. This effect stiffens the beam as the beam deflects more and causes a nonlinear load-deflection response.

Senturia solves this problems by using the Principle of Virtual Work [67]. He starts by using an exact solution for small deflections:

$$w(x) = \frac{c}{2} \left(1 + \cos \frac{2\pi x}{L}\right) \quad (\text{G.1})$$

In the energy function the self-generated axial strain due to stretching of the neutral axis is added. The axial strain is found by:

$$\epsilon_{\text{axial}} = \frac{1}{2} \frac{1}{L} \int_{-\frac{L}{2}}^{\frac{L}{2}} \left(\frac{dw}{dy}\right)^2 dx \quad (\text{G.2})$$

Now, the total strain in the beam becomes:

$$\epsilon_{\text{total}} = \epsilon_{\text{bend}} + \epsilon_{\text{axial}} = -z \frac{d^2 w(x)}{dx^2} + \frac{1}{2} \frac{1}{L} \int_{-\frac{L}{2}}^{\frac{L}{2}} \left(\frac{dw}{dy}\right)^2 dx \quad (\text{G.3})$$

And the total strain energy can be found from:

$$W = \frac{Ew}{2} \int_{-\frac{h}{2}}^{\frac{h}{2}} \int_{-\frac{L}{2}}^{\frac{L}{2}} \epsilon_{\text{total}}^2 dx dz \quad (\text{G.4})$$

The work done by the applied load is simply the load times the deflection, Fc , so that after the integrals are being performed, the total potential energy is found to be:

$$U = \frac{Ewh^3\pi^4(8h^2 + 3c^2)c^2}{96L^3} - F_N c \quad (\text{G.5})$$

Using this equation, the value of c that minimizes the potential energy U should be found. This can be done by taking the derivative of U with respect to c and setting the result

to 0. This leads to a relation which expresses the force as a function of the displacement c in the middle of the beam:

$$F_N = \frac{\pi^4 Ewh^3}{6 L^3}c + \frac{\pi^4 Ewh}{8 L^3}c^3 \quad (\text{G.6})$$

The result is a force which partly depends on linear bending term (left) and a nonlinear stretching term (right). The higher the deflection, the more important the right hand part gets. This result is not unexpected and is an example of an amplitude stiffened Duffing spring. The two parts of the function can each be broken down to three components: a numerical constant, a term that depends on material properties and dimensions of the beam and a dependency on the deflection c . These numerical constants are not accurate since the trial solution used is too simple. There are several possibilities to obtain more precise numerical constants. One approach is to repeat the before mentioned solution with more complex trial solutions but this becomes complex because the number of terms in the trial solution grows. An alternative is to use the functional form of the force displacement solution and find better values for the constants in each term. The functional form of the function looks like:

$$F_N = C_b \frac{Ewh^3}{L^3}c + C_s \frac{Ewh}{L^3}c^3 \quad (\text{G.7})$$

Since measurements had already been done, it was decided to find C_b and C_s by fitting the functional form in the measured load-deflection curve. The final graph resulting from fitting the C_b and C_s numerical constants, and substituting the material and dimensional parameters, $E = 1.463$ GPa, $w = 25.35$ mm, $h = 860$ μm , $L = 10$ mm is shown in Figure G.1.

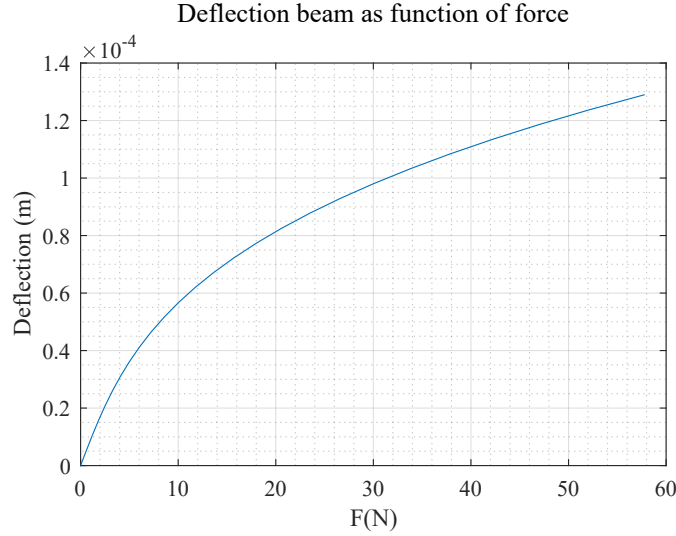


Figure G.1: The nonlinear deflection as a function of force.

To find the axial strain in the beam and compare this with the bending strains present in the beam, Equation G.7 has been written in an alternative form in which the displacement of the centre of the beam is expressed as a function of the applied load:

$$c = f(F_N) = \frac{\sqrt[3]{\sqrt{3}\sqrt{4A^3B^3 + 27B^4F_N^2} + 9B^2F_N}}{\sqrt[3]{23^{\frac{2}{3}}B}} - \frac{\sqrt[3]{\frac{2}{3}A}}{\sqrt[3]{\sqrt{3}\sqrt{4A^3B^3 + 27B^4F_N^2} + 9B^2F_N}} \quad (\text{G.8})$$

With:

$$A = C_b \frac{Ewh^3}{L^3}$$

$$B = C_s \frac{Ewh}{L^3}$$

The result of this has been combined with the shape function used in the linear approximation of the clamped-clamped beam displacement:

$$w(x) = \frac{f(F_N)}{\frac{1}{4}L^3} x^2(3L - 4x)$$

Now, for each force, the axial strain can be calculated using G.3. Also, the bending strain can be calculated using the same relations as found in Appendix E. Both trends have been plotted in Figure G.2. From this calculation it seems that although beam stiffening plays a role in bending the beam, it should not play a mayor role in the signals generated by the changes in resistance as the bending strain is even at relatively high loads of 25 N an order of magnitude smaller than the maximum bending strain in the beam.

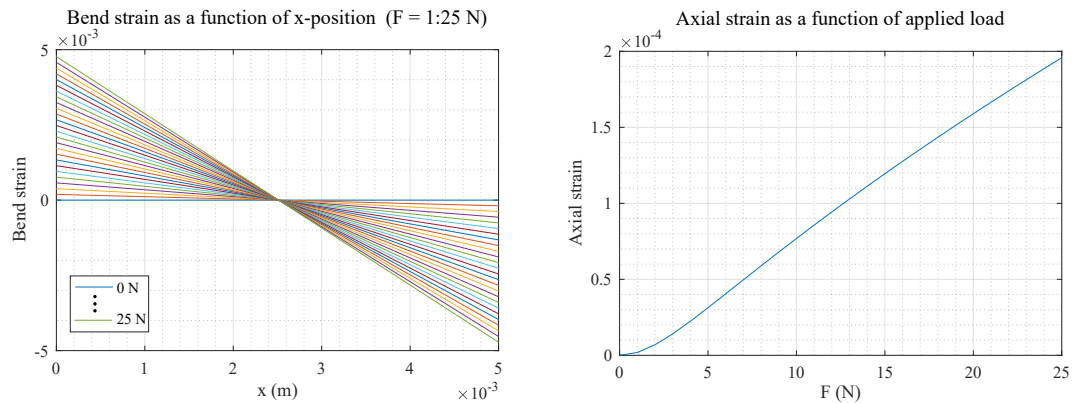


Figure G.2: The strain due to bending of the membrane at a distance $z = 300 \mu\text{m}$ from the neutral plane (left) and the axial strain (right).

```

1 close all;
2 clear all;
3 clc
4
5 %_Parameters-----
6
7 max_W = 25;           % [N] Load in middle beam
8 l = 10e-3;           % [m] Length total beam
9 h_b = 600e-6;        % [m] Thickness beam
10 w_b = 25.35e-3;      % [m] Width beam
11 I = (w_b*h_b^3)/12;  % [m^4] Moment of inertia beam
12 E= 1.463e+09;        % [Pa] Modulus of Elasticity
13 mu=0.35;            % Poisson ratio material
14 A=h_b*w_b;           % [m^2] Surface area channel
15 z=0.180e-3;         % [m] Distance from neutral plane to calculate bend
16 %strain
17
18 %_Defining ...
19     variables-----
20 res = 10;            % Resolution calculation force deflection graph
21 res2 = 500;
22 w=zeros(1,res+1);
23 w2=zeros(max_W+1,res2+1);
24 f=zeros(1,res+1);
25 x=zeros(1,res+1);
26 axialStrain = zeros(max_W+1,1);
27 ddwdx = zeros(max_W+1,res2+1);
28 bendStrain = zeros(max_W+1,res2+1);
29 totalStrain = zeros(max_W+1,res2+1);
30
31 %Fit parameters retrieved from measurement data
32 fit_par1 = 6.677e+04;
33 fit_par2 = 2.488e+13;
34 %find constants Cb and Cs with that
35 Cb = fit_par1/((E*w_b*h_b^3)/l^3);
36 Cs = fit_par2/((E*w_b*h_b)/(l^3));
37
38 %_Calculations-----
39     % Counter to cycle through different loads
40     for i=1:max_W+1           % Counter to calculate deflections etc.
41         %calculate a force deflection curve for deflection is 0 to
42         % (3/10) (1/2) * h_b
43         w(1,i) = ((i-1)/(max_W)) * (3/10) * (1/2) * h_b;
44         f(1,i) = Cb * ((E*w_b*h_b^3)/l^3) * w(1,i) + Cs * ((E*w_b*h_b)/(l^3)) * w(1,i)^3;
45
46         %Calculate the constants to be used in deflection as function ...
47         % of x
48         %and strain calculations
49         W=i-1;
50         A=Cb * ((E*w_b*h_b^3)/l^3);
51         B=Cs * ((E*w_b*h_b)/(l^3));
52         C = (((sqrt(3)*sqrt(4*A^3*B^3 + 27*B^4*W^2) + 9*B^2*W)^...
53             (1/3))/(2^(1/3)*3^(2/3)*B) - ((2/3)^(1/3)*A)/(sqrt(3)*...
54             sqrt(4*A^3*B^3 + 27*B^4*W^2) + 9*B^2*W)^(1/3)))/((1/4)*l^3));
55         for j=1:(res2+1)
56             x(1,j) = ((j-1)/res2) * (1/2) * l;
57             w2(i,j) = C*x(1,j)^2 * (3*l-4*x(1,j));

```

```

56         ddwdx(W+1, j) = ...
           ((2*W) / (48*E*I)) * (3*l-4*x(1, j)) + ((2*W*x(1, j)) / ...
57           (48*E*I)) * (3*l-4) + ((2*W*x(1, j)) / (48*E*I)) * (3*l-4);
58         bendStrain(i, j) = z*ddwdx(W+1, j);
59     end
60     axialStrain(i, 1) = (1/2) * (1 / ((1/2)*l)) * ((3*C^2*l^5) / 20);
61 end
62 %calculate total strain by adding axial and bendstrain
63 for i=1:max_W+1
64     totalStrain(i, :) = bendStrain(i, :) + axialStrain(i, 2);
65 end
66
67 %create relevant plots
68 to_plot = zeros(size(w2, 1), size(w2, 2), 4);
69 for i=1:size(w2, 1)
70     to_plot(i, :, 1) = x(1, :);
71     to_plot(i, :, 3) = w2(i, :);
72     to_plot(i, :, 2) = NaN;
73     to_plot(i, :, 4) = NaN;
74 end
75
76 file3 = strcat('Deflection clamped-clamped beam 1');
77 names = {'Deflection beam as function of x-position (F = 1:25 N)' ...
78         'F(N)' 'Deflection (m)'};
79 ploterrbar(names, to_plot, [], [], [], 0, '-', 0, file3)
80
81 to_plot = zeros(size(w, 1), size(w, 2), 4);
82 for i=1:size(w, 1)
83     to_plot(i, :, 1) = f(i, :);
84     to_plot(i, :, 3) = w(1, :);
85     to_plot(i, :, 2) = NaN;
86     to_plot(i, :, 4) = NaN;
87 end
88
89 file3 = strcat('Deflection clamped-clamped beam 2');
90 names = {'Deflection beam as function of force' 'F(N)' 'Deflection ...
91         (m)'};
92 ploterrbar(names, to_plot, [], [], [], 0, '-', 0, file3)
93
94 to_plot = zeros(size(w, 1), size(w, 2), 4);
95
96 for i=1:size(w, 1)
97     to_plot(i, :, 1) = 0:1:25;
98     to_plot(i, :, 3) = axialStrain(:, 1);
99     to_plot(i, :, 2) = NaN;
100    to_plot(i, :, 4) = NaN;
101 end
102
103 file3 = strcat('Axial strain as a function of applied load');
104 names = {'Axial strain as a function of applied load' 'F (N)' ...
105         'Axial strain'};
106 ploterrbar(names, to_plot, [], [], [], 0, '-', 0, file3)
107
108 to_plot = zeros(max_W+1, size(x, 2), 4);
109 for i=1:size(bendStrain, 1)
110     to_plot(i, :, 1) = x(1, :);
111     to_plot(i, :, 3) = bendStrain(i, :);
112     to_plot(i, :, 2) = NaN;

```

```
112     to_plot(i,:,4) = NaN;
113 end
114
115 file3 = strcat('Bend strain as a function of position2');
116 names = {'Bend strain as a function of x-position (F = 1:25 N)' 'x ...
(m)' ...
'Bend strain'};
117
118 ploterrbar(names, to_plot, [], [], [], 0, '-', 0, file3)
```

Appendix H

Interconnects

During the course of this research, the interconnects slowly evolved to the form they have now. This appendix describes the different forms the connections took, their advantages and disadvantages.

The very first try to interface silver glue and carbon glue with measurement equipment is shown in Figure I.1. In this setup, copper wires were hung in the fluidic inlets after infusion of the channel. For mechanical stability, cyano acrylate was used to connect the wire to the print. This method works well but has several disadvantages. One cannot perform a four wire measurement to exclude the contact resistances from the measurement nor can one retrieve any information about the magnitude of the contact resistances. A possible solution is of course to insert several wires in the fluidic inlets but this is far from ideal. Especially if the resistance over the course of a channel is to be investigated, like in section 5.3, a different solution is needed. An additional challenge in this is that cleaning the channel should remain possible while connections should be added on different locations along the channel. A possible solution is to add holes for the wires after the post-processing of the 3D print (Figure I.2). This was done by drilling holes at 3D printed indicators. After this, wires were added and the access holes were sealed using hot glue. This method was not successful as drilling holes in the 3D print caused the channels to be clogged. The next setup had printed access holes that could

be closed using hot glue (Figure H.1). The hot glue can easily be removed when it has to be. This allows removing the wax from the entire channel. When the wax is removed from the channel, the holes are opened up to remove the wax from there. Before the insertion, the copper wires were cleaned using acetone. Then they were put in the access holes, glued with two component glue (Bison combi rapide two component glue) and left to cure. When the glue was cured, the conductive liquid was infused using a syringe (BD plastipak 2.5 ml Luer) with a pipette tip (Eppendorf ep.T.I.P.S. Standard volume range 2 μ l–200 μ l). The pipette tips are adapted to fit on the syringe by cutting off the end. Also the tip is opened up (about 2 mm is cut off) to reduce the pressure loss and make a better fit with the chip inlets. There are two identical chips and half of the channels were filled with graphite paint and the other half with carbon glue.

The result of the fabrication of one of the chips is shown in Figure H.5. Several channels had problems with filling and were blocked especially when passing a wire inlet. Also, it was observed that some of the copper wires were not located at the center of the channel which lead to assymmetric filling of the void around the wire (Figure H.2). Also, after curing several air pockets were found at the interconnects in the channels filled

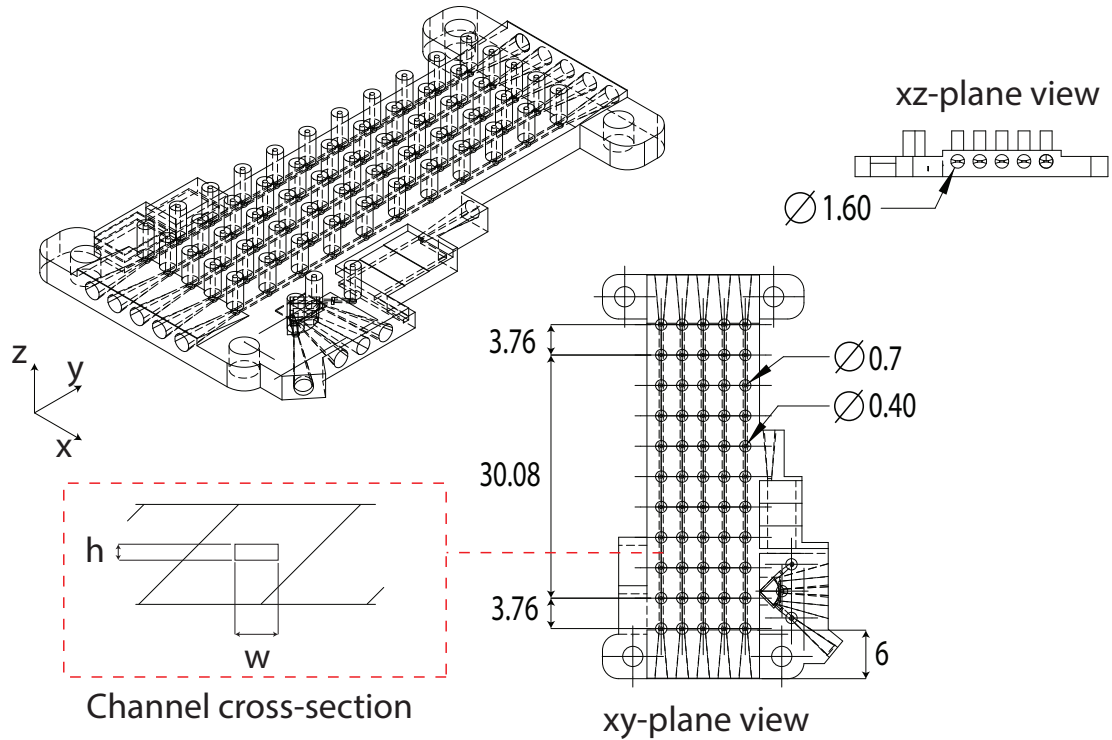


Figure H.1: Design for a fluidic chip with 3D printed holes for the wires. Channels have dimensions $w = 510 \mu\text{m}$ by $h = 160 \mu\text{m}$ and get wider at a wire inlet ($\varnothing 0.7 \text{ mm}$).

with carbon glue. For the graphite paint, it was not possible to see where the paint was located after drying.

Once the channels in the chip had cured for a week, 4-wire measurements are done over sections of the channel to determine the development of the resistance over distance (Figure H.4). This is done using a Keithley 2602 System Sourcemeter (Table H.1) which is connected to a computer running Labview. A current-sweep is performed such that the maximum current leads to a voltage of about 40 V, the maximum voltage the sourcemeter can handle. The current is swept from 0 to the maximum currents, to minus the maximum current, and then back to zero. This in order to see any hysteresis effects.

In Figure H.6 two current-voltage curves are shown which were measured over the entire length of the channel. The left graph shows a channel filled with graphite paint whereas the left graph shows a channel filled with carbon glue. It can be seen that the current-voltage curve is linear and does not depend on the direction of the current. By differentiating the line, the resistance of the channel can be obtained. This particular graphite paint channel has a resistance of about 205 k Ω . The one filled with carbon glue

Table H.1: Settings for the Keithley 2602 System SourceMeter

Source (range)	Current (1.000 00 mA)
Measure	Voltage
Limit	40 V
Speed	Hi-Accuracy
Filter	Average, Repeat, 5x



Figure H.2: Microscopic images of the channel filling process. The copper wires are not located in the middle of the channel. In the depicted situation the fluid goes around the left side first (left) while a moment later the right side follows (right).

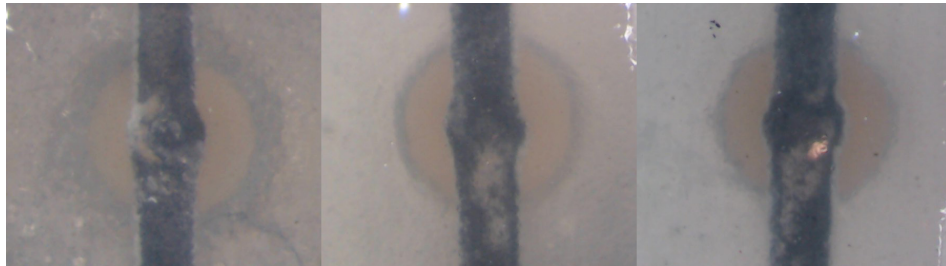


Figure H.3: It was discovered that in the channels filled with carbon glue several air pockets were visible around the interconnects.

has a resistance of about 560 k Ω . Other channels had very similar results. What they all had in common is that the produced resistance is far higher than expected.

The main cause for these high resistances is ascribed to the fact that the paint retracts in the wire inlets as is shown in Figure H.3). Another observation which less likely, but possibly underlies the high resistances is the inclusion of air bubbles due to the asymmetry at the wire inlets. Another problem of this setup is the amount of time it takes to assemble the chip and take measurements. The several steps needed to open and close the wire inlets contaminated some channels which caused them to be blocked. A more generic method was needed to make the assembling process faster, more precise, and increase the success rate in filling the channels and decrease the resulting channel resistances.

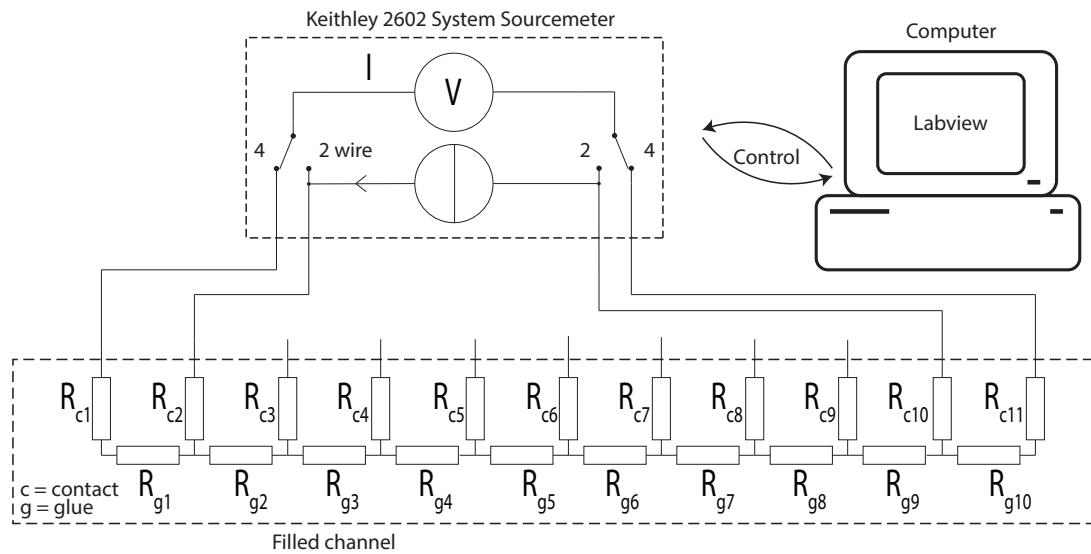


Figure H.4: Measurement setup which measures the resistance over a section of the filled channel.

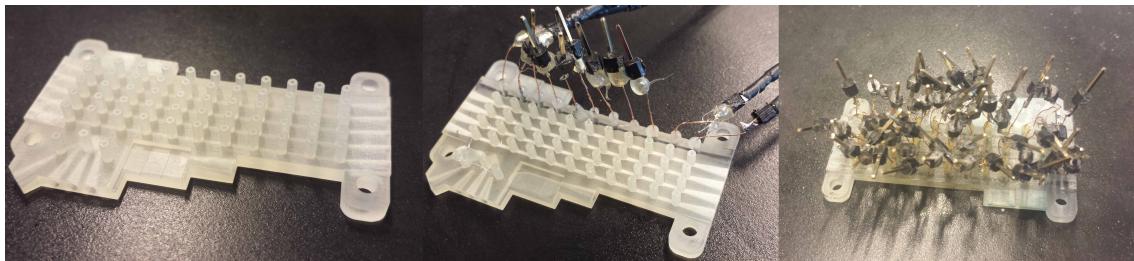


Figure H.5: Fluidic chip with 3D printed holes for the wires. The middle photo shows one assembled channel filled with graphite paint. The right photo shows a finished chip in which all wires are added and all channels are filled.

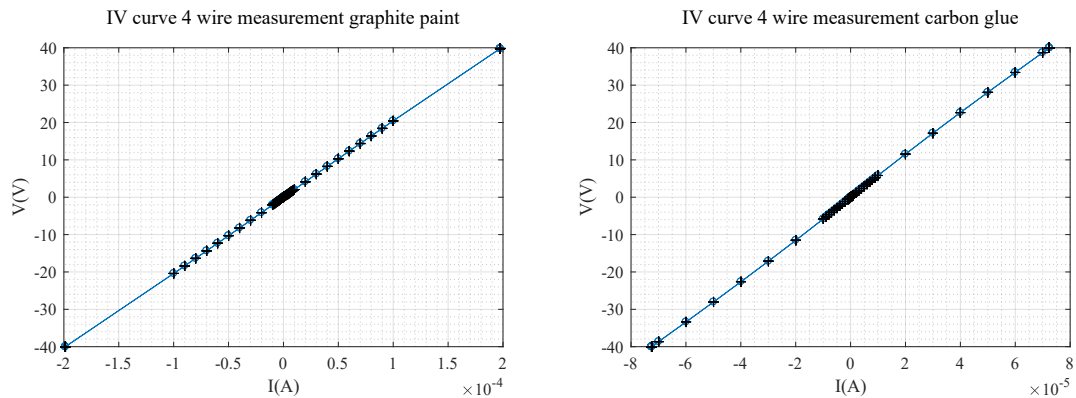


Figure H.6: IV curves of a channel filled with graphite paint (left) and carbon glue (right).

Appendix I

Photos fabricated chips and measurement setups

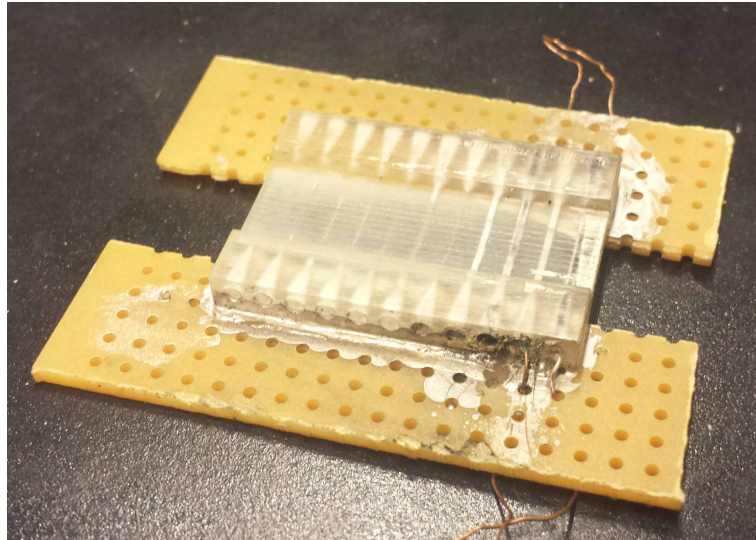


Figure I.1: The first interconnects were made by glueing the 3D print on a pcb with soldered copper wires. After the infusion the wires were inserted in the fluidic inlets and left to dry. For mechanical stability the wires were later also glued with cyano acrylate.

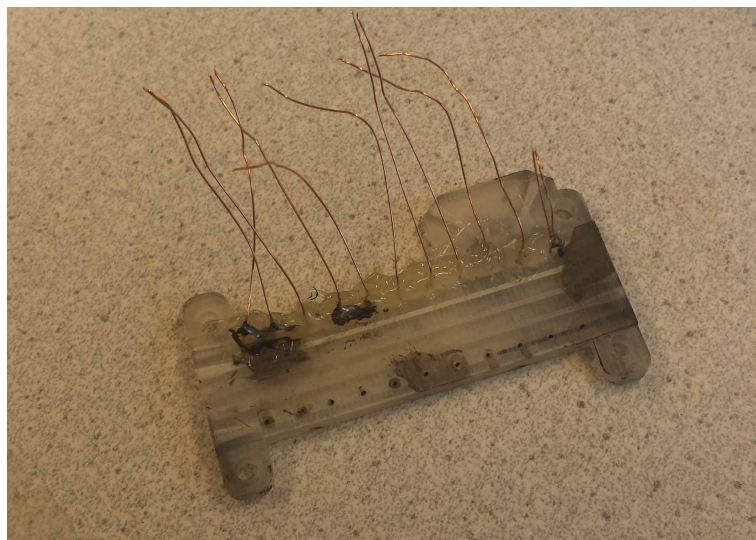


Figure I.2: Fluidic chip in which the post-processing was done before creating the access holes for the wiring.

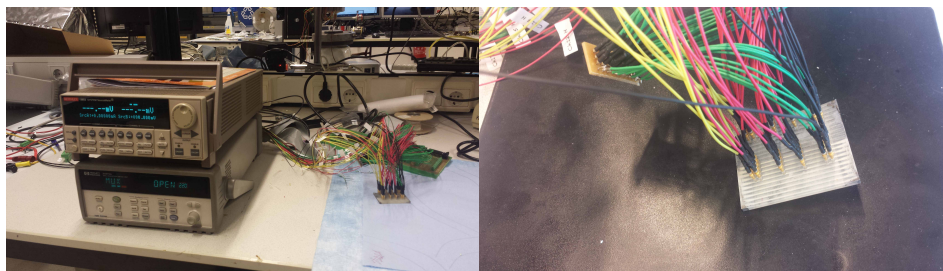


Figure I.3: Measurement setup to do a 4 and 2 wire measurement on all ten channels. The left shows an overview of the setup with the matrixboard and the source measurement unit. The right shows a close-up of all the channels with the wires to the matrixboard.

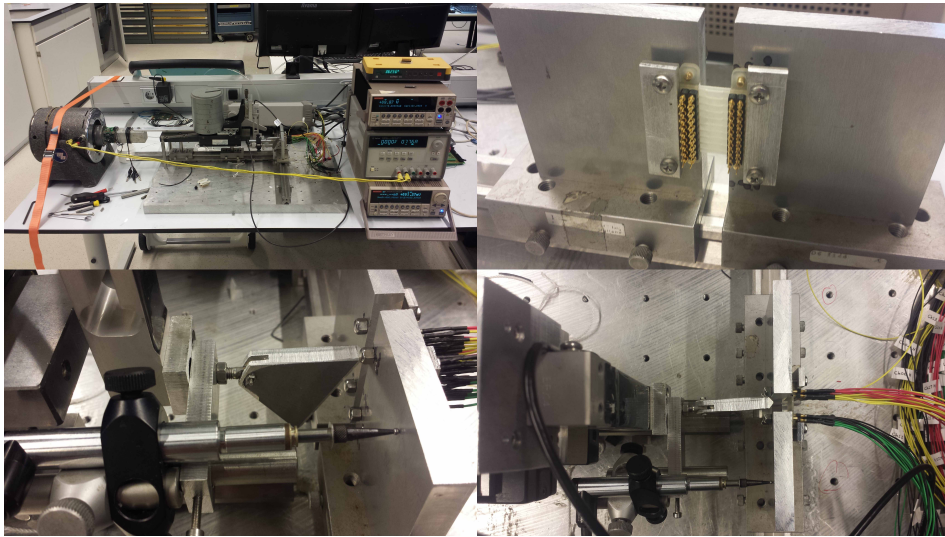


Figure I.4: Photos of the described measurement setup. The upper left photo shows an overview of the setup. The upper right photo shows the doubly clamped beam. The lower left photo shows the plunger, its hinge and the displacement sensor. The lower right photo shows the setup with sensor in place.

Appendix J

IV curve measurements

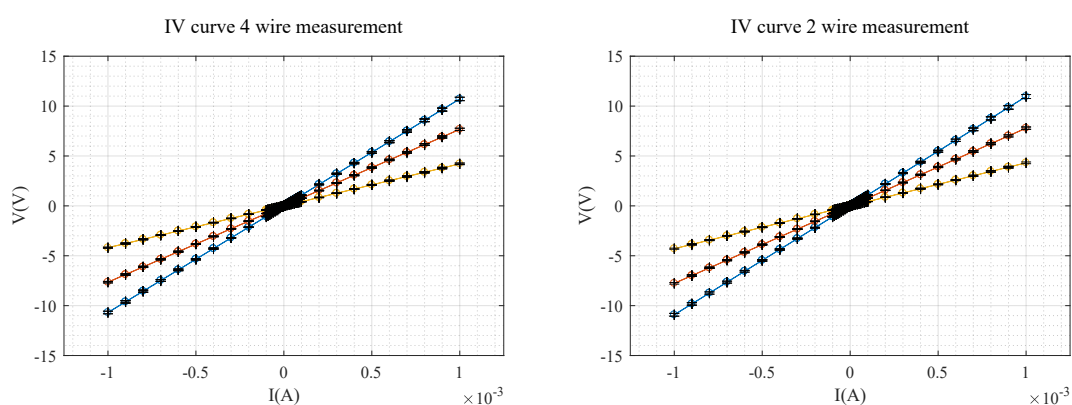


Figure J.1: IV channel 1 graphite paint

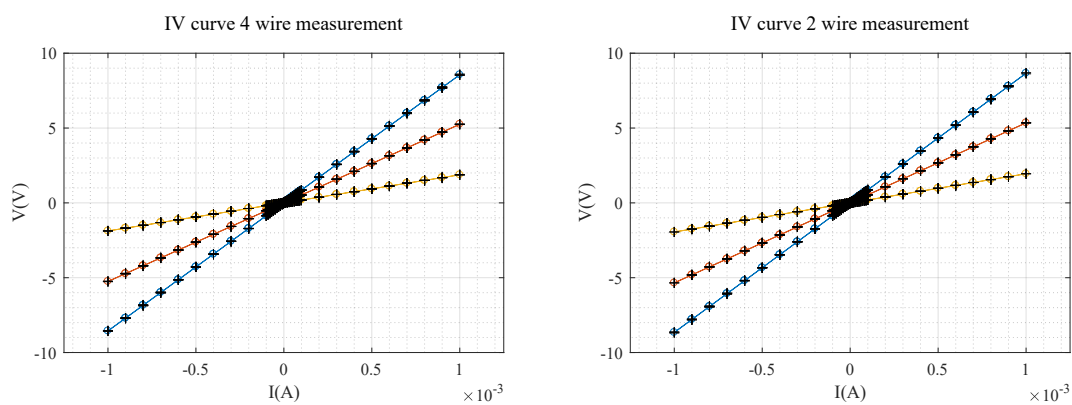


Figure J.2: IV channel 2 graphite paint

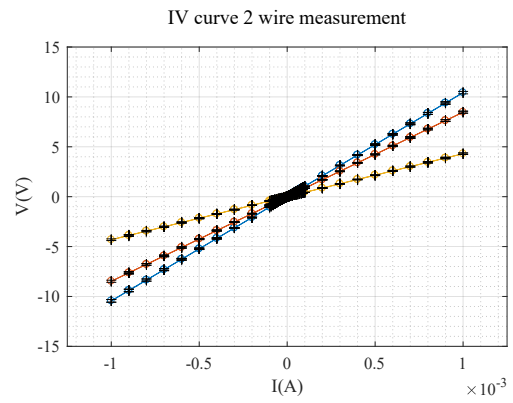
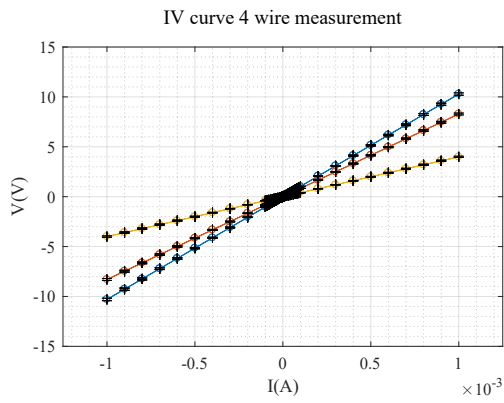


Figure J.3: IV channel 3 graphite paint

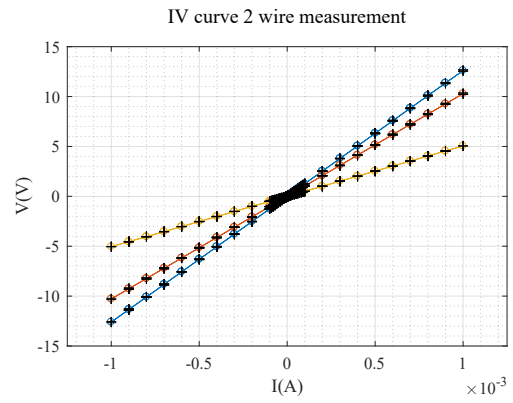
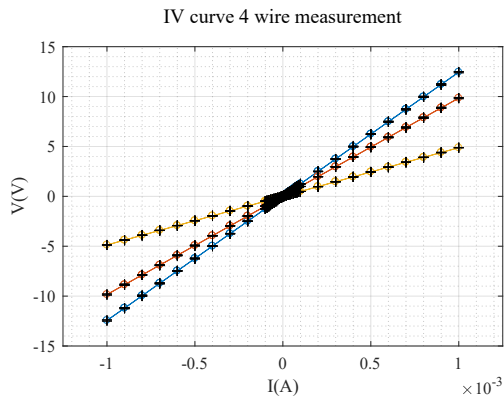


Figure J.4: IV channel 4 graphite paint

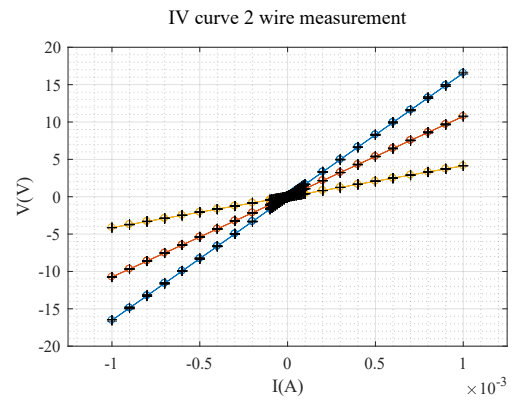
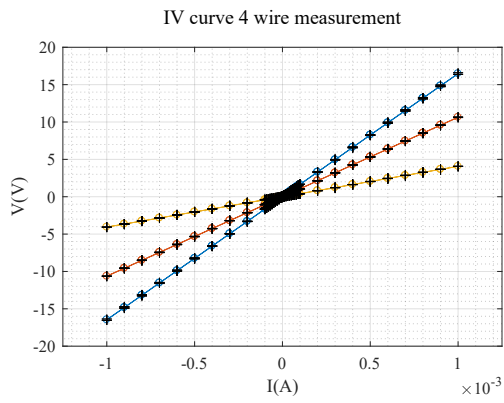


Figure J.5: IV channel 5 graphite paint

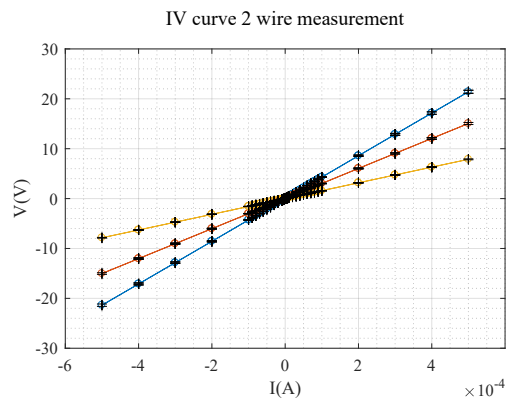
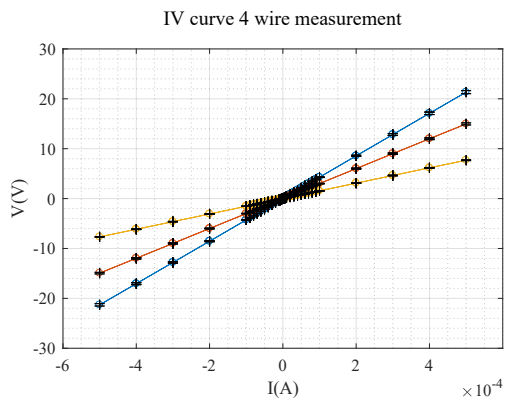


Figure J.6: IV channel 6 carbon glue

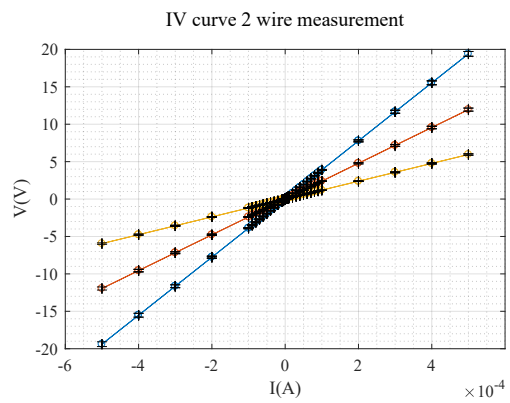
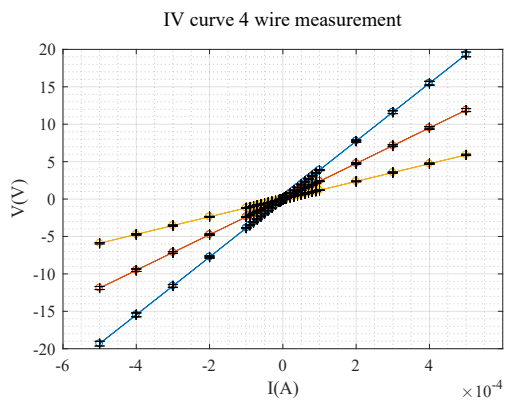


Figure J.7: IV channel 7 carbon glue

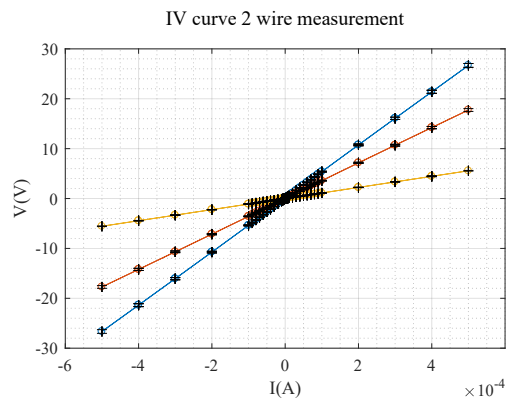
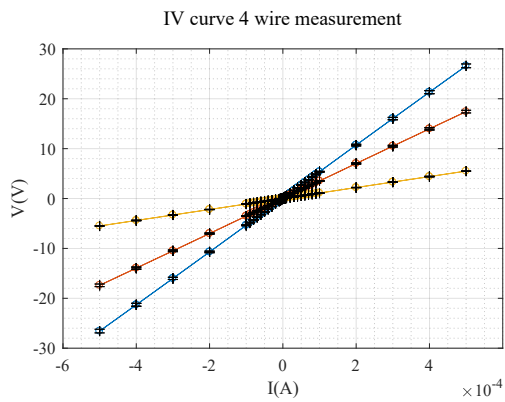


Figure J.8: IV channel 8 carbon glue

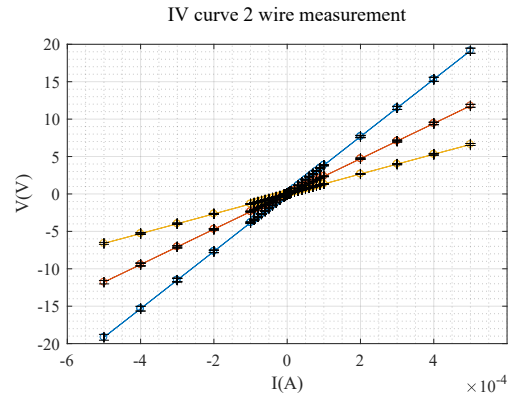
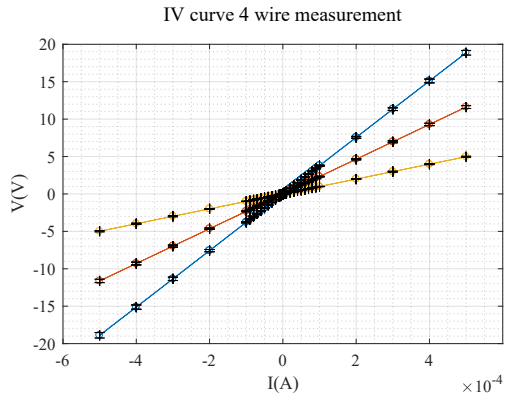


Figure J.9: IV channel 9 carbon glue

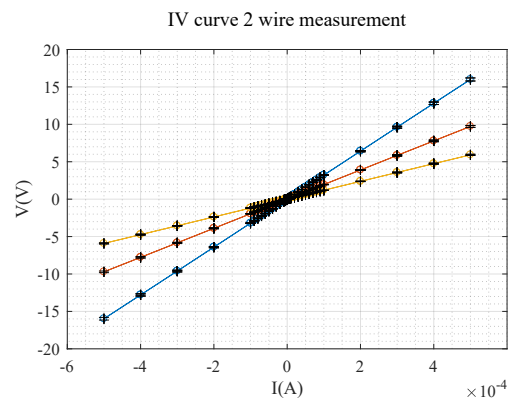
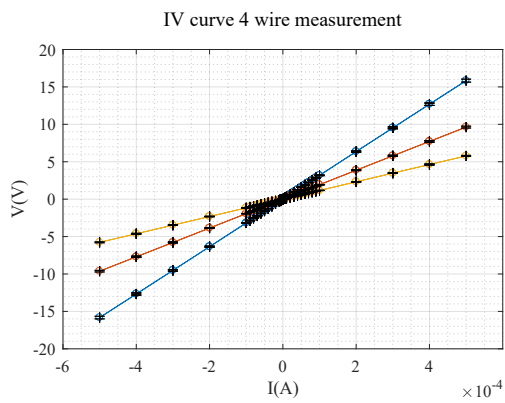


Figure J.10: IV channel 10 carbon glue

Appendix K

IV curve measurements 23 days after first measurement

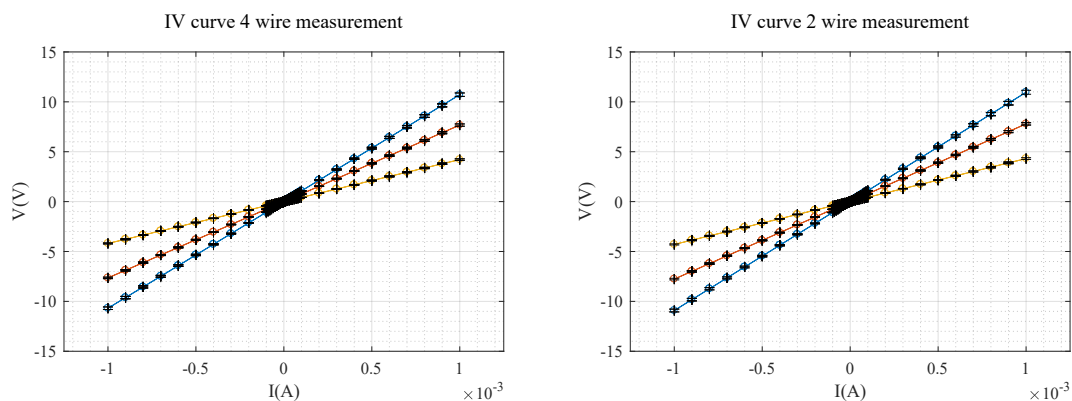


Figure K.1: IV channel 1 graphite paint

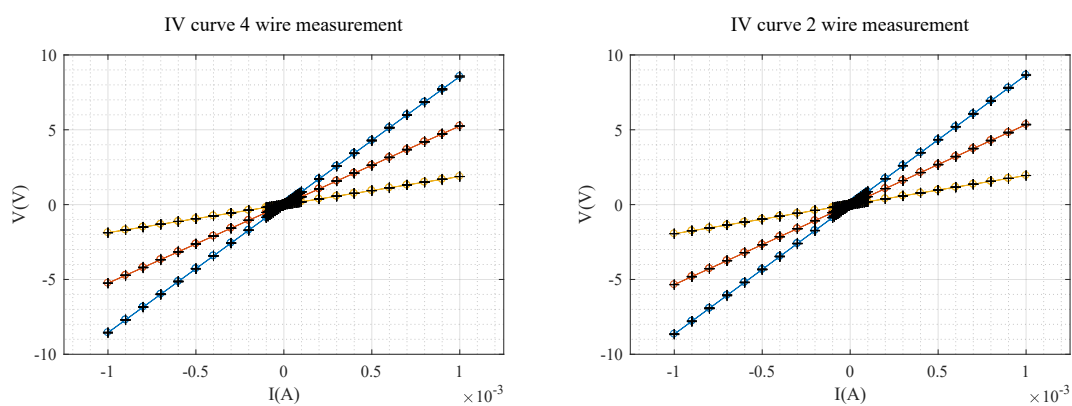


Figure K.2: IV channel 2 graphite paint

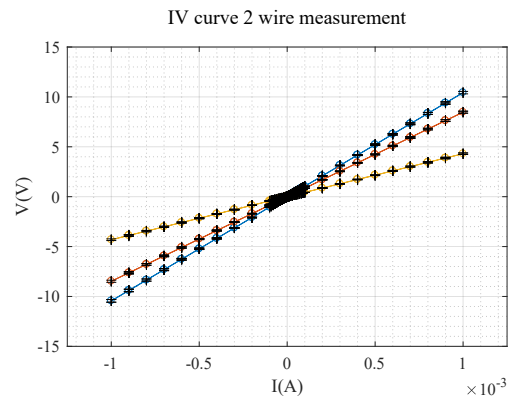
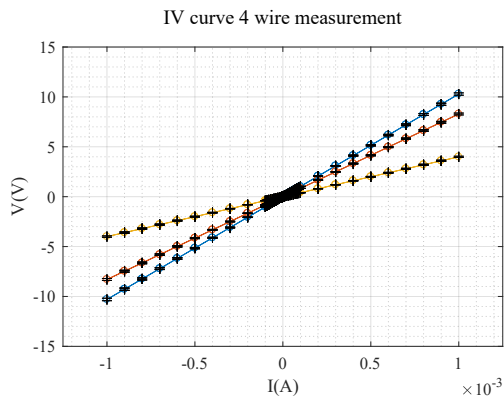


Figure K.3: IV channel 3 graphite paint

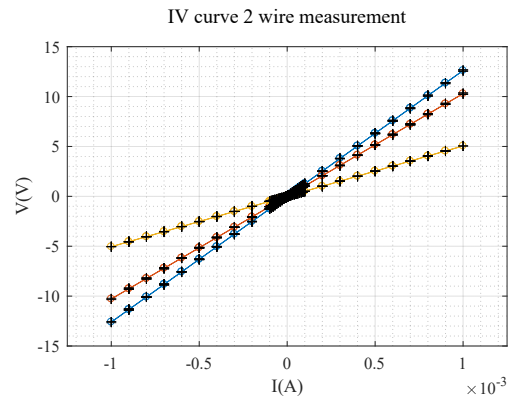
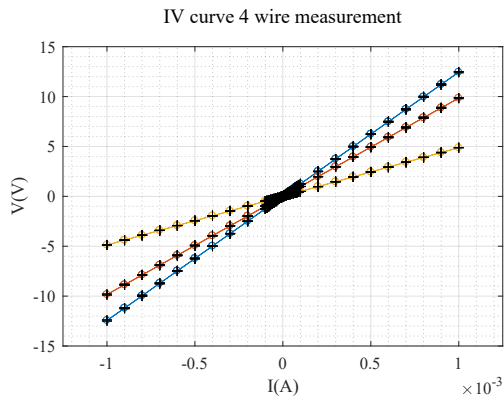


Figure K.4: IV channel 4 graphite paint

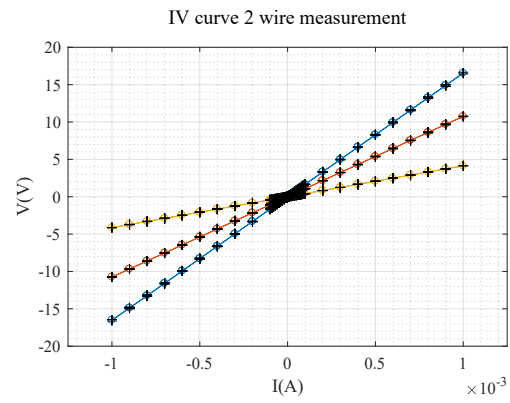
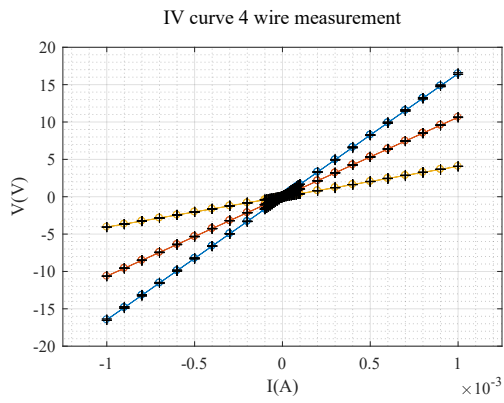


Figure K.5: IV channel 5 graphite paint

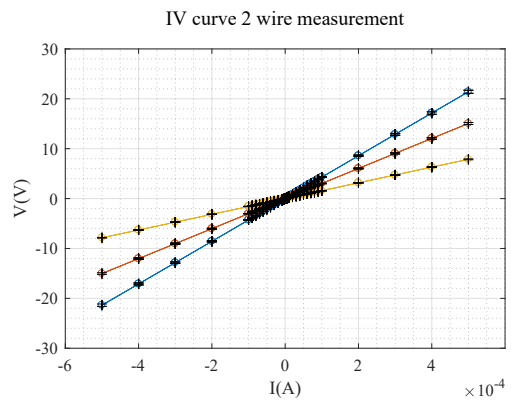
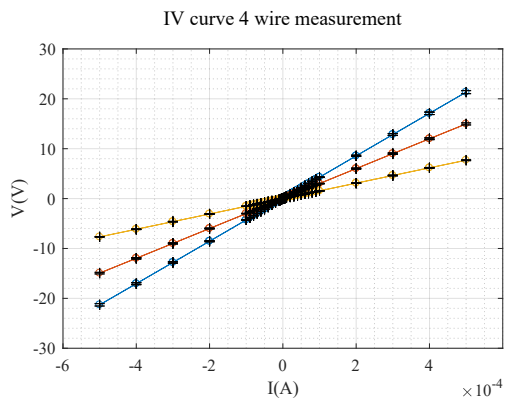


Figure K.6: IV channel 6 carbon glue

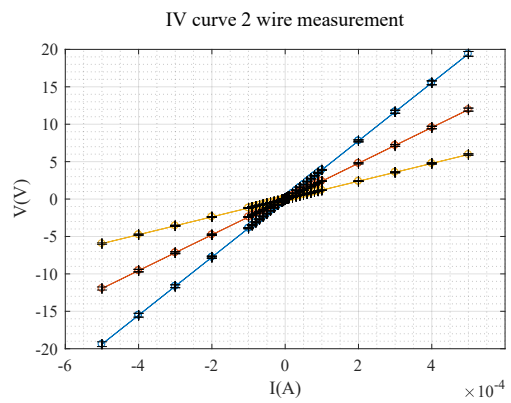
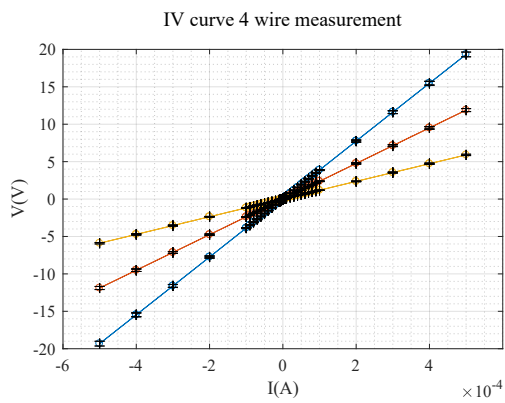


Figure K.7: IV channel 7 carbon glue

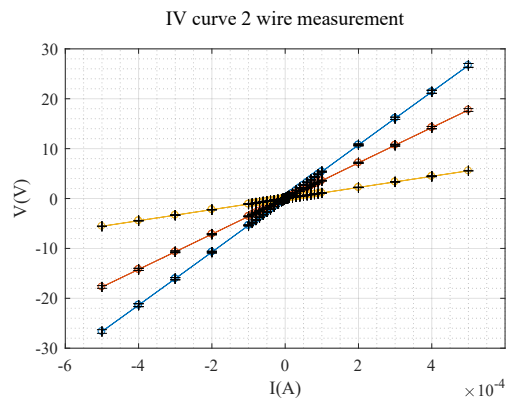
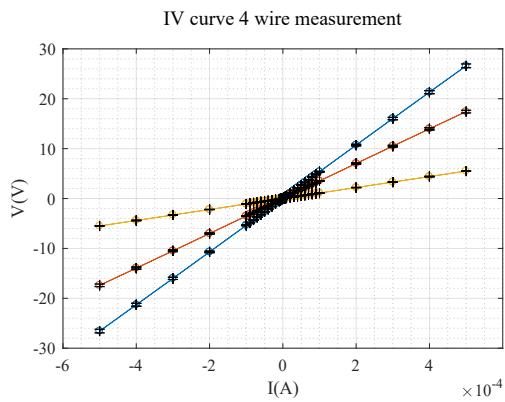


Figure K.8: IV channel 8 carbon glue

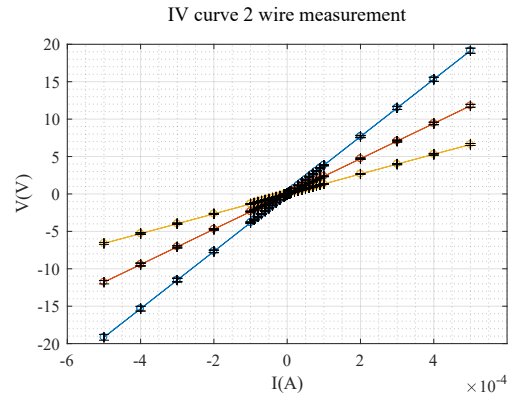
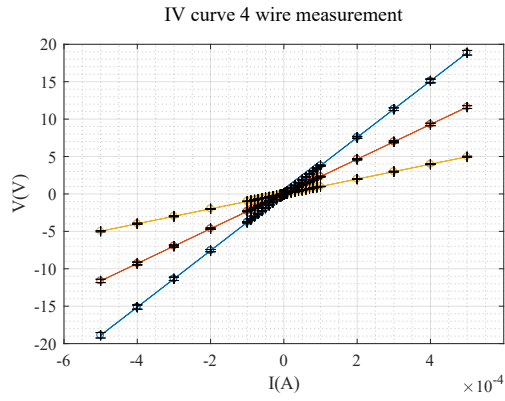


Figure K.9: IV channel 9 carbon glue

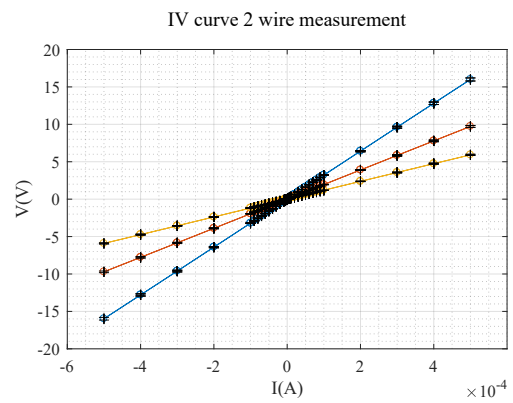
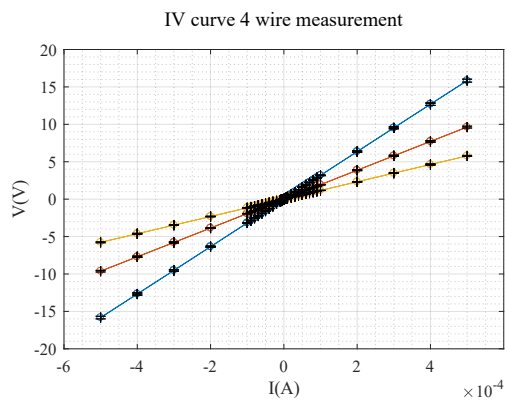


Figure K.10: IV channel 10 carbon glue

Appendix L

Measurements on strain gauges with straight channels containing paint

Table L.1: Resistances 860 μm strain gauge incorporating straight channels with graphite paint

Channel nr.	Resistance (Ω)
1	12508 ± 9
2	10561 ± 10
3	10361 ± 1
4	11230 ± 3
5	11833 ± 4
6	11073 ± 8
7	11203 ± 3
8	9010 ± 3
9	10807 ± 2
10	11269 ± 13

Table L.2: Resistances 1260 μm strain gauge incorporating straight channels with graphite paint

Channel nr.	Resistance (Ω)
1	9987 ± 19
2	11237 ± 8
3	12719 ± 9
4	11139 ± 12
5	10610 ± 6
6	9938 ± 18
7	7721 ± 8
8	10703 ± 6
9	14717 ± 12
10	14432 ± 45

L.1 Datasets for 860 μm beam incorporating channels filled with paint

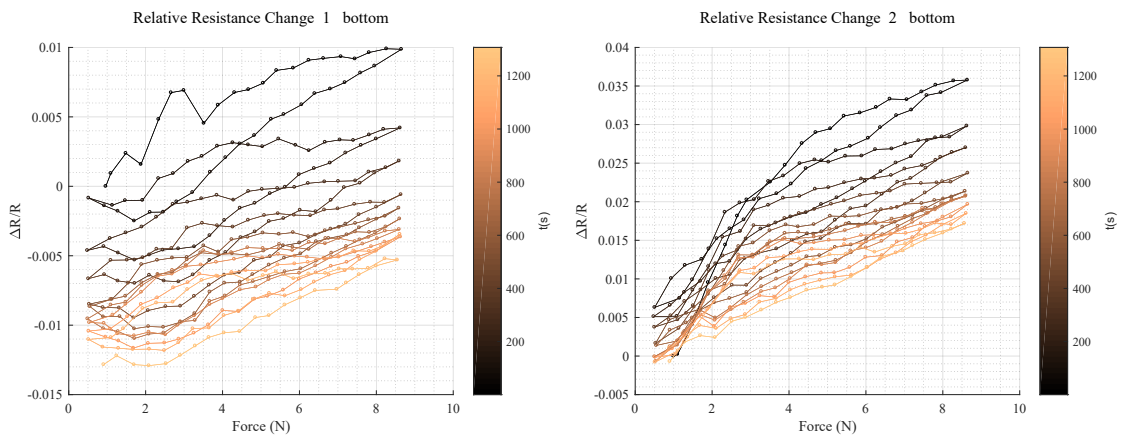


Figure L.1: Resistance change when pushing from bottom

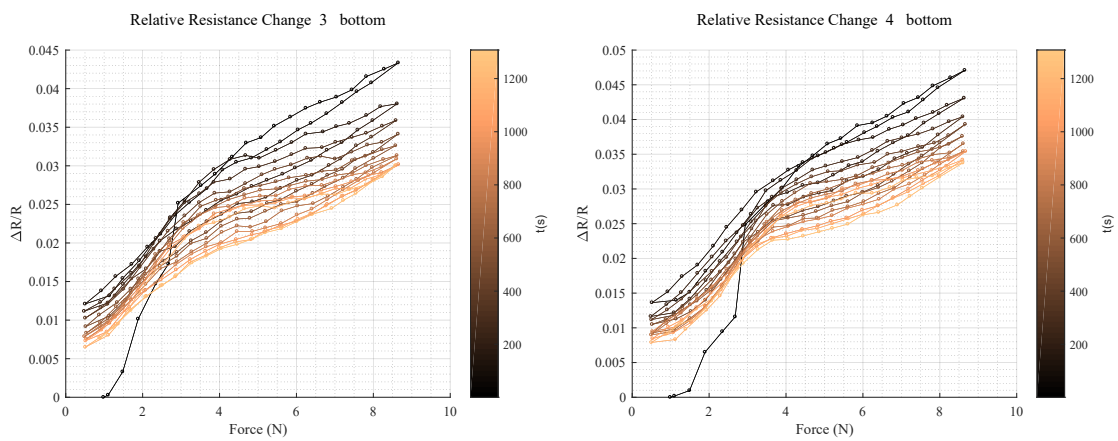


Figure L.2: Resistance change when pushing from bottom

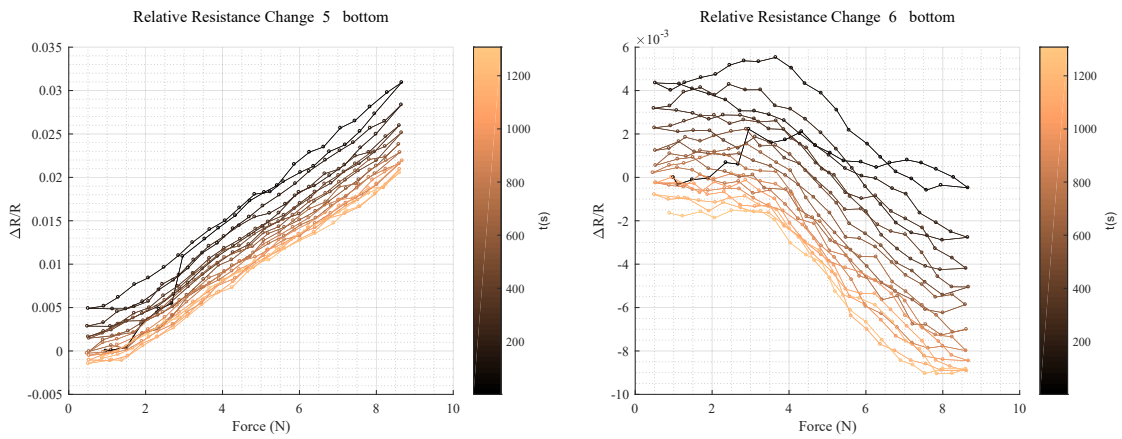


Figure L.3: Resistance change when pushing from bottom

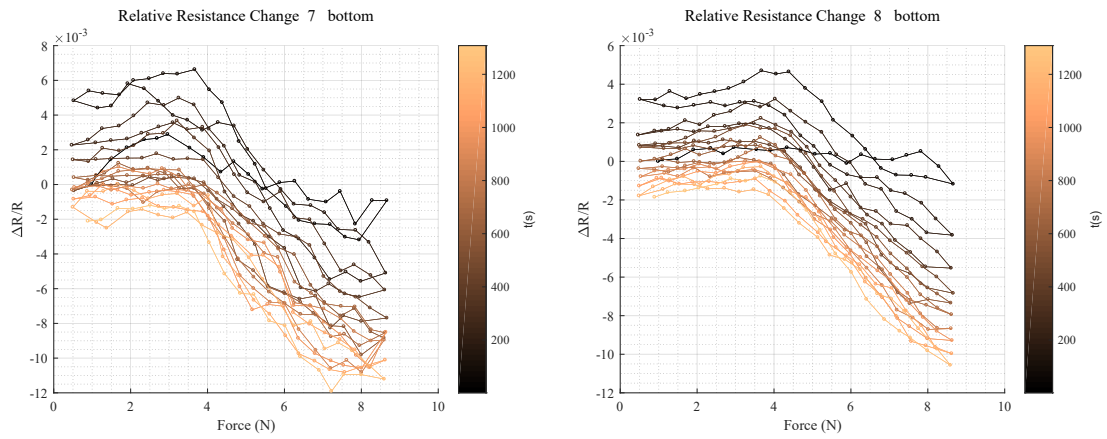


Figure L.4: Resistance change when pushing from bottom

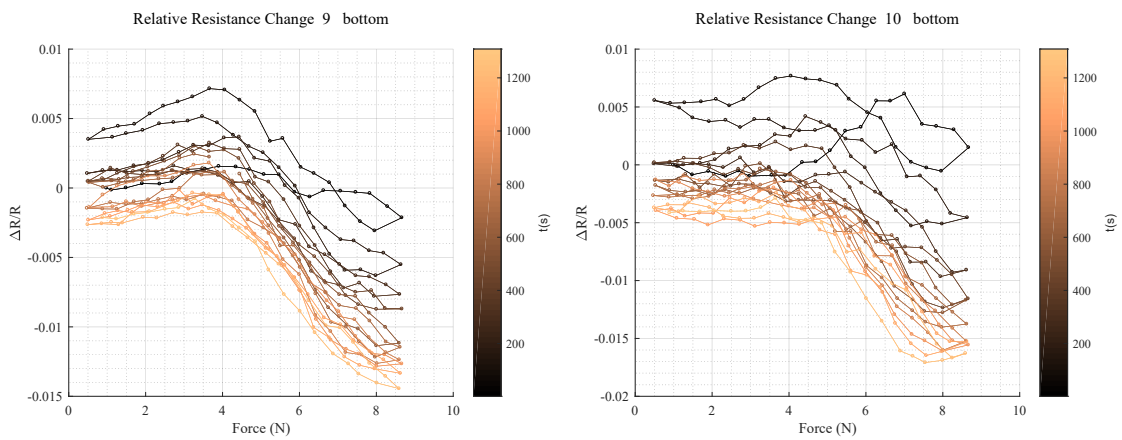


Figure L.5: Resistance change when pushing from bottom

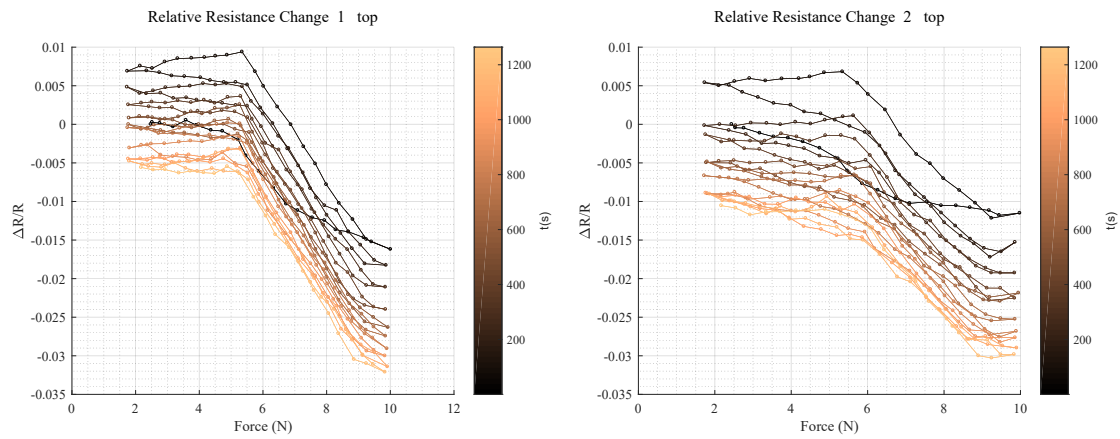


Figure L.6: Resistance change when pushing from top

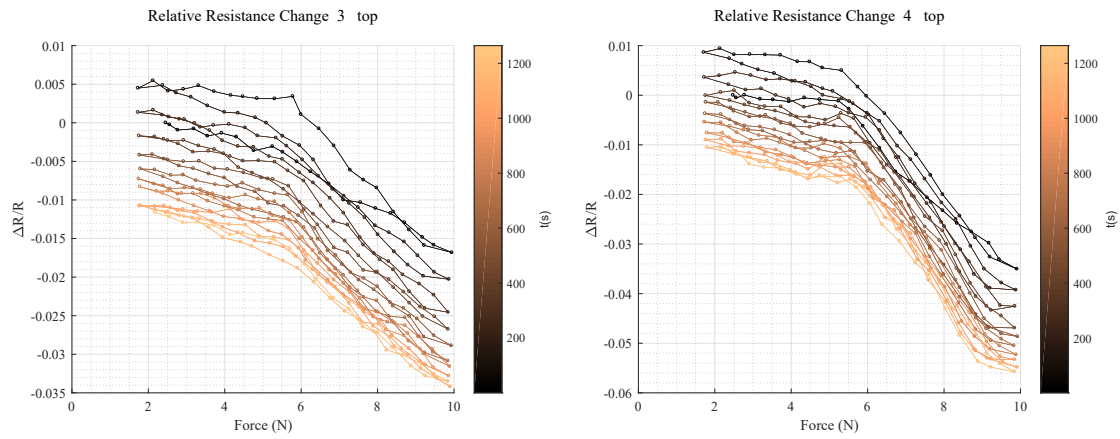


Figure L.7: Resistance change when pushing from top

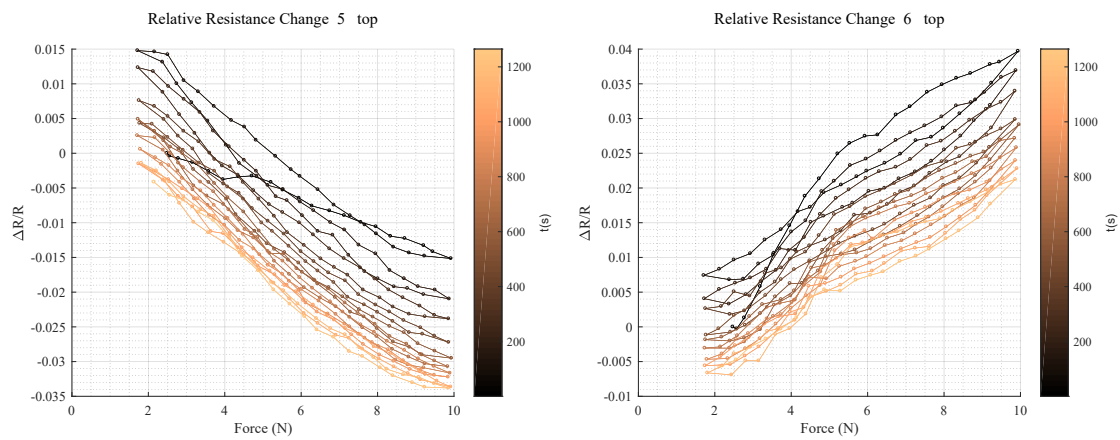


Figure L.8: Resistance change when pushing from top

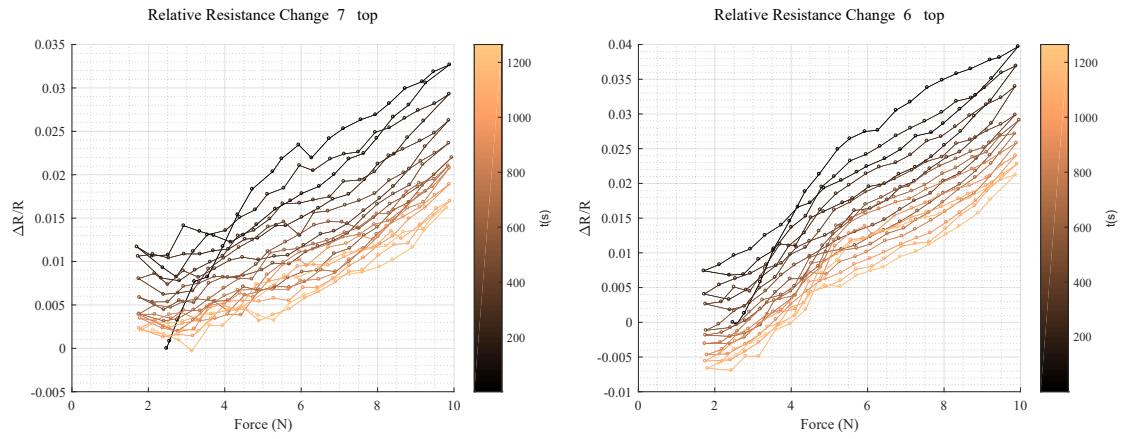


Figure L.9: Resistance change when pushing from top

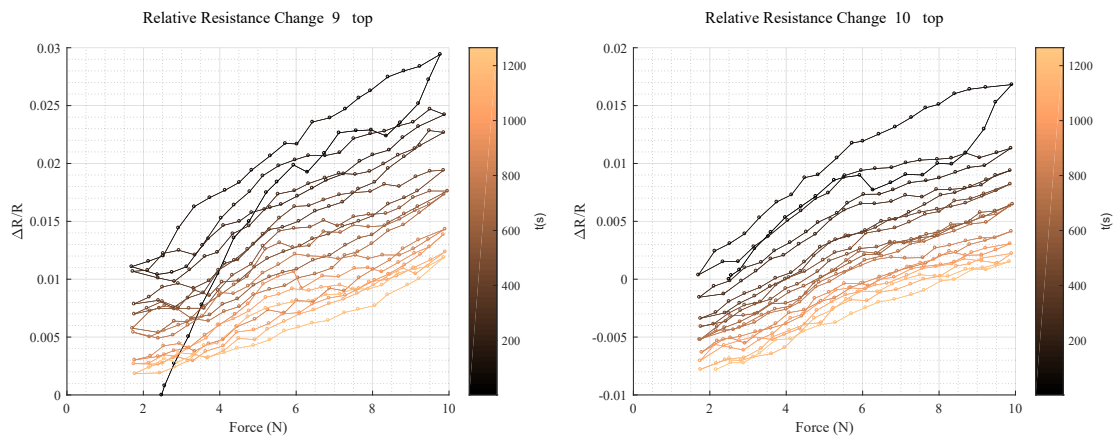


Figure L.10: Resistance change when pushing from top

Appendix M

Measurements on strain gauges with straight channels containing paint

Table M.1: Resistances 860 μm strain gauge incorporating straight channels with carbon glue

Channel nr.	Resistance ($\text{k}\Omega$)
1	36.1 ± 0.1
2	41.1 ± 0.1
3	37.6 ± 0.1
4	49.4 ± 0.1
5	262 ± 0.4
6	118 ± 0.8
7	178 ± 0.9
8	72.8 ± 0.1
9	25.0 ± 0.1
10	123 ± 0.4

Table M.2: Resistances 1260 μm strain gauge incorporating straight channels with carbon glue

Channel nr.	Resistance ($\text{k}\Omega$)
1	73.1 ± 0.268
2	686 ± 2.76
3	31.8 ± 0.1
4	21.4 ± 0.1
5	95.9 ± 0.3
6	36.9 ± 0.2
7	512 ± 2.09
8	82.3 ± 0.4
9	434 ± 2.25
10	130 ± 0.9

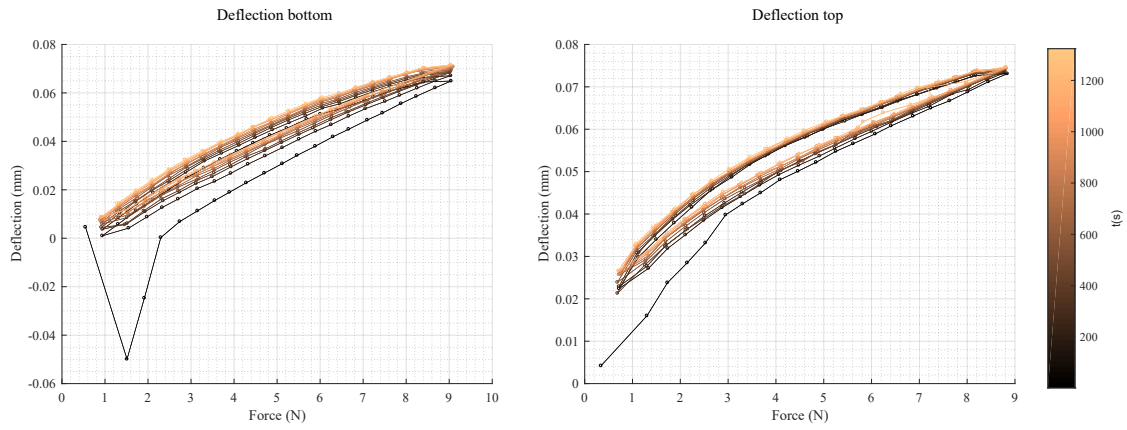


Figure M.1: Deflection 860 μm beam incorporating straight channels filled with carbon glue

M.1 Datasets for 860 μm beam incorporating channels filled with glue

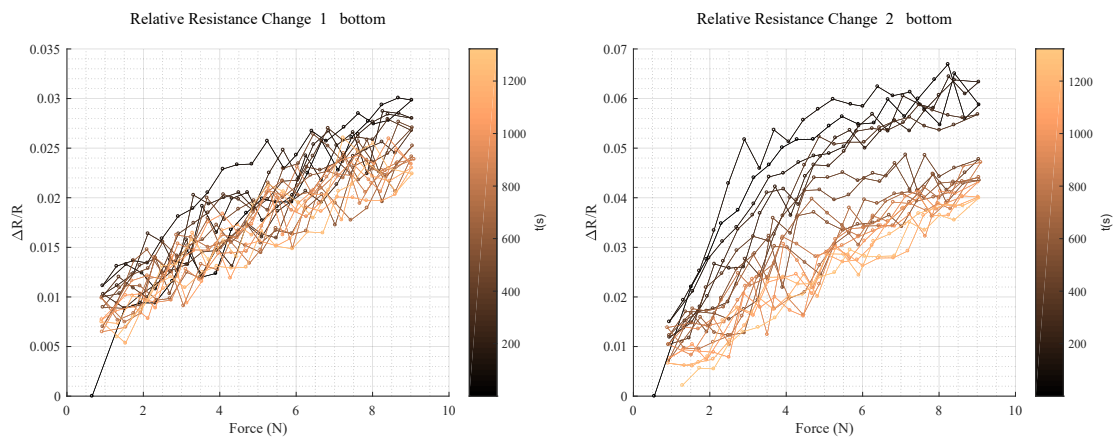


Figure M.2: Resistance change when pushing from bottom

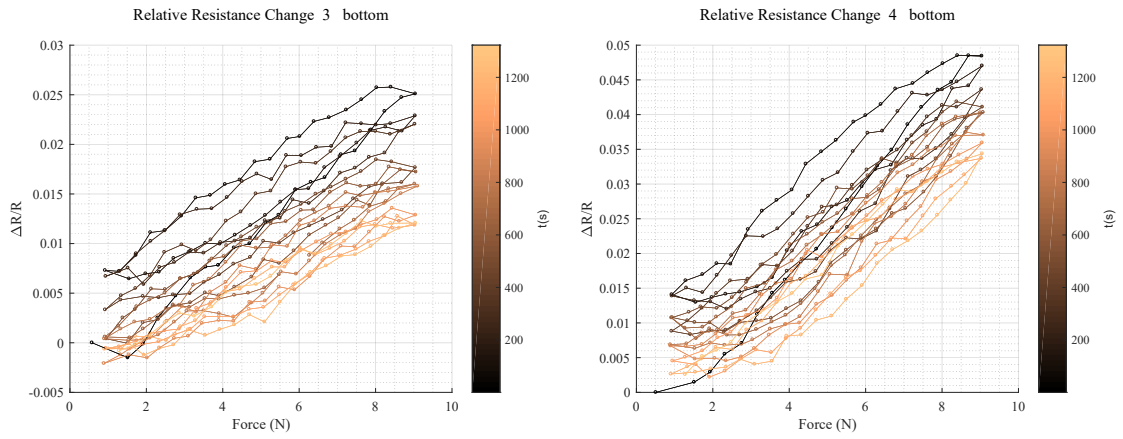


Figure M.3: Resistance change when pushing from bottom

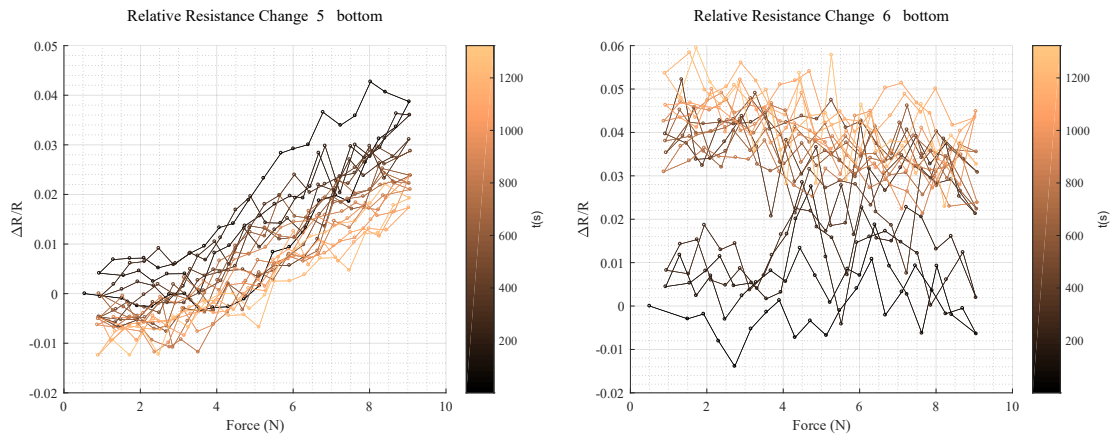


Figure M.4: Resistance change when pushing from bottom

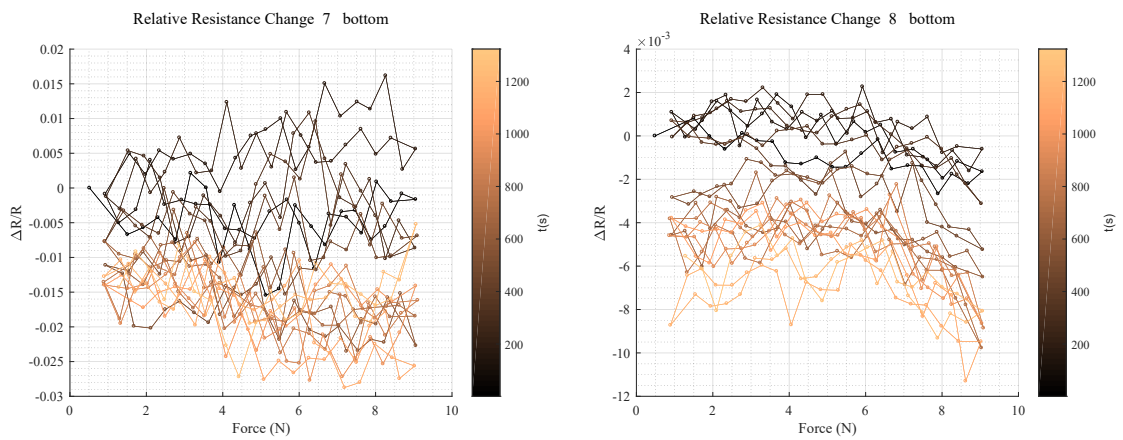


Figure M.5: Resistance change when pushing from bottom

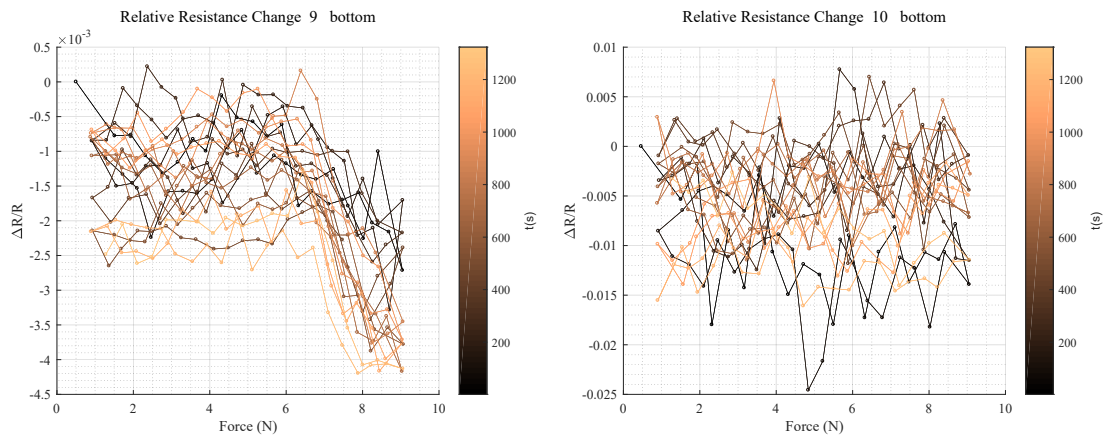


Figure M.6: Resistance change when pushing from bottom

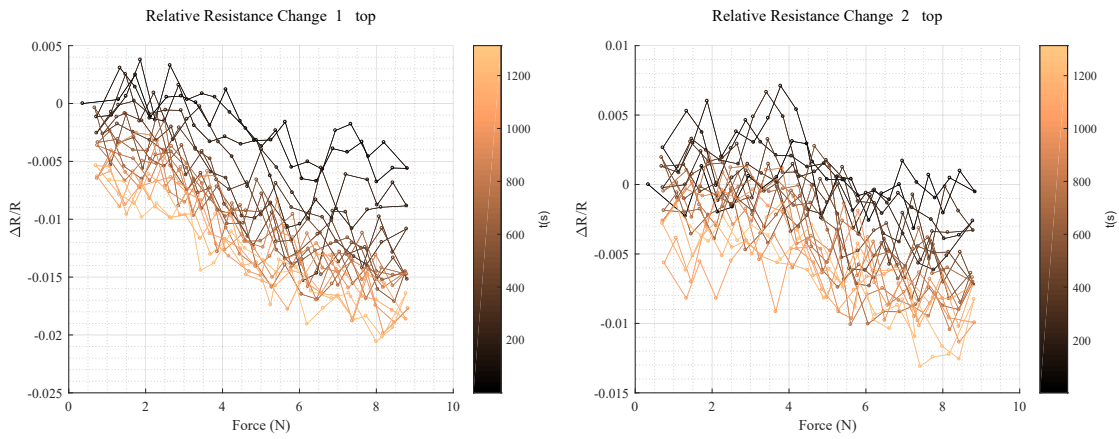


Figure M.7: Resistance change when pushing from top

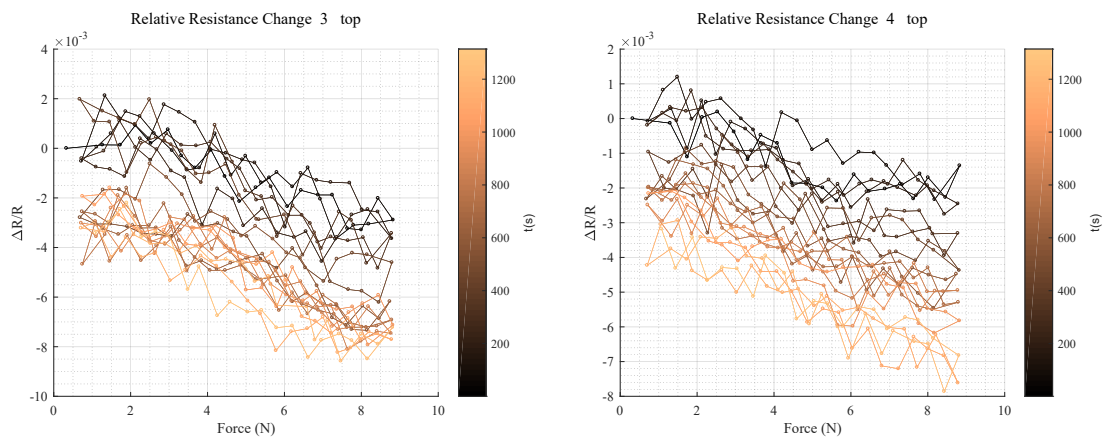


Figure M.8: Resistance change when pushing from top

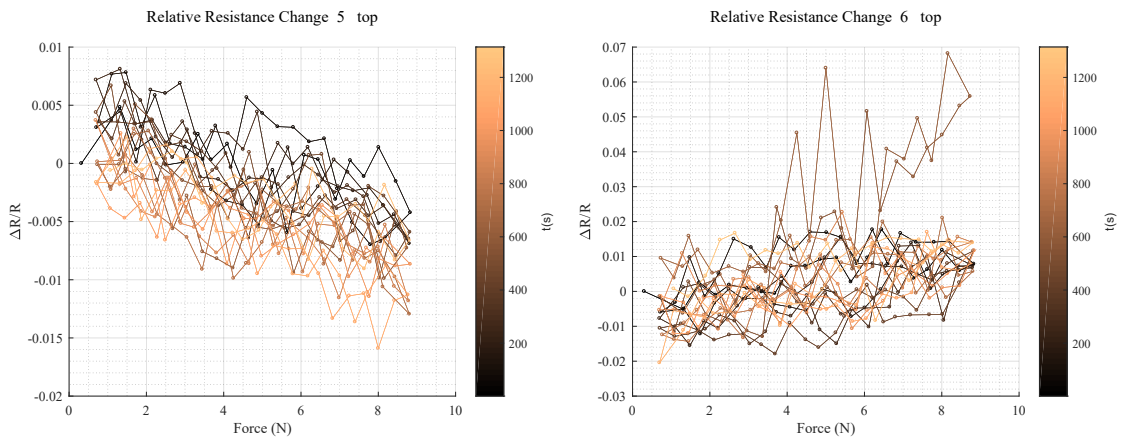


Figure M.9: Resistance change when pushing from top

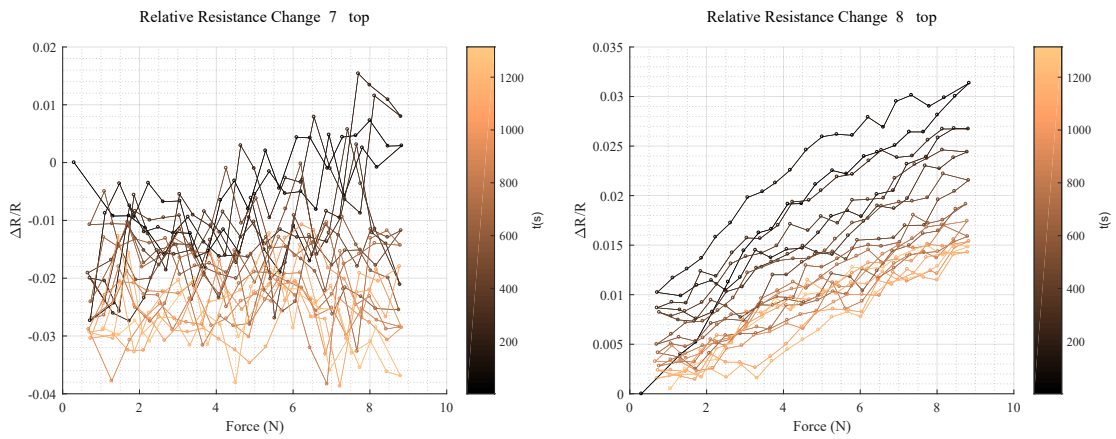


Figure M.10: Resistance change when pushing from top

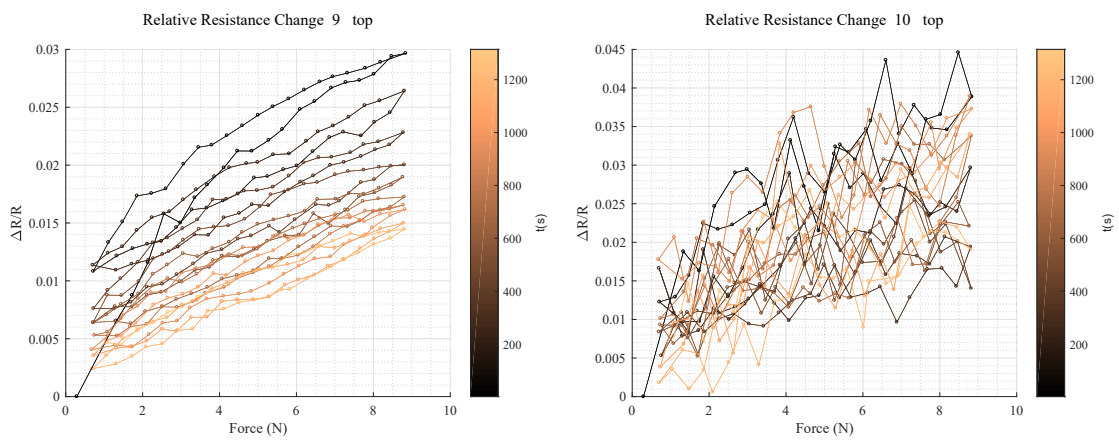


Figure M.11: Resistance change when pushing from top

Appendix N

Measurements on strain gauges with tapered channels containing paint

Table N.1: Resistances 860 μm strain gauge incorporating tapered channels with carbon glue

Channel nr.	Resistance (Ω)
1	78969 ± 107
2	24720 ± 12
3	213537 ± 720
4	33384 ± 17
5	42623 ± 24
6	11969 ± 6
7	15891 ± 10
8	15094 ± 12
9	18958 ± 11
10	16408 ± 7

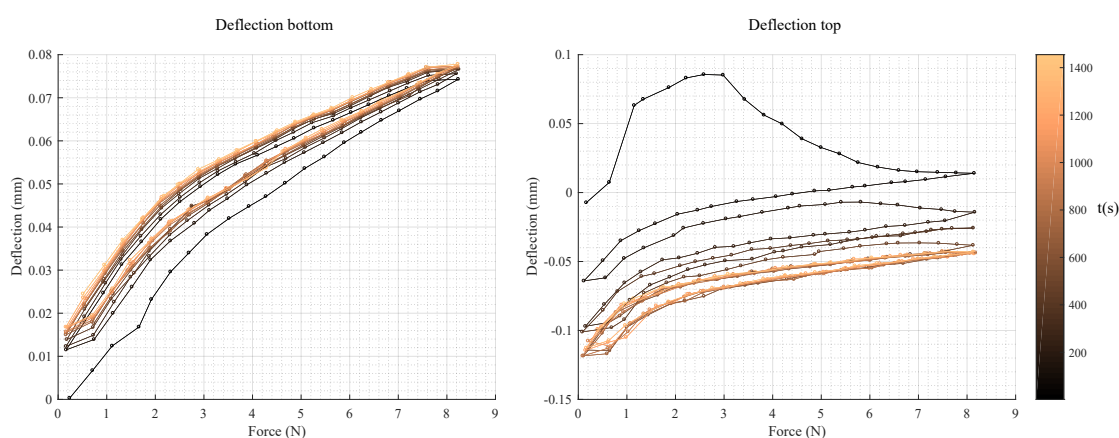


Figure N.1: Deflection beam with tapered channels. On the right the displacement sensor got loose

N.1 Datasets for 860 μm beam incorporating tapered channels filled with paint

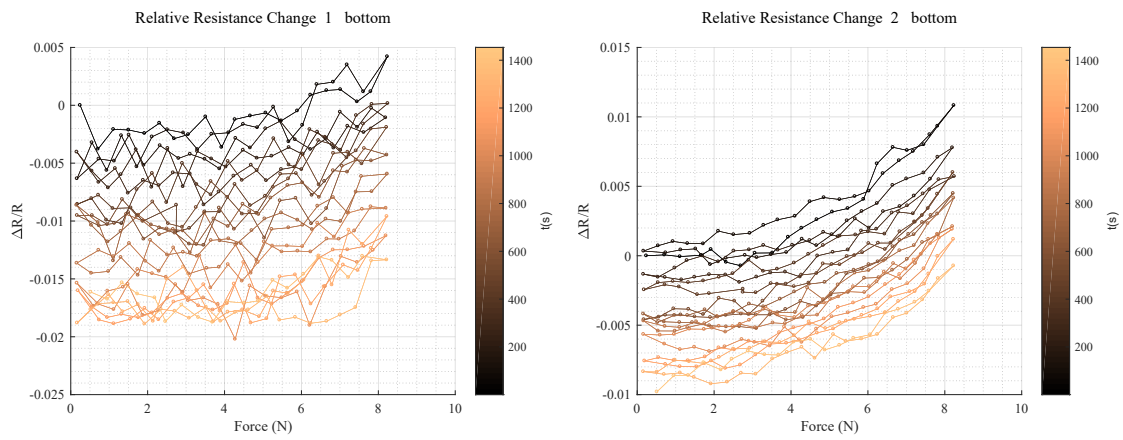


Figure N.2: Resistance change when pushing from bottom

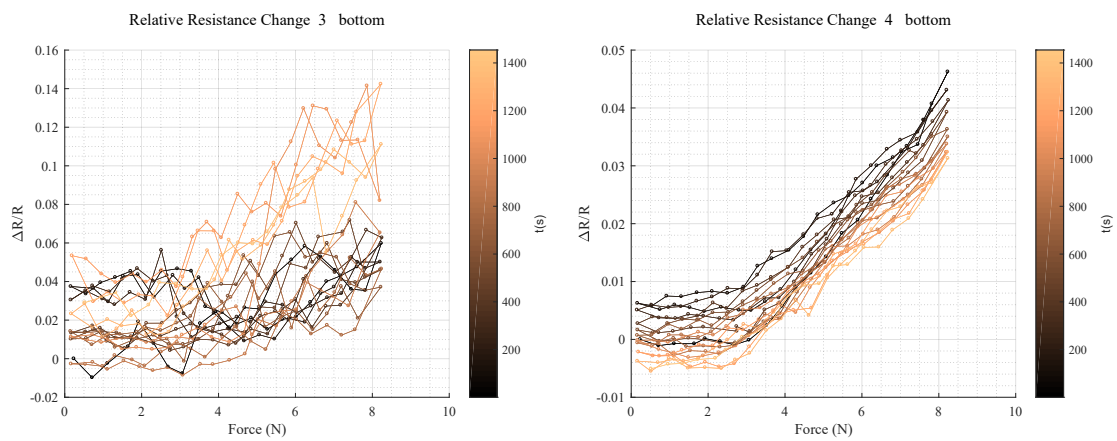


Figure N.3: Resistance change when pushing from bottom

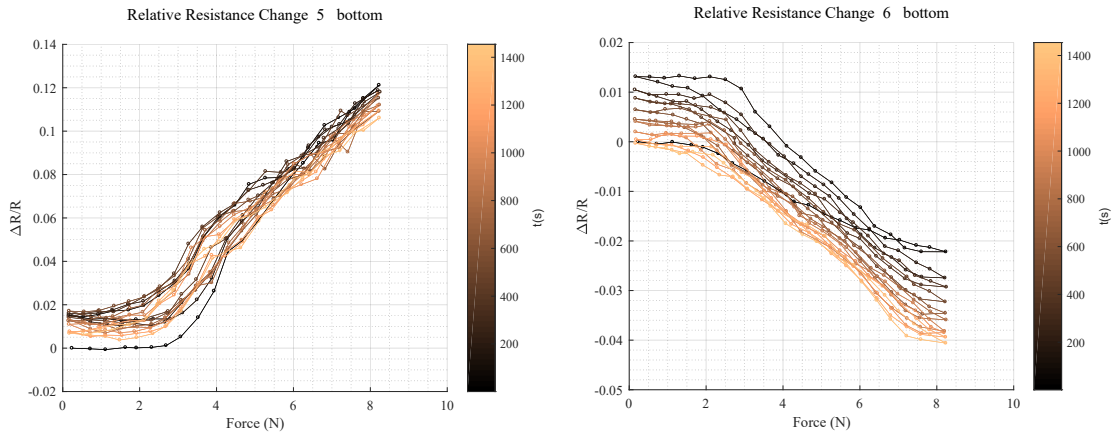


Figure N.4: Resistance change when pushing from bottom

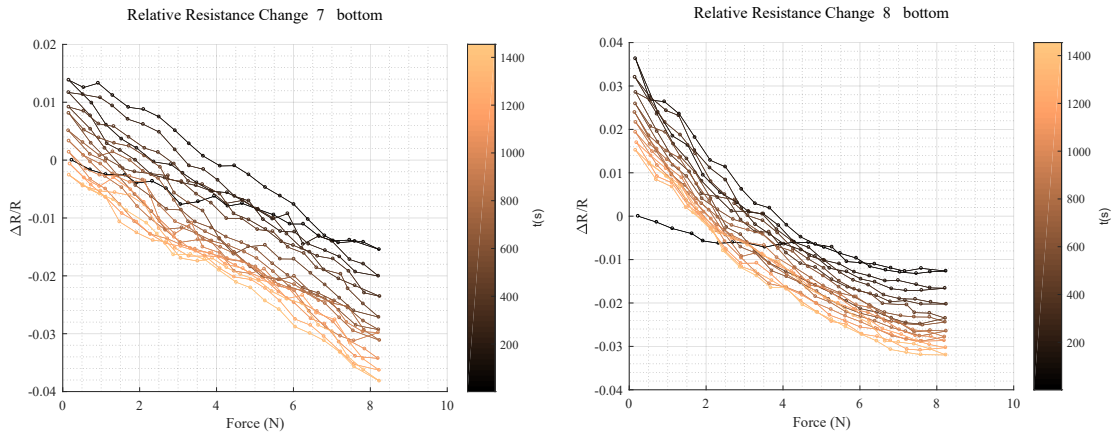


Figure N.5: Resistance change when pushing from bottom

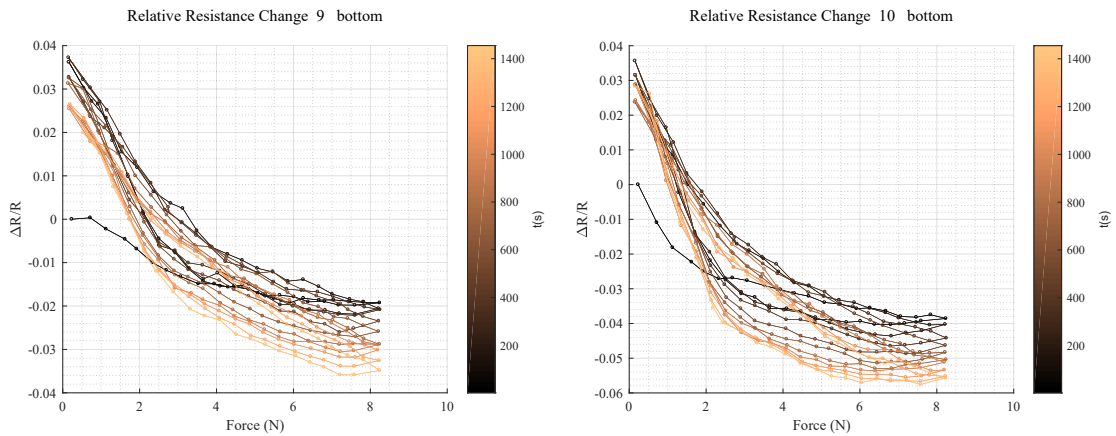


Figure N.6: Resistance change when pushing from bottom

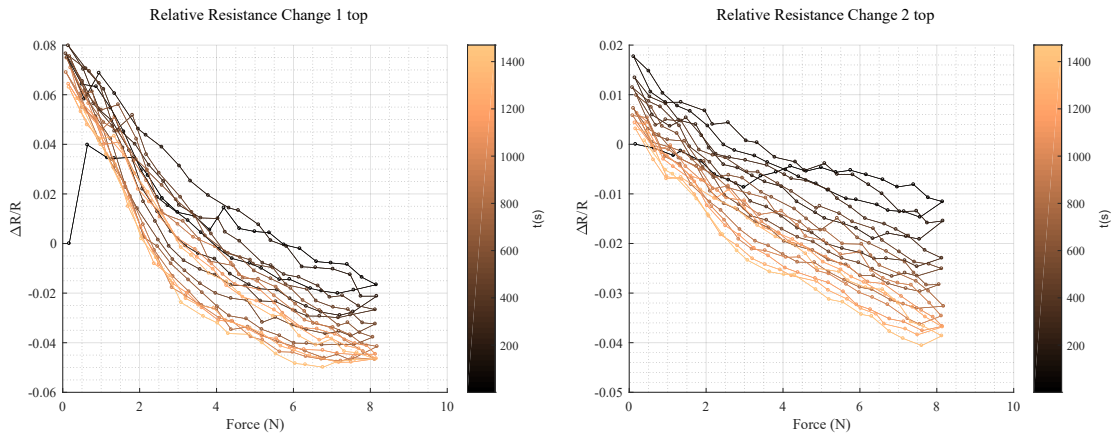


Figure N.7: Resistance change when pushing from top

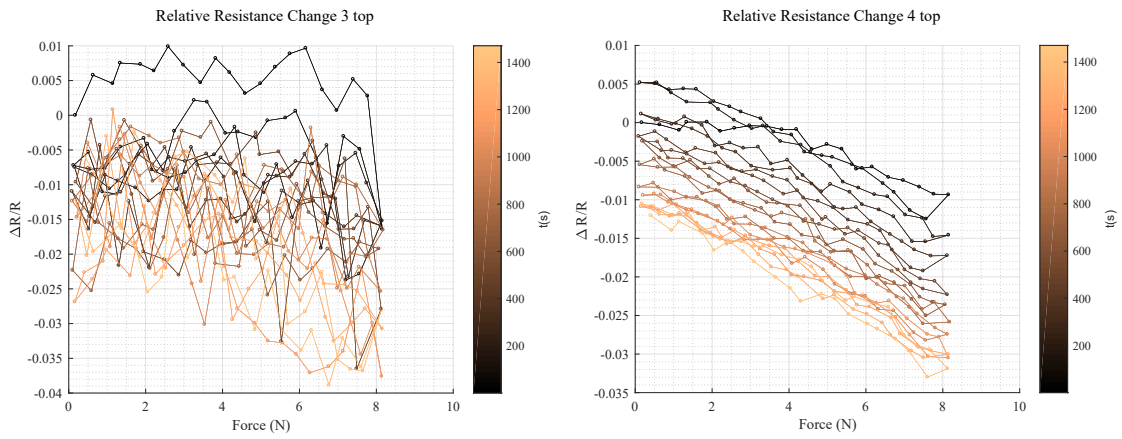


Figure N.8: Resistance change when pushing from top

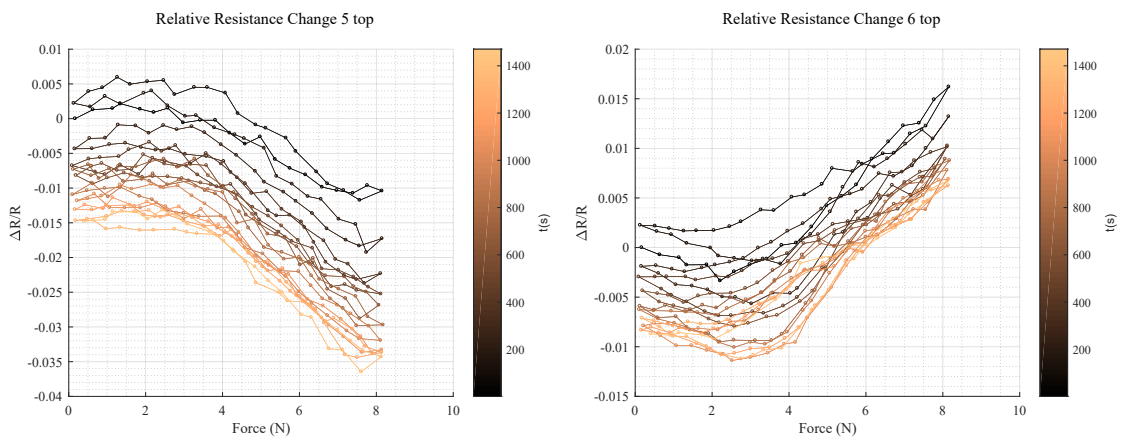


Figure N.9: Resistance change when pushing from top

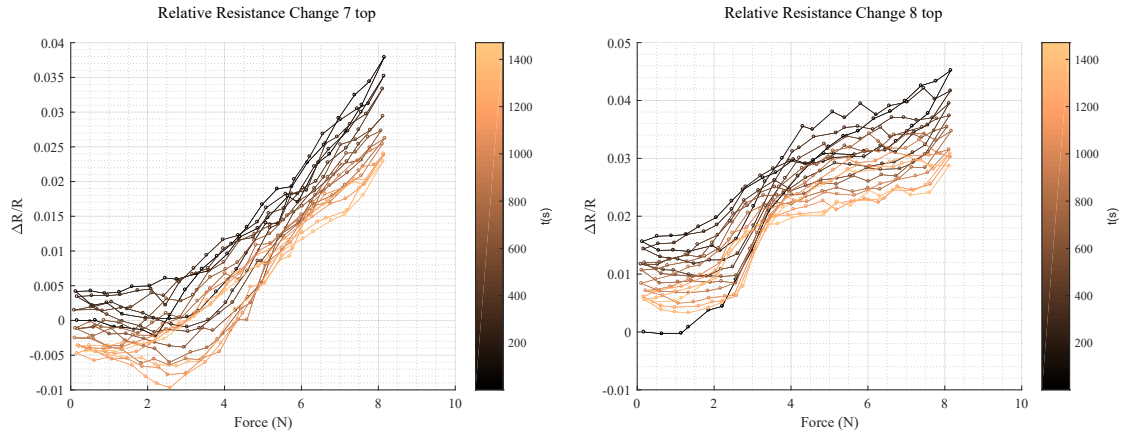


Figure N.10: Resistance change when pushing from top

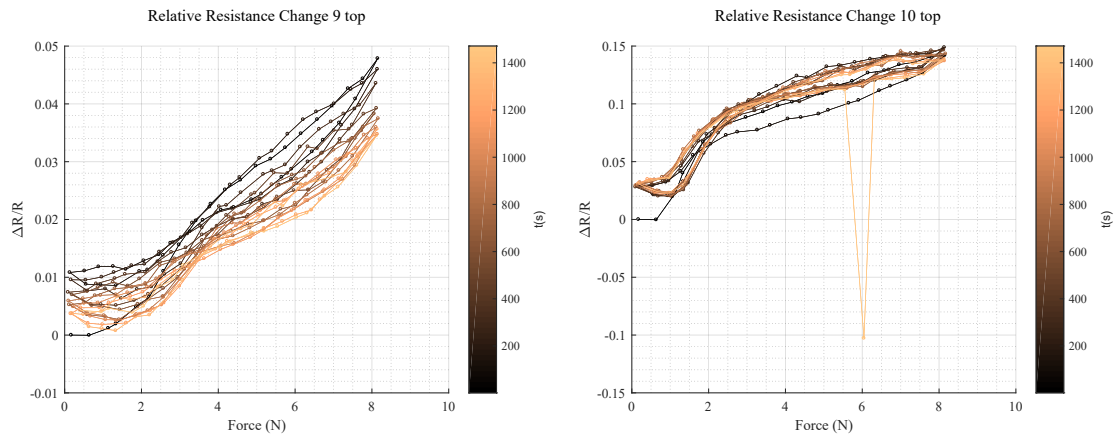


Figure N.11: Resistance change when pushing from top